“Modeling of the bile canalicular network during liver regeneration and fibrosis after carbon tetrachloride intoxication”

INAUGURAL – DISSERTATION

zur Erlangung des Grades eines

Dr. med. vet.

beim Fachbereich der Veterinärmedizin

der Justus-Liebig-Universität Gießen

Seddik Hammad

Aus dem Institut für Pharmakologie und Toxikologie
des Fachbereichs Veterinärmedizin
der Justus-Liebig-Universität Gießen
Betreuer: Prof. Dr. med. vet. Ernst Petzinger
und
dem Leibniz-Institut für Arbeitsforschung an der TU Dortmund (IfADo)
Betreuer: Prof. Dr. med. Jan Hengstler

Modeling of the bile canalicular network during liver regeneration and fibrosis after carbon tetrachloride intoxication

INAUGURAL – DISSERTATION

zur Erlangung des Grades eines

Dr. med. vet.

beim Fachbereich der Veterinärmedizin
der Justus-Liebig-Universität Gießen

eingereicht von

Seddik Hammad

Tierarzt, South Valley Universität
Qena- Ägypten

Gießen 2012

Die Durchführung dieser Arbeit wurde ermöglicht durch die finanzielle Unterstützung durch die South Valley Universität Ägypten - Fakultät für Veterinärmedizin.

Mit Genehmigung des Fachbereiches Veterinärmedizin
der Justus-Liebig-Universität Gießen

Dekan: Prof. Dr. h. c. med. vet. M. Kramer

Gutachter:
Prof. Dr. med. vet. Ernst Petzinger
Prof. Dr. med. Jan Hengstler

Tag der Disputation: 15.06.2012

Table of contents

==========

	Page
Table of contents…….....	1
List of figures and tables …….	6
1. Abstract and aims of the work	9
2. Literature review	
2.1. Hepatic micro-architecture ……...	11
2.1.1. The hepatic vascular system …….....	13
2.1.2. The biliary network ……...	13
2.1.3. Hepatocyte ……. …..	14
2.1.4. Hepatic sinusoid and liver sinusoidal endothelial cell ……..	14
2.1.5. Hepatic stellate cell (HSC) ……	15
2.2. Models of hepatic damage and regeneration responses……	15
2.2.1. Carbon tetrachloride induces centrilobular hepatocyte necrosis ……...	16
2.2.2. Prolonged administration of carbon tetrachloride induces septal fibrosis…….	18
2.3. Hepatocellular polarity during liver regeneration …….....	18
2.3.1. The basolateral surface of the hepatocyte …….	19
2.3.2. The apical surface of the hepatocyte …….	19
2.4. Hepatic micro-architecture organization during intoxication and regeneration...	20
3. Material	
3.1. Animals…….	22
3.2. Chemicals……..	22
3.3. Equipment…….....	24
3.4. Antibodies…….	25
3.4.1. Primary antibodies…….	25
3.4.2. Secondary antibodies…….	26
3.5. Preparation of buffers and reagents……..	28
3.5.1. 10X Phosphate buffered saline (10X PBS)……. …….....	28
3.5.2. 10X Tris-buffered saline (10X TBS) ……	28
3.5.3. Preservation buffer…….	29

3.5.4. Carbon tetrachloride (CCl_4) solution……. 29
3.5.5. Bromodeoxy uridine (BrdU) solution…… 29
3.5.6. Antigen retrieval agent……... 29
3.5.7. DNA denaturation agent…… 30
3.5.8. Blocking serum…….. 30
3.5.9. Dilution buffer……..... 30
3.5.10. DAPI solution…….. 30
3.5.11. Mounting media (mowiol) …….. 30
3.5.12. Mayer's hematoxylin……... 31
3.5.13. Eosin……..... 31
3.5.14. Picro-sirius red solution……... 31
3.6. Software……..... 31

4. Methods

4.1. Animal experiments……..... 32
4.1.1. Administration of carbon tetrachloride and BrdU…….. 32
4.1.2. Hepatocellular polarity during liver regeneration…….. 32
4.1.3. Induction of liver fibrosis……... 33
4.1.4. Excision and fixation of liver lobes……... 33
4.2. Preparation of liver tissue for histology and immunohistochemistry……... 34
4.2.1. Embedding of the liver lobes on paraffin…….. 34
4.2.2. Preparation of vibratome liver slices for immunostaining……. 34
4.3. Principles of immunohistochemistry and immunofluorescence staining……. 34
4.4. Liver histology and immunohistochemistry using paraffin embedded sections... 36
4.4.1. Hematoxylin and eosin (H&E) staining…… 36
4.4.2. Picro-sirius red staining……. 37
4.4.3. Immunohistochemistry of BrdU…… 37
4.4.4. Immunohistochemistry of glutamine synthetase (GS)……... 38
4.4.5. Immunohistochemistry of alpha-smooth muscle actin (α-SMA)…….. 39
4.5. Immunofluorescence staining using vibratome slices…….. 41

4.5.1. Architectural staining……. 41
4.5.2. Proliferation staining…….. 41
4.5.3. Co-staining of BrdU and different membrane markers……. 42
4.5.4. Co-staining of alpha-tubulin and different membrane markers……. 43
4.5.5. Co-staining of DPPIV/CD26 and Mrp2 or Claudin1……. 44
4.5.6. Co-staining of DPPIV/CD26, ICAM1 and dylight 649 conjugated donkey anti-mouse (DMs)……. …….. 44
4.5.7. Co-staining of DPPIV/CD26 and collagen III…… 45
4.6. Image analysis and microscopy…… 46
4.6.1. Fluorescence and bright field microscopy……. 46
4.6.2. Confocal laser scanning microscopy and Z-stack preparation……... 46
4.7. Quantification of the centrilobular necrosis…….. 47
4.8. Quantification of BrdU-positive hepatocytes……... 47
4.9. Quantification of α-SMA positive area……. 48
4.10. Mathematical modeling…….. 48
4.11. Statistical analysis……..... 49
5. Results
5.1. Establishment of immunostaining protocols……. 50
5.1.1. DPPIV/CD26 antibody labels the bile canaliculi and the hepatic sinusoids…. 50
5.1.2. The bile canalicular signal of DPPIV/CD26 antibody co-localizes with Mrp2 and claudin1 signals……..... 51
5.1.3. Glutamine synthetase is a specific marker for the centrilobular hepatocytes… 53
5.1.4. Dylight 649-conjugated donkey anti-mouse (DMs) localizes at the hepatic sinusoids……..... 54
5.2. Characterization of liver intoxication and regeneration after carbon tetrachloride injection……..... 56
5.2.1. Mouse weight and liver weight (%)……... 56
5.2.2. Analysis of the centrilobular necrosis…… 57
5.2.2.1. Macroscopical analysis……... 57

5.2.2.2. Microscopical analysis…… 59
5.2.2.3. Confirmation of the centrilobular carbon tetrachloride-induced necrosis by fluorescence microscopy……..... 61
5.2.3. Hepatocyte proliferation…… 62
5.2.3.1. Quantification of BrdU incorporation……. 62
5.2.4. Total hepatocyte nuclei number per square millimeter…….. 65
5.2.5. Simulation of the destruction and regeneration processes after carbon tetrachloride by a mathematical model…… 67
5.2.6. Characterization of liver fibrosis induced by repetitive carbon tetrachloride injections……..... 68
5.3. Hepatocyte polarity during carbon tetrachloride-induced hepatotoxicity and regeneration……..... 71
5.3.1. The apical domains of hepatocytes are maintained during both S- and M-phases……..... 71
5.3.2. Hepatocytes maintain basolateral domains during both S- and M-phases…… 73
5.3.3. Hepatocytes preserve claudin-1 (tight junction protein) during both S- and M-phases……..... 75
5.3.4. Bile canaliculi are preserved during different phases of mitosis……... 76
5.3.5. Establishment of bile canaliculi between the daughter hepatocytes…….. 78
5.4. Reconstruction of the bile canalicular network of the normal, intoxicated, regenerated and fibrotic livers……. 80
5.4.1. Reconstruction of the bile canalicular network of the normal livers……. 80
5.4.1.1. The bile canaliculi form three half-hexagonal belts around the hepatocytes.. 81
5.4.1.2. Two classes of bile canaliculi……. 82
5.4.1.3. Three hepatocytes surrounding one sinusoid form a frequently observed basic building block……. 84
5.4.1.4. Hepatic sinusoids surrounded by a hexagonal belt of bile canaliculi……. 85
5.4.1.5. Unconnected branches of the bile canalicular network ´dead ends`……... 86
5.4.2. Bile canalicular network integrity during intoxication and fibrosis…….. 89

==========

6. Discussion……..……... 90

7. Summary…….…….... 101

8. References…….…….. 105

9. Erklärung…….……... 121

Acknowledgements

List of publications

List of figures

Page

Figure 2.1. The murine liver is a multi-lobular and multi-cellular organ…….. 12

Figure 2.2. Postulated mechanism of the toxicological action of carbon tetrachloride …… 17

Figure 2.3. Organization of the bile canalicular network……. 21

Figure 4.1. Experimental design of the spatial-temporal modeling of liver intoxication and regeneration…… 32

Figure 4.2. Establishment of a novel bile canaliculus between the daughter cells……... 33

Figure 4.3. Immunohistochemistry protocol of formalin fixed paraffin embedded sections….. 35

Figure 4.4. Immunofluorsence staining protocol of vibratome prepared slices…… 36

Figure 4.5. Hematoxylin & eosin staining and BrdU immunohistochemistry of the paraffin embedded mouse livers ……..……. 48

Figure 5.1. DPPIV/CD26 immunoreactivity at the bile canaliculi and the hepatic sinusoid…… 51

Figure 5.2. The bile canalicular signal of the DPPIV/CD26 antibody co-labeling with Mrp2 and claudin1……... 52

Figure 5.3. Glutamine synthetase signal reported at the centrilobular hepatocytes…….. 53

Figure 5.4. The dylight 649-conjugated donkey anti-mouse (DMs) signal visualized at the hepatic sinusoids…… 55

Figure 5.5. Mouse weight (g) and liver weight as a percentage of body weight at different time points after carbon tetrachloride injection……. 56

Figure 5.6. Macroscopical appearance of mouse livers at different time points after administration of 1.6 g/kg carbon tetrachloride……. 58

Figure 5.7. Microscopical appearance by hematoxylin and eosin (H&E) staining of mouse livers after intoxication. ……..……... 59

Figure 5.8. Quantification of the centrilobular necrosis in hematoxylin and eosin (H&E) stained liver sections. ……..……... 61

Figure 5.9. Microscopical appearance of control mouse liver and two days after carbon tetrachloride intoxication using confocal laser scanning microscopy of immunostained slices.... 62

Figure 5.10. Proliferation status of hepatocytes was investigated by BrdU immunostaining of control and carbon tetrachloride-intoxicated mouse livers ……... 63

Figure 5.11. Quantification of the BrdU-positive hepatocyte in control and intoxicated mouse livers……... 65

Figure 5.12. The total number of hepatocyte nuclei per mm^2 was investigated by BrdU immunostaining of mouse livers at different time points after intoxication…….. 66

Figure 5.13. Mathematical modeling of liver intoxication and regeneration. ……..... 67

Figure 5.14. Histopathological examination of mouse livers was investigated by H&E, picro-sirius red alpha-smooth muscle actin (α-SMA) staining……... 69

Figure 5.15. The liver micro-architecture and collagen deposition were analyzed using immunofluorescence staining of deep liver slices……. 70

Figure 5.16. Immunofluorescence microscopy of DPPIV/CD26 on mouse liver slices during S-phase and metaphase. …… 72

Figure 5.17. Immunoreactivity of both Mrp2 and radixin on the bile canaliculi during cell cycle…… 74

Figure 5.18. Immunolocalization of E-cadherin and LDLR at the basolateral surface of the hepatocytes during cell proliferation…….. 75

Figure 5.19. Immunopositivity of a tight junction protein (claudin1) during cell division……... 76

Figure 5.20. Hepatocyte maintained the bile canaliculi during different phases of mitosis…….. 77

Figure 5.21. Establishment of bile canaliculi between daughter hepatocytes……... 79

Figure 5.22. A confocal Z-stack of deep liver slices after Imaris processing (normal mouse liver)……..... 81

Figure 5.23. The bile canaliculi form three half-hexagonal belts around the hepatocytes. 82

Figure 5.24. The bile canalicular network forms two classes based on their alignment to the closest sinusoid. ……. 83

Figure 5.25. Observation of a basic building block consisting of one sinusoid and three hepatocytes…….. 84

Figure 5.26. The hepatic sinusoid is surrounded by complete or incomplete belt of bile canaliculi. ……..…….. 86

Figure 5.27. Unconnected branches of the bile canalicular network. ……... 87

Figure 5.28. Disruption of the bile canalicular network after intoxication and fibrosis…… 88

Figure 6.1. Establishment of hepatocellular polarity……. 93

Figure 6.2. Establishment of a novel apical domain and bile canaliculus between the daughter hepatocytes. ……..……... 95

Figure 6.3. Some basic structures of the bile canalicular network. …….. 97

Figure 6.4. Bile canaliculi are located mainly at the center of lateral surface……... 99

List of tables

Page

Table 3.1. Panel of primary antibodies used in the study ……..... 25

Table 3.1. Panel of primary antibodies used in the study (continued)…….. 26

Table 3.2. Panel of secondary antibodies used in the study ……... 26

Table 3.2. Panel of secondary antibodies used in the study (continued)……. 27

Table 5.1. Quantification of the necrotic area after carbon tetrachloride intoxication……..... 60

Table 5.2. Number of BrdU-positive hepatocyte nuclei after intoxication with carbon tetrachloride…..……. 64

1. Abstract and aims of the work

In veterinary medicine, liver disease is a common problem, due to the frequent exposure of both livestock and pets to hepatotoxicants (Villar et al., 1998). Common examples include the exposure of ruminants and pets to the well-known hepatotoxicants, aflatoxins and paracetamol. The liver is a main site for xenobiotic biotransformation and the main target organ for many substances entering the body. Hepatic micro-architecture is tightly linked to the liver function. Therefore, investigation of liver micro-architecture is important to understand the toxico-pathological alterations initiated by different hepatotoxicants. The hepatic lobule consists of hepatocytes, the sinusoidal and bile canalicular networks. The smallest functional basic unit of the liver is made up of hepatocytes and non-parenchymal cells including the hepatic endothelial sinusoidal cells, Kupffer (macrophages) and the stellate cells. Establishment of hepatocellular polarity depends predominantly on this small unit. Communication between hepatocyte-hepatocyte and hepatocyte-non parenchymal cells is required for hepatocellular polarity. This communication is a precondition for both structural and functional properties of hepatocytes and for organ functions. Loss of cell polarity is directly linked to impaired hepatocyte function e.g. detoxification and metabolism. The liver has a remarkable regenerative capacity. Unlike other organs e.g. heart and skeletal muscle, liver regeneration is carried out by proliferation of the surviving hepatocytes without involvement of the stem cell compartment (Fausto and Riehle, 2005). If the proliferation capacity of the mature hepatocyte is compromised e.g. β-catenin depletion, the liver progenitor cells are able to proliferate and maintain the liver functions (Wang et al., 2011). The coordination of different liver cells to establish the functional unit and restore the micro-architecture during toxicity and regeneration is not completely understood. However, advancements in both imaging tools and bioinformatics in the last decade have improved our possibilities

to study morphological alterations during liver regeneration. Such improvements include confocal laser Z-scans, image processing and three-dimensional tissue reconstruction (Hoehme et al., 2010). The initial project that began to use mathematical modeling for tissue reconstruction has discovered some previously unknown but crucial mechanisms during liver toxicity and eventual hepatocyte regeneration. To injure the liver, I used a chemical-driven liver toxicant, carbon tetrachloride, a prototypical inducer of centrilobular hepatocyte necrosis. Carbon tetrachloride-induced damage is similar to a paracetamol overdose. Both toxicants produce a strong necroinflammatory response followed by a well reproducible and highly synchronized regeneration process. In addition, the hepatocyte polarization status during proliferation is elucidated.

The aims of the present study are to

i) Establish a mouse model of both acute and chronic liver intoxication by carbon tetrachloride administration.

ii) Determine the maintenance and establishment of hepatocellular polarity during intoxication and regeneration processes.

iii) Reconstruct the bile canalicular network of the normal, intoxicated, regenerated and fibrotic mouse livers.

2. Literature review

2.1. Hepatic micro-architecture

The liver is a complex organ that has pivotal roles in metabolism, synthesis and storage of carbohydrates, lipids, vitamins and proteins as well as blood filtration from bacteria, bacterial endotoxins, antigen-antibody complexes and other toxic substances by specific detoxification mechanisms then excreted (Boyer et al., 2006). These different functions and liver micro-architecture are tightly linked (Michalopoulos and De Frances, 1997; Michalopoulos and Khan 2005; Michalopoulos 2007; Hoehme et al., 2007). The liver lies in the right upper quadrant of the abdominal cavity and is attached to the diaphragm (Boyer et al., 2006). This unique anatomy enables the liver to serve its dual roles as metabolic and biochemical transformation organ (Sahu, 2007). Therefore, the liver receives blood containing substances absorbed or secreted by the viscera including the spleen, gastrointestinal tract and pancreas and uses these substances as raw materials and modifies them or synthesizes new chemicals. These substances are then returned to the blood stream or to the bile for elimination (Bacon et al., 2006). The mouse liver is a multi-lobular organ (Fig. 2.1A) and consists of four main lobes: caudate lobe, right lobe, median lobe and left lobe (Martins et al., 2008). The hepatic lobule (Fig. 2.1B and C) is the structural and classical unit of the liver. It resembles a polygon with portal triads at the corners and consists of radially arranged plates of 15-25 hepatocytes between the limiting lamellae and the central vein (Rappaport, 1973). There are regularly distributed portal triads at the angles of hepatic lobule. This triad contains microscopic branches of bile duct, hepatic artery and portal vein. From a metabolic point of view, the functional unit is the hepatic acinus. The axis of hepatic acinus is a portal tract and its boundary is described by an imaginary line connecting the neighboring terminal hepatic venules (central veins). Every hepatic acinus is subdivided into three zones of hepatocytes. Each zone has different levels of oxygen supply and metabolic function (Bacon et al., 2006). Zone I (periportal cells) are supplied with blood rich in oxygen, hormones and

substrates. Zone II (mid-zonal cells) and zone III (perivenous cells) are supplied by blood poor in oxygen but rich in carbon dioxide and metabolic products (Gebhardt, 1992; Katz, 1992). Beside liver parenchymal cells (hepatocytes), the organ consists of (Fig. 2.1D) liver endothelial sinusoidal cells (LESC), hepatic stellate cells (HSCs), cholangiocytes (biliary epithelial cells) and Kupffer cells (Boyer et al., 2006; Boehm et al., 2010).

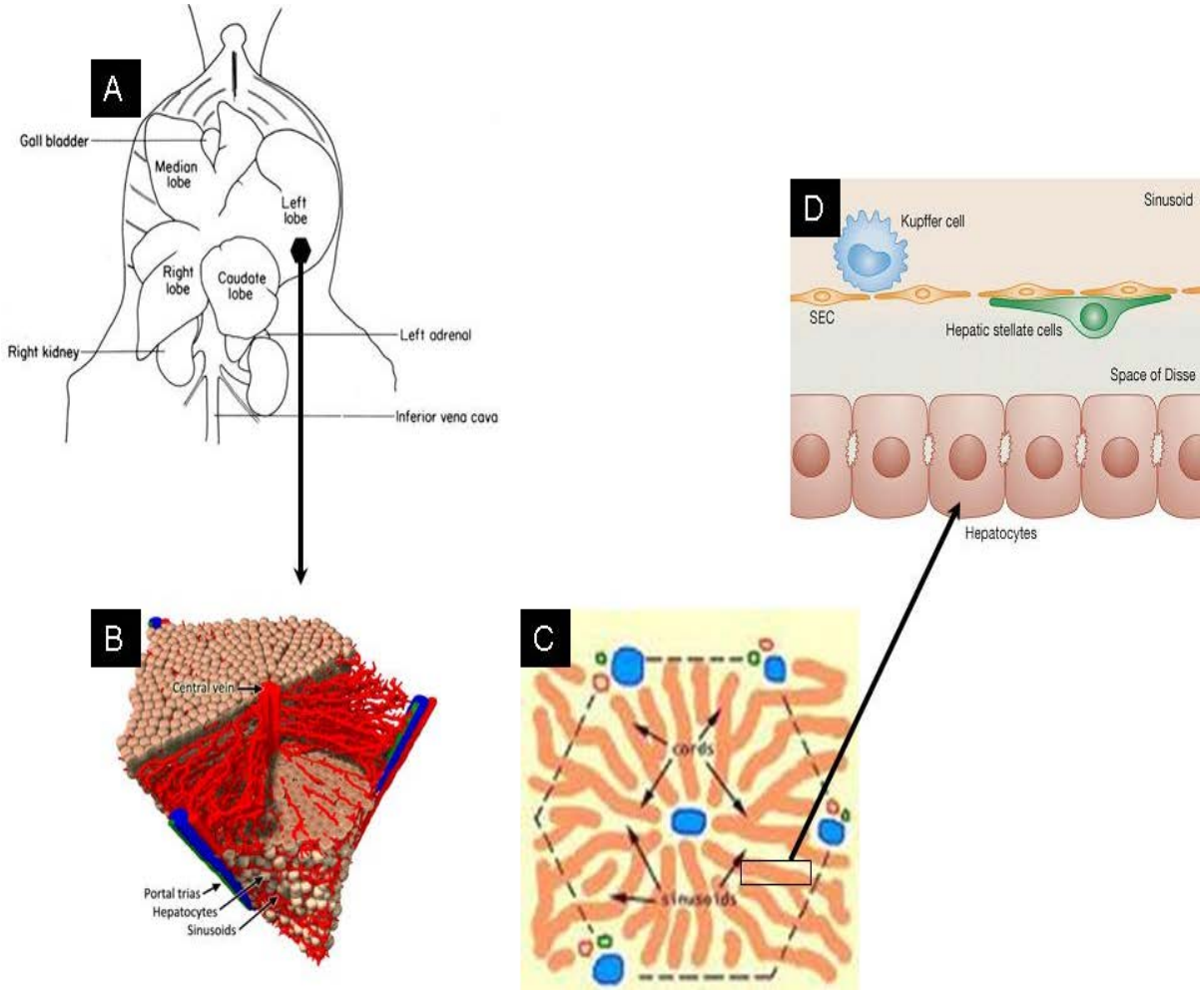

Figure 2.1: The murine liver is a multi-lobular organ. A) Mouse liver has several lobes (source: The anatomy of the laboratory mouse Margaret J. Cook). B) The hepatic lobule is the classical unit of the liver (Hoehme et al., 2010). C) The liver cells are radially arranged in cords between the limiting lamellae and the central vein (www.siumed.edu/~dking2/erg/liver.htm). D) As a multi-cellular organ, liver is composed of hepatocyte (parenchymal cell) and non-parenchymal cells, such as Kuppfer cells, sinusoidal endothelial cells, stellate cells and other cell types (Boehm et al., 2010).

2.1.1. The hepatic vascular system

The hepatic vasculature is specialized to guarantee the corresponding hepatic functions. Nearly 75% of the blood entering the liver is venous blood from the portal vein. All venous blood returning from the small intestine, stomach, pancreas and spleen pour into the portal vein (Bacon et al., 2006). Therefore, the liver comes in contact with nearly all absorbed nutrients from the gastrointestinal tract. The hepatic artery provides the liver with highly oxygenated blood and this represents approximately 25% of the liver blood supply. Terminal branches of both portal vein and hepatic artery mix as they enter the hepatic sinusoids in the liver (McCuskey, 2008). Blood flows through the sinusoids and pours into the central vein of each hepatic lobule. Central veins coalesce into hepatic veins which leave the liver on the dorsal surface and join the inferior vena cava (Boyer et al., 2006).

2.1.2. The biliary network

The biliary network is the conduit between the hepatocellular parenchyma of the liver and the lumen of the small intestine. Microscopic ductules are called bile canaliculi which are spaces of 0.5-2 μm wide formed between the neighboring hepatocytes (Ludwig et al., 1998; Boyer et al., 2006). A bile canaliculus is a dilated intercellular space between adjacent hepatocytes. Hepatocytes secrete bile into the canaliculi and bile flows parallel to the sinusoids but in the opposite direction of blood. At the ends of the canaliculi, bile flows into bile ducts. Bile duct is lined with simple cuboidal epithelium and collects the bile directly from the hepatocellular parenchyma via the canals of Herring (Takasaki and Hano, 2001). Small bile ducts anastomose into larger ductules and larger ducts eventually forming the common bile duct which dumps bile into the gall bladder. This is a sac-like structure adhering to the liver which has a duct that leads directly into the common bile duct.

2.1.3. Hepatocyte

Liver cell (hepatocyte) is a polyhedral cell about 20-30 μm in size, has a volume of approximately 5000 μm^3 (Boyer et al., 2006). It represents approximately 80% of the liver volume and 60 - 65% the total cell number proportion (Bacon et al., 2006; Boyer et al., 2006). Hepatocytes are epithelial cells, polarized with distinct apical, lateral and basal surfaces. The basal surfaces of hepatocytes face the sinusoidal endothelium (sinusoidal surface). The apical surfaces face adjacent hepatocytes and enclose the bile canaliculi (canalicular surface) while the lateral membranes of hepatocytes extend from the bile canaliculi to the space of Disse and form cell–cell junctions, including gap junctions (facilitate communication between hepatocytes) and tight junctions (seal the bile canalicular lumen from the interstitial space and prevent leakage of plasma into bile as well as backflow of bile from canaliculi into the blood). Hepatocytes have one nucleus although nearly 25% are binucleated (Bacon et al., 2006). The cytoplasm of the hepatocyte contains numerous mitochondria, a prominent Golgi apparatus located between the nucleus and the bile canaliculi, rough and smooth endoplasmic reticulum. Liver cells also contain numerous endosomes, lysosomes and peroxisomes. The lifespan of murine hepatocytes is approximately 400 days (Wang et al., 2011). Hepatocytes play significant roles in various aspects of liver pathophysiology.

2.1.4. Hepatic sinusoid and liver sinusoidal endothelial cells

The hepatic sinusoid has unique structures and functions as blood vessel. It serves as the main site of exchange between the blood and hepatocytes and characterized by presence of fenestrae (open pores in the wall) and lacking of basement membranes (Wisse, 1970; Braet and Wisse 2002; McCuskey, 2008). Liver sinusoidal endothelial cell constitutes the greatest proportion (approximately 70%) of the sinusoidal cells (Kuntz and Kuntz, 2008). The proportion of the total cell number is nearly 15-20% but they make up only 2.8% of the liver volume. These are flat cells and the nuclei camber the cell body. They form a continuous lining of the sinusoids which possess numerous intercellular spaces.

The diameter of this intercellular space (fenestrae) is 0.1-0.5 μm. Liver sinusoidal endothelial cells separated from the hepatocytes by a space of Disse. The space between the hepatocytes and the liver sinusoidal endothelial cells is called the space of Disse or the perisinusoidal space. The role of liver sinusoidal endothelial cell during pathophysiology is recently investigated in regenerating mouse livers (Ding et al., 2010; Hoehme et al., 2010). Also disruption of liver sinusoidal endothelial cell continuity enhances engraftment and integration of transplanted cells in damaged rat livers (Joseph et al., 2006).

2.1.5. Hepatic stellate cell (HSC)

Hepatic stellate cell is also known as Ito cell, perisinusoidal cells or lipocytes - referring to the main function of these cells in normal liver as fat storing cells (quiescent state). It lies in the space of Disse between the hepatocytes and the liver sinusoidal endothelial cell. Quiescent stellate cells represent 5-8% of the total number of liver cells (Geerts, 2001). During liver damage, stellate cells are able to change its phenotype into an activated state. The activated stellate cell is characterized by proliferation, contractility and chemotaxis. The amount of stored vitamin A decreases progressively during liver injury then the activated stellate cell is secreting collagen scar tissue (Stanciu et al., 2002) which can lead to fibrosis and subsequently cirrhosis. The role of stellate cells in chronic liver damage is well known and described in several reports (Bataller and Brenner, 2005; Friedman, 2008; Krizhanovsky et al., 2008).

2.2. Models of hepatic damage and regeneration responses

Liver has a unique capacity to detoxify different xenobiotics. This detoxification process evolved to protect the animals from plant and food toxins (Michalopoulos 2007). In addition to detoxification ability, the liver is able to regenerate and restore its original mass according to the functional requirements. The regenerative ability of liver has been described firstly in Hesiod’s Theogony (750 to 700 BC). Prometheus, a Titan, angered

Zeus by stealing fire and giving it to the primitive humans. Prometheus is punished by being chained to a rock in the Caucasus Mountains and an eagle was send to him each day to devour his liver. During the night, his damaged liver regenerated, leaving him fit for the next day's torture and so on (Ponfick, 1890). Today, several models have been established for liver regeneration studies in rodents. Among these models a single toxic dose of carbon tetrachloride (CCl_4) produces massive centrilobular hepatocyte necrosis (Hoehme et al., 2007; Hoehme et al., 2010; Zellmer et al., 2010).

2.2.1. Carbon tetrachloride induces centrilobular hepatocyte necrosis

A single dose of carbon tetrachloride (1.6 g/kg body weight in mice) leads to massive death of the centrilobular hepatocytes. The mouse livers are able to regenerate and restore the normal architecture within one week (Hoehme et al., 2007; Hoehme et al., 2010). These intoxication and regeneration processes are well-orchestrated and highly reproducible. The hepatotoxicity of carbon tetrachloride is a complex process involving toxicological and necro-inflammatory processes. The centrilobular hepatic damage results from the cytochrome P450 2E1-mediated bioactivation of carbon tetrachloride in the centrilobular hepatocytes (Shi et al., 1998; Manibusan et al., 2007) which have the highest concentration of cytochrome P450 2E1 (Raucy et al., 1993; Diaz Gómez et al., 2006). The bioactivation of carbon tetrachloride produces highly reactive free radical metabolites (Fig. 2.2) particularly trichloromethyl and/or trichloromethyl peroxyl free radicals (Poyer et al., 1980; Mico and Pohl 1983; Link et al., 1984; Slater et al. 1985). These radicals attack polyunsaturated fatty acids in membranes leading to impairment of cellular functions which depend on membrane integrity (Slater and Sawyer 1970; Benedetti et al., 1982; Lee et al., 1982; Tribble et al., 1987; Weber et al., 2003). This phenomenon is called lipid peroxidation. Eventually lipid peroxidation induces loss of cellular functions and cell death (Shah et al., 1979). The centrilobular pattern of carbon tetrachloride toxicity is similar to that caused in humans by an overdose of acetaminophen (Gunawan et al., 2006).

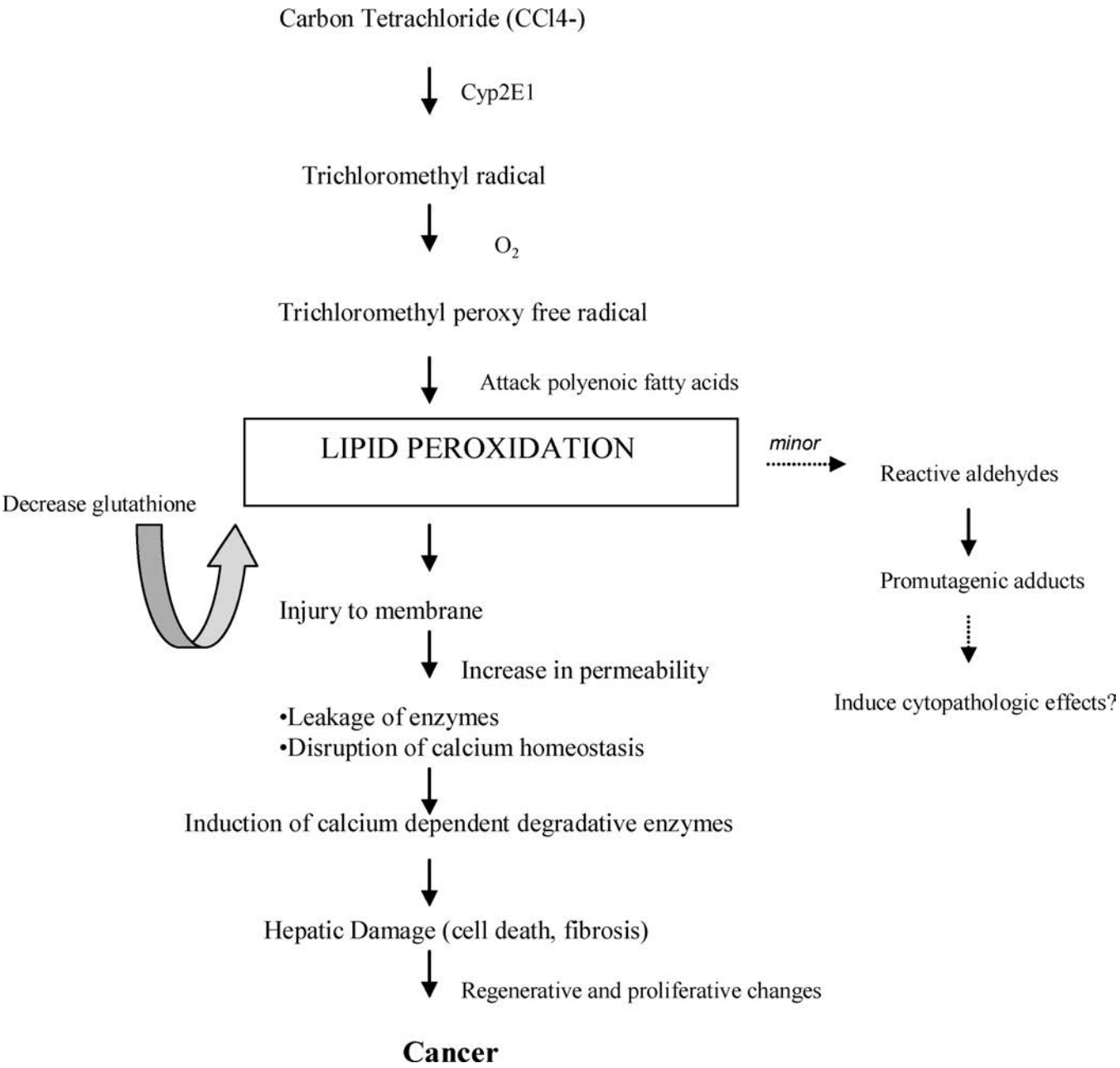

Figure 2.2. Postulated mechanism of the toxicological action of carbon tetrachloride. The bioactivation of carbon tetrachloride is mediated by cytochrome P450 2E1 resulting in formation of trichloromethyl radical. In presence of oxygen, the trichloromethyl radical is converted to trichloromethyl peroxy free radical. These radicals are able to attack the membranous fatty acids leading to lipid peroxidation. Therefore the integrity of the cell membrane is disrupted and eventually massive cell death occurred (Manibusan et al., 2007).

2.2.2. Prolonged administration of carbon tetrachloride induces septal fibrosis

Carbon tetrachloride is a chemical widely used to induce fibrosis in experimental animals (Bataller and Brenner, 2005). Prolonged administration of carbon tetrachloride leads to accumulation of collagen and extracellular matrix (Perez Tamayo, 1983; Krizhanovsky et al., 2008) in the perivenous compartment, extended between the central veins leading to pseudolobulation (Chobert et al., 2012). Later the fibrosis is bridged from the central to the portal areas of the liver lobule. In advanced cases, the cirrhosis and hepatocellular carcinoma (Fig. 2.2) are developed. Therefore carbon tetrachloride is an experimental model to study the pathogenesis of acute liver intoxication and regeneration, hepatic fibrosis and cirrhosis as well as hepatocellular carcinoma (Perez Tamayo, 1983). Liver fibrosis is a wound healing response to preserve liver integrity after dramatic continuous tissue destruction (Bataller and Brenner, 2005). Activated stellate cells (Bataller and Brenner, 2005; Radaeva et al., 2006; Friedman, 2008; Fujii et al., 2010) and myofibroblasts (Saile et al., 2002) are the main collagen producing cells in chronic liver diseases.

2.3. Hepatocellular polarity during liver regeneration

Biological tissues have both a robust architecture - required for tissue stability and resistance to stress - and a plasticity that allows tissue remodeling. Tissue homeostasis depends on the balance between robustness and plasticity of tissues, which is controlled by cell polarity (Lecuit and Lenne, 2007). Hepatocyte polarity is a precondition for the structural and functional aspects of hepatocytes therefore it is essential for liver function. The plasma membrane of epithelial cells is divided into two domains: an apical domain facing the external milieu and a basolateral domain in contact with the internal milieu and the blood supply (Kuntz and Kuntz, 2008). These plasma membrane domains have different lipid and protein constituents (Simons et al., 1988; van Meer et al., 1988). The general features of cell polarity have been described mostly in cultivated cells e.g., canine kidney cells (MDCK), drosophila or yeast (Handler 1989; Rodriguez-Boulan et

al., 1992; Cohen et al., 2004; Decaens et al., 2008; Martin-Belmonte and Mostov, 2008; McCaffrey and Macara, 2009; Wang et al., 2009; Shivas et al., 2010; Panbianco and Grotto, 2011) and primary murine hepatocytes (Godoy et al., 2010).

2.3.1. The basolateral surface of the hepatocyte

The basal surfaces of hepatocytes face the sinusoidal endothelium (sinusoidal surface). Hepatocytes have two or three non-contiguous basal surfaces (Dufour and Clavien, 2005) exposed to the perisinusoidal space of Disse. This includes transport of small molecules across the basal membrane, secretion of plasma proteins via fusion of secretory vesicles with the basal membrane and internalization of circulating macromolecules via clathrin-coated pits and vesicles (Bacon et al., 2006) also drug secretions as well as the uptake of recycled biliary salts (Decaens et al., 2008). The lateral membranes of hepatocytes extend from the bile canaliculi to the space of Disse and form cell–cell junctions, including gap and tight junctions. The basal and lateral membranes are frequently considered one unit, called the basolateral membrane and comprise nearly 85% of hepatocyte membrane (Kuntz and Kuntz, 2008). This membrane serves as: 1) a contact surface with hepatic sinusoids, where nutrients and blood constituents are exchanged between hepatocytes and hepatic sinusoids, and 2) hepatocyte-hepatocyte contact surface, where hepatocytes can communicate and exchange information with one another. There are several proteins expressed at the basolateral surface such as i) Low density lipoprotein receptor (LDLR) and ii) Epithelial-cadherin (E-cadherin).

2.3.2: The apical surface of the hepatocyte:

The apical surfaces of hepatocytes face adjacent hepatocytes and enclose the bile canaliculi (canalicular surface). At the apical poles several proteins are localized e.g. i) Dipeptidyl peptidase-4 (DPP4/CD26); ii) Multi-drug resistance associated protein 2 (Mrp2) and iii) phospho-Ezrin (Thr567)/Radixin (Thr564)/Moesin (Thr558). Hepatocyte

polarity is highly important for the physiological role of hepatocytes, such as canalicular bile secretion and simultaneous sinusoidal secretion of large quantities of serum proteins into blood. Hepatocyte polarity is compromised in many diseases like cholestasis (Wang and Boyer, 2004). In liver regeneration, the architecture of the organ is severely altered. However, there are no available in vivo studies in mice concerning hepatocyte polarity during different stages of the cell cycle. The maintenance and establishment of the hepatocellular polarity are not completely elucidated. Therefore this study investigated hepatocyte polarity during cell division in the regenerating liver.

2.4. Hepatic micro-architecture organization during intoxication and regeneration

During liver damage and regeneration, there are two principles established to guarantee a functional lobule structure. First, the sinusoidal endothelial cell guides the dividing hepatocytes during regeneration (Hoehme et al., 2010). Recently, it has been shown that the communication between the sinusoidal endothelial cells and the hepatocytes play pivotal roles in the hepatocyte proliferation. This communication takes place through cytokines e.g. hepatocyte growth factor (Ding et al., 2010). Second, the bile canalicular network establishment is critical for lobule architecture as well as hepatotoxicity. The bile canaliculus is established by the apical domains of the hepatocytes. The integrity of the apical membranes was investigated recently. Using in vivo imaging with two-photon microscopy, it was shown that paracetamol administration leads to rupture of the apical membrane, the bile floods backward to the hepatocyte leading to irreversible hepatocyte death. However, disruption of the basolateral membrane integrity is reversible and may be survived (Li et al., 2011). Currently, no technique is available to quantify the bile canalicular network.

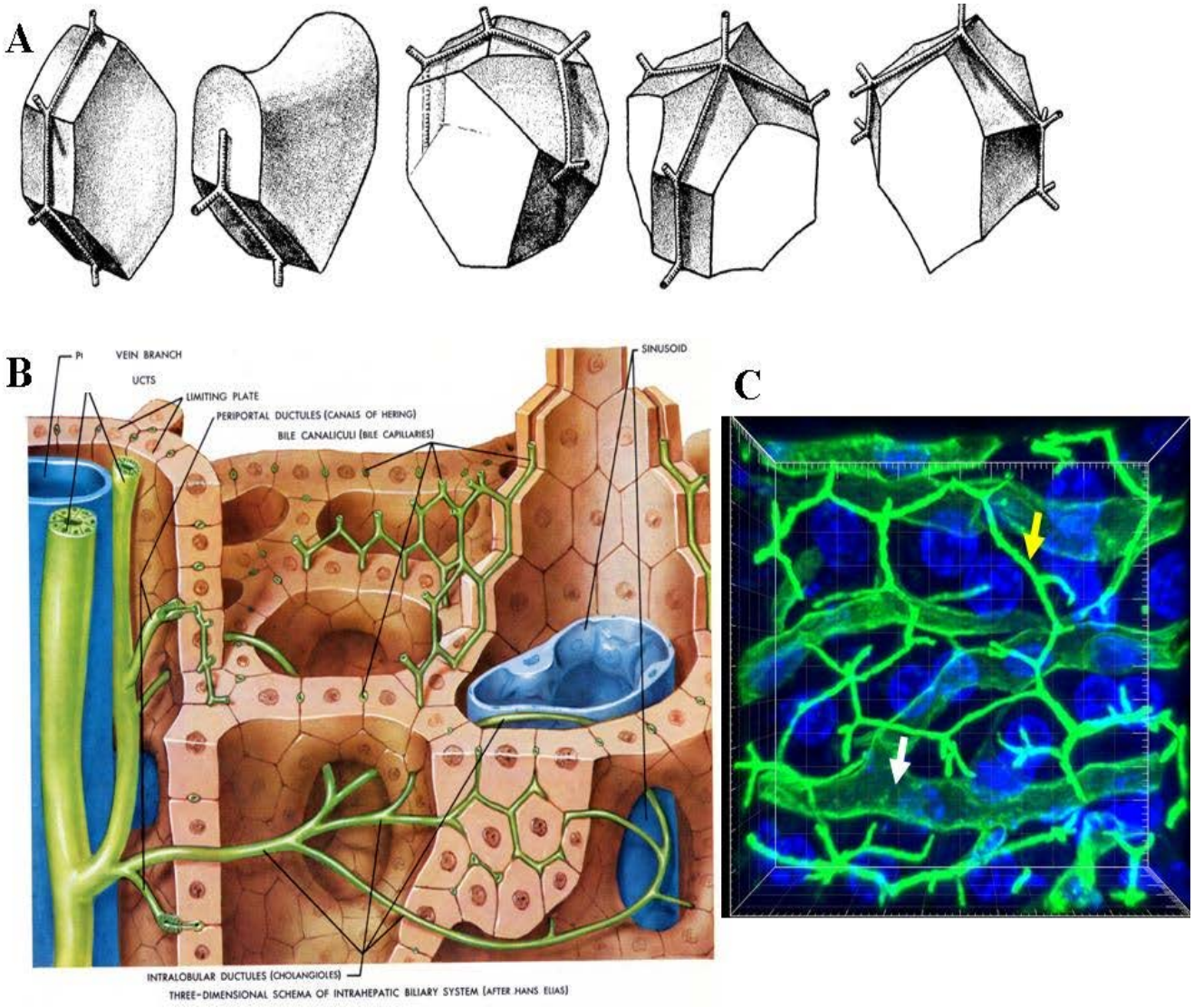

Figure 2.3. Organization of the bile canalicular network. A) Hepatocyte is a polygonal cell. Based on the hepatocyte shape, the bile canalicular network is organized. These schedules are described by Hans Elias (Elias, 1949). B) The bile canalicular network is organized as a hexagonal belt around the hepatocyte (Hansen and Koepen, 2002). C) Reconstructed Z-stack using Imaris software shows that the immunopositivity of DPPIV/CD26 at the bile canaliculi (yellow arrow) and the hepatic endothelial sinusoidal (white arrow) cells (Hoehme et al., 2010).

3. Material

3.1. Animals

To induce acute liver intoxication, male C57BL/6N mice, 8-12 weeks old were used (Charles River, Sulzfeld, Germany). For fibrosis induction, male C57BL/6J mice, 8-10 weeks old were used (Charles River, Sulzfeld, Germany). All protocols for experiments with animals were carried out in full compliance with the guidelines for animal care and were approved by the Animal Care Committee from the German government. The mice were kept under standard conditions and were fed ad libitum with Ssniff R/M-H, 10 mm standard diet (Ssniff, Soest, Germany).

3.2. Chemicals

4',6-Diamidino-2-phenylindol (DAPI)	Invitrogen, Darmstadt-Germany
5-Bromo-2'-deoxyuridine (BrdU)	Sigma-Aldrich Corp., MO-USA
Acetic acid (glacial)	Sigma-Aldrich Corp., MO-USA
Avidin/biotin blocking kit	Vector Lab, Dossenheim-Germany
Biotinylated solanum tuberosum lectin	Vector Lab., Burlingame, CA-USA
Bovine albumin fraction (BSA)	SERVA, Heidelberg-Germany
Carbon tetrachloride (CCl_4)	Carl Roth, Karlsruhe-Germany
Citric acid monohydrate	Carl-Roth, Karlsruhe-Germany
DAB peroxidase substrate	Vector Labor, Burlingame-USA
Direct red 80 (sirius red)	Sigma-Aldrich Corp., MO-USA
Di-sodium hydrogen phosphate anhydrous	Carl-Roth, Karlsruhe-Germany
Entellan	Merck, Darmstadt-Germany
Eosin-Y (water soluble)	Sigma-Aldrich Corp., MO-USA
Isopropanol (2-propanol 99.8%)	Carl-Roth, Karlsruhe-Germany
Ethyl alcohol (ethanol)	J.T.Baker, Griesheim-Germany
Fluorpreserve™ reagent	Merck, Darmstadt-Germany
Glucose	Carl-Roth, Karlsruhe-Germany

3.2. Chemicals (continued)

Glycerin	Merck, Darmstadt-Germany
Histoacryl® gewebekleber	B.Braun Melsungen AG-Germany
Hydrochloric acid (HCl)	Carl-Roth, Karlsruhe-Germany
Hydrogen peroxide (H_2O_2)	Carl-Roth, Karlsruhe-Germany
Mayer's hematoxylin	Merck, Langenfeld-Germany
Methanol	J.T.Baker, Griesheim-Germany
Paraffin	Leica Microsys., Wetzlar-Germany
Picric acid solution	Sigma-Aldrich Corp., MO-USA
Polyvinyl alcohol	Sigma-Aldrich, Steinheim-Germany
Potassium chloride (KCl)	Carl-Roth, Karlsruhe-Germany
Potassium di-hydrogen phosphate (KH_2PO_4)	Carl-Roth, Karlsruhe-Germany
Rotihistol	Carl-Roth, Karlsruhe-Germany
Roti-hitofix 4% (paraformaldehyde)	Carl-Roth, Karlsruhe-Germany
Sodium chloride (NaCl)	Carl-Roth, Karlsruhe-Germany
Sodium hydroxide	Sigma-Aldrich Corp., MO-USA
Streptavidin-horseradish peroxidase (HRPO)	Dianova, Hamburg-Germany
TRIS hydroxymethylaminomethane	Carl Roth, Karlsruhe-Germany
TritonX-100	Carl-Roth, Karlsruhe-Germany
Tween20	Sigma, Schnelldorf-Germany
Vectastain ABC kit (rabbit IgG)	Vector Lab., Dossenheim-Germany
Vectastain ABC kit (rat IgG)	Vector Lab., Dossenheim-Germany
Weigert's iron hematoxylin kit	Merck, Darmstadt-Germany
Xylene	Carl-Roth, Karlsruhe-Germany
Xylol (dimethylbenzene)	Merck, Darmstadt-Germany

3.3. Equipment

Analytical balance BL150S	Sartorius AG, Goettingen-Germany
Aperio image scanner	Aperio-Canada
Bright field microscopy (BX41)	Olympus GmbH, Hamburg-Germany
Centrifuge rotina 35R	Hettich GmbH, Tuttlingen-Germany
Compact balance CS200	Carl-Roth, Karlsruhe-Germany
Confocal laser scanning microscope	Olympus GmbH, Hamburg-Germany
Cutfix scalpel blades	B.Braun Melsungen AG-Germany
DAKO (delimiting) pen	Dakocytomation, Glostrup-Denmark
Eppendorf (microtube 0.5, 1 and 2ml)	Sarstedt, Numbrecht-Germany
Hybridizer	Dakocytomation, Glostrup-Denmark
Incubator	Binder GmbH, Tuttlingen-Germany
Microlance™ hypodermic needle- 26G	BD worldwide, Heidelberg-Germany
Microscope cover glass, Thermo scientific	Gerhard Menzel, Braunschweig-Germany
Microscope slide, Thermo scientific	Gerhard Menzel, Braunschweig-Germany
Microtome (microm-HM450)	Microm, Walldorf-Germany
Microwave Oven	Sharpe-Germany
Paraffin embedding cassettes	Carl-Roth, Karlsruhe-Germany
Parafilm® M	Carl-Roth, Karlsruhe-Germany
pH meter (seven easy PH S20)	VWR GmbH, Berlin-Germany
pH-Electrode blueline 14pH	Schott Instruments, Mainz-Germany
pH-Meter CG842	Schott Instruments, Mainz-Germany
Pipette, div.	Eppendorf, Wesseling-Berzdorf-Germany
Rotatory shaker	Edmund Buhler, Hechingen-Germany
ThermoMixer (model HTM 130L)	HLC Biotech, Bovenden-Germany
Tissue culture plate (6 and 24 wells)	Sarstedt, Numbrecht-Germany
Tubes (15 and 50ml)	Sarstedt, Numbrecht-Germany
Vibrating blade microtome (vibratome)	Leica Microsystems, Wetzlar-Germany

3.3. Equipment (continued)

Vibratome feather blades (blades VT)	Leica Microsystems, Wetzlar-Germany
Water bath JB1	Grant Instruments, Cambridgeshire-UK
Welted glasses	Carl-Roth, Karlsruhe-Germany

3.4. Antibodies

3.4.1. Primary antibodies

Antibody characteristics, manufacturer and source are given in Table 3.1.

Table 3.1. Panel of primary antibodies used in the study

Antibody	**Raised in**	**Cat.NO**	**Company**
Anti-BrdU, clone BU1/75 (ICR1)	Rat	MCA2060	AbD Serotec, Dusseldorf-Germany
Anti-glutamine synthetase	Rabbit	G2781	Sigma Aldrich, Missouri-USA
Anti-mouse DPPIV/CD26	Goat	AF954	R&D systems, Minneapolis, MN, USA
Anti-mouse LDL-R	Goat	AF2255	R&D systems, Nordenstadt-Germany
Anti-alpha–tubulin, FITIC conjugated	Mouse	F2168	Sigma Aldrich, Missouri-USA
Anti-ICAM-1	Rabbit	10020-1-AP	ProteinTech Group, Chicago-USA
Anti-Mrp2 K13	Rabbit	-	Gift from Dr. Bruno Stieger
Anti-E-cadherin (24E10)	Rabbit	#3195	Cell Signaling Technology, Frankfurt-Germany
Anti-claudin1	Rabbit	ab15098	Abcam, Cambridge-UK
Anti-alpha smooth muscle actin	Rabbit	ab5694	Abcam, Cambridge-UK
Anti-collagen III	Rabbit	ab7778	Abcam, Cambridge-UK

Table 3.1. Panel of primary antibodies used in the study (continued)

Antibody	Raised in	Cat.NO	Company
Alexa Fluor 488-conjugated phalloidin	-	A12379	Invitrogen, Darmstadt-Germany
Anti-Phospho-Ezrin (Thr567) /radixin (Thr564)/moesin (Thr558)	Rabbit	#3141	Cell Signaling Technology, Frankfurt-Germany

3.4.2. Secondary antibodies

Antibody characteristics, manufacturer and source are given in Table 3.2.

Table 3.2. Panel of secondary antibodies used in the study

Antibody	Conjugated	Raised in	Company
Anti-goat IgG	488	Donkey	Dianova, Hamburg-Germany
Anti-goat IgG	Cy3	Donkey	Dianova, Hamburg-Germany
Anti-goat IgG	Cy5	Donkey	Dianova, Hamburg-Germany
Anti-goat IgG	649	Donkey	Dianova, Hamburg-Germany
Anti-goat IgG	AlexaFluor®546	Donkey	Invitrogen, Darmstadt-Germany
Anti-rabbit IgG	AlexaFluor®555	Goat	Invitrogen, Darmstadt-Germany
Anti-rabbit IgG	488	Donkey	Dianova, Hamburg-Germany
Anti-rabbit IgG	Cy3	Donkey	Dianova, Hamburg -Germany
Anti-rabbit IgG	649	Donkey	Dianova, Hamburg-Germany
Anti-mouse IgG	Cy2	Donkey	Dianova, Hamburg-Germany

Table 3.2. Panel of secondary antibodies used in the study (continued)

Antibody	**Conjugated**	**Raised in**	**Company**
Anti-mouse IgG	488	Donkey	Dianova, Hamburg-Germany
Anti-mouse IgG	Cy3	Donkey	Dianova, Hamburg-Germany
Anti-mouse IgG	649	Donkey	Dianova, Hamburg-Germany
Anti-rat IgG	488	Donkey	Dianova, Hamburg-Germany
Anti-rat IgG	Cy3	Donkey	Dianova, Hamburg-Germany
Anti-rat IgG	649	Donkey	Dianova, Hamburg-Germany
Anti-mouse IgG	AlexaFluor®555	Goat	Invitrogen, Darmstadt-Germany
Anti-rabbit IgG	AlexaFluor®514	Goat	Invitrogen, Darmstadt-Germany
Anti-rat IgG	Alexa Fluor®488	Donkey	Invitrogen, Darmstadt-Germany
Anti-rat IgG	SP-Biotin	Goat	Dianova, Hamburg-Germany
Streptavidin	Cy2	-	Dianova, Hamburg-Germany
Streptavidin	Cy3	-	Dianova, Hamburg-Germany
Streptavidin	Cy5	-	Dianova, Hamburg-Germany
Phalloidin	Alexa Fluor®488	-	Invitrogen, Darmstadt-Germany
Anti-mouse IgG	SP-Biotin	Goat	Dianova, Hamburg-Germany

3.5. Preparation of buffers and reagents

3.5.1. 10X phosphate buffered saline (10X PBS)

Substance	weight [mmol/l]
NaCl	1370
KCl	27
KH_2PO_4	15
Na_2HPO_4	81
$Na_2HPO_4*7H_2O$	81

The pH was adjusted to 7.4 using a pH meter

The final volume was made up to 1000 ml with distilled water.

For 1 liter 1X PBS: To 900 ml of distilled water, 100 ml of prepared 10X PBS was added and mixed well.

3.5.2. 10X Tris-buffered saline (10X TBS)

Substance	weight [mmol/l]
NaCl	137
KCl	2.7
TRIS	25

The pH was adjusted to 7.4 using a pH meter

The final volume was made up to 1000 ml with distilled water.

For 1 liter 1X TBS: To 900 ml of distilled water, 100 ml of prepared 10X TBS was added and mixed well.

3.5.3. Preservation buffer

Substance	weight [ml]
Glucose (30%)	500
Roti®-Histofix 4%	500
This mixture was stored at 4°C	

This buffer is used to keep liver lobes or slices for at least 6 months without architectural interferences with respect to hepatic micro- architecture.

3.5.4. Carbon tetrachloride (CCl_4) solution

The dose of CCl_4 was 1.6 g/kg body weight (Hoehme et al., 2010 and Zellmer et al., 2010) and was prepared as follows: to 3 ml of olive oil, 1 ml of carbon tetrachloride was added and mixed well.

3.5.5. Bromodeoxy uridine (BrdU) solution

BrdU is a synthetic analog of thymidine that incorporates into a cell's DNA during cell division, more specifically during the S-phase of the cell cycle. Antibodies against BrdU can be used to label these cells thereby providing visual evidence of S-phase cells.

Substance	Concentration [mmol/l]
BrdU	500
Few drops of 1M NaOH were added.	
The final volume was made up to 1000 ml with distilled water.	

3.5.6. Antigen retrieval agent

To 800 ml of distilled water, 2.1 g of citric acid monohydrate was added and the pH adjusted to 6.0. The final volume was brought to 1 liter with distilled water to produce a final concentration of 0.01 M. The pretreatment of liver tissue with the antigen retrieval

reagent significantly improved the availability of antigens through break down of the protein cross-links formed by formalin fixation and uncovering hidden antigenic sites.

3.5.7. DNA denaturation agent

The 2N hydrochloric acid (HCl) was prepared as follows: To 10 ml of distilled water, 10 ml of HCl (4 mol/l) was added and mixed well. To measure cell proliferation or DNA synthesis, 5-bromo2'-deoxy-uridine (BrdU) incorporates into DNA in place of thymidine. Incorporation of BrdU into DNA can be detected using an antibody against BrdU. The binding of the antibody to BrdU is achieved through DNA denaturation by exposing the cells to acid (HCl) and/or heat.

3.5.8. Blocking serum

To 99 ml of 1X PBS, 3 g of protease free bovine albumin fraction V and 1 ml of Tween20 were added and mixed well. Aliquots of 10 ml were prepared and stored at -20°C. The incubation of liver sections with 3% bovine serum albumin (BSA) reduces non-specific binding of the antibodies due to hydrophobic interaction.

3.5.9. Dilution buffer

To 99 ml of 1X PBS, 0.3 g of protease free bovine albumin fraction V and 1 ml of Tween20 were added and mixed well. Aliquots of 10 ml were prepared and were stored at -20°C. Primary and secondary antibodies were diluted in this buffer to reduce non-specific binding due to hydrophobic interaction.

3.5.10. DAPI solution

To 10 ml of distilled water, 1µl of 4',6-Diamidino-2-phenylindol (DAPI) was added and mixed well. The DAPI is used to counterstain nucleic acid.

3.5.11. Mounting media (Mowiol)

To 6.0 g of glycerol, 2.4 g of polyvinyl alcohol 40-88 was added and mixed well for one hour at room temperature. Six ml of distilled water was then added and mixed well for

two hours at room temperature. Subsequently, twelve ml of 0.2 M Tris/HCl was added, and the mixture incubated overnight at 4ºC. The mixture was then transferred to 50 ml tube and incubated for 30 minutes in a water bath at 50ºC followed by centrifugation at 4000 rpm at room temperature for 30 minutes. The supernatant was poured into a 2 ml eppendorf tube and stored at -20ºC. Mowiol is a glycerol-based solution containing an inhibitor that retards photobleaching of fluorochrome and enhances the visualization of signals when viewed under a fluorescent microscope.

3.5.12. Mayer's hematoxylin

To 160 ml of distilled water, 40 ml of Mayer's hematoxylin was added, mixed well and was stored at room temperature.

3.5.13. Eosin

To 200 ml of distilled water, 4 g of 4% Eosin-Y (water soluble) was added, mixed well and was stored at room temperature.

3.5.14. Picro-sirius red solution

To 500 ml of saturated aqueous solution of picric acid, 0.5 g of Sirius red was added, mixed well and was stored at room temperature.

3.6. Software

Cell^F	Olympus GmbH, Hamburg - Germany
Fluoview1000	Olympus GmbH, Hamburg - Germany
Aperio imagescope software	Aperio - Canada
Image J	National Institutes of Health's NIH Image
Positive pixel count v9 (version 9.1)	Aperio - Canada
Imaris 7.4	Bitplane - Zurich
SPSS statistics 20	IBM - USA

4. Methods

4.1. Animal experiments

4.1.1. Administration of carbon tetrachloride and BrdU

Male C57BL/6N mice were treated intraperitoneally with a single dose of carbon tetrachloride (1.6 g/kg body weight) dissolved in olive oil (Hoehme et al., 2010; Zellmer et al., 2010). A control group received olive oil only. Mice received three doses through intraperitoneal injection of BrdU (80 mg/kg body weight in 0.9% NaCl solution) at 2, 4 and 6 hours before preparation of the livers (Fig. 4.1). Mice were sacrificed by cervical dislocation. Three mice were used for each of the time period.

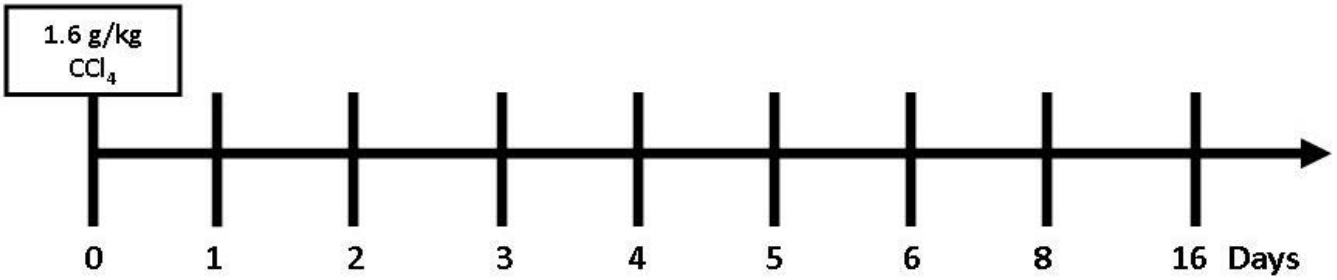

Figure 4.1. Experimental design of the spatial-temporal modeling of liver intoxication and regeneration. The mice were exposed intraperitoneally to carbon tetrachloride and received three doses of BrdU before liver preparation. Three mice were analyzed per time interval.

4.1.2. Hepatocellular polarity during liver regeneration

To investigate the establishment of the bile canaliculi between the daughter hepatocytes, male C57BL/6N mice were treated intraperitoneally with a single dose of carbon tetrachloride (1.6 g/kg body weight). A control group received vehicle only. The mice then received 80 mg/kg of BrdU at 46 hours after intoxication during the maximum level of hepatocyte proliferation. Liver tissues were harvested from the intoxicated as well as control mice (Fig. 4.2). Three mice were analyzed per time interval. The BrdU has been incorporated into the cell's DNA during cell division. Therefore, it could be used to label the daughter cells.

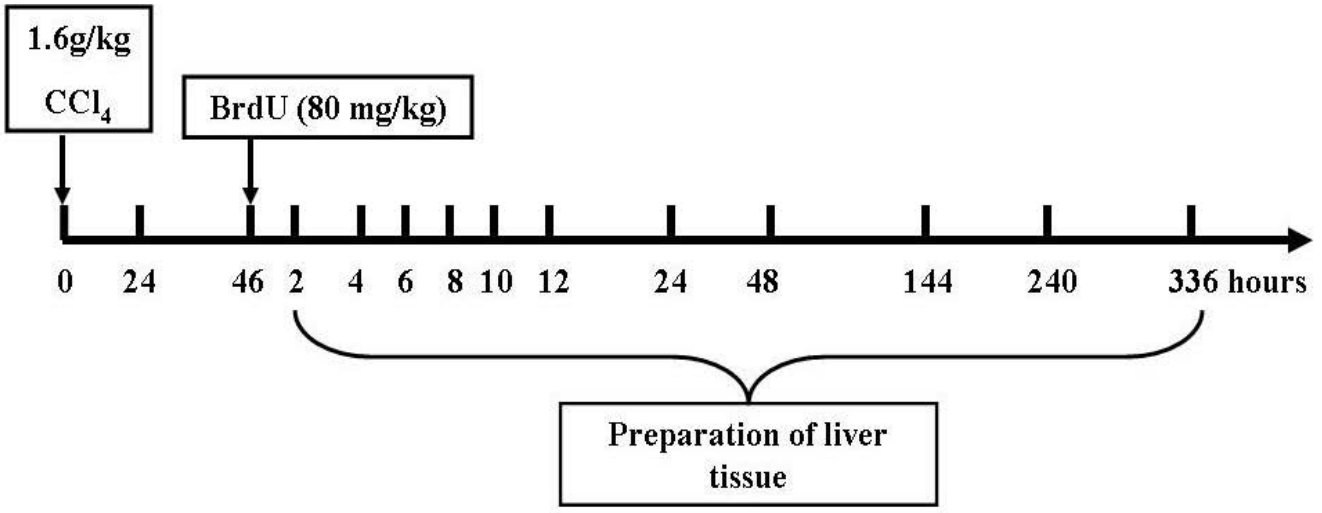

Figure 4.2. Experiment for establishment of a novel bile canaliculus between the daughter cells. The mice were exposed to a single dose of carbon tetrachloride intraperitoneally. A control group received olive oil only. Subsequently, the mice received 80 mg/kg of BrdU at 46 hours after carbon tetrachloride. Liver tissues were prepared at different time points after intoxication as well as from control animals. Three mice were analyzed per time interval.

4.1.3. Induction of liver fibrosis

In order to investigate the alterations in the hepatic micro-architecture after repetitive doses of carbon tetrachloride, male C57BL/6J mice were used. Administration regimen was thrice a week for six consecutive weeks. Carbon tetrachloride (1.6 g/kg body weight) was suspended in olive oil and injected intraperitoneally (Krizhanovsky et al., 2008). A control group received vehicle only. Mice were sacrificed 48 hours after the last carbon tetrachloride injection. Five mice were used for each of the time point. Liver tissues were harvested from the treated as well as control mice.

4.1.4. Excision and fixation of liver lobes

At the end of experiment, the mice were sacrificed by cervical dislocation. The abdominal cavity was immediately opened and the whole liver carefully excised. The tissue was then separated into two parts: The first part was stored in 4% paraformaldehyde for embedding in paraffin. The second part was preserved in 4%

paraformaldehyde for three days followed by a buffer containing 2% paraformaldehyde and 15% glucose (Hoehme et al., 2010). This part was used for immunofluorescence staining of deep liver slices.

4.2. Preparation of liver tissue for histology and immunohistochemistry

4.2.1. Embedding of the liver lobes on paraffin

The left liver lobe was collected in paraffin embedding cassettes and stored in 4% paraformaldehyde for 48 hours at 4°C. Formalin-fixed liver was washed in 1X PBS for 48 hours and dehydrated through an ethanol series (three times, 5 minutes each in 70%, 90%, 95% and 100% ethanol). Liver sections were incubated four times in xylene and then were incubated over night in xylene/paraffin (1:1) at 60°C. Subsequently, tissue specimens incubated twice in 60°C paraffin for three hours, followed by paraffin embedding. The paraffin was heated in the heat abele vessels up to 62°C, the Microm STP was started and the liver tissue was embedded.

4.2.2. Preparation of vibratome liver slices for immunostaining

Immediately before staining, the median liver lobe was sliced using a vibrating blade microtome. The liver lobe was fixed in the specimen holder using glue for two minutes. The buffer tray and specimen holder were installed in the vibratome and the buffer tray filled with 1X PBS to cover the liver lobe. Subsequently, a vibratome feather blade was tightly fixed into the knife holder and installed in the vibratome. The slicing settings were adjusted to 75 μm thickness and low velocity.

4.3. Principles of immunohistochemistry and immunofluorescence staining

Immunohistochemistry protocol is used to detect specific proteins in the cells or tissues. For BrdU, glutamine synthetase and alpha-smooth muscle action immunostaining, I used the Avidin-Biotin Complex (ABC) Method. The protocol is based on the immunostaining protocols recommended by the Cell signaling and Abcam companies from which most of the antibodies were purchased, with slight modifications. This

technique includes three steps: 1) unlabeled primary antibody, 2) biotinylated secondary antibody and 3) complex of avidin-biotin peroxidase. Subsequently, the peroxidase is developed by the DAB substrate producing a brown end product (Fig. 4.3).

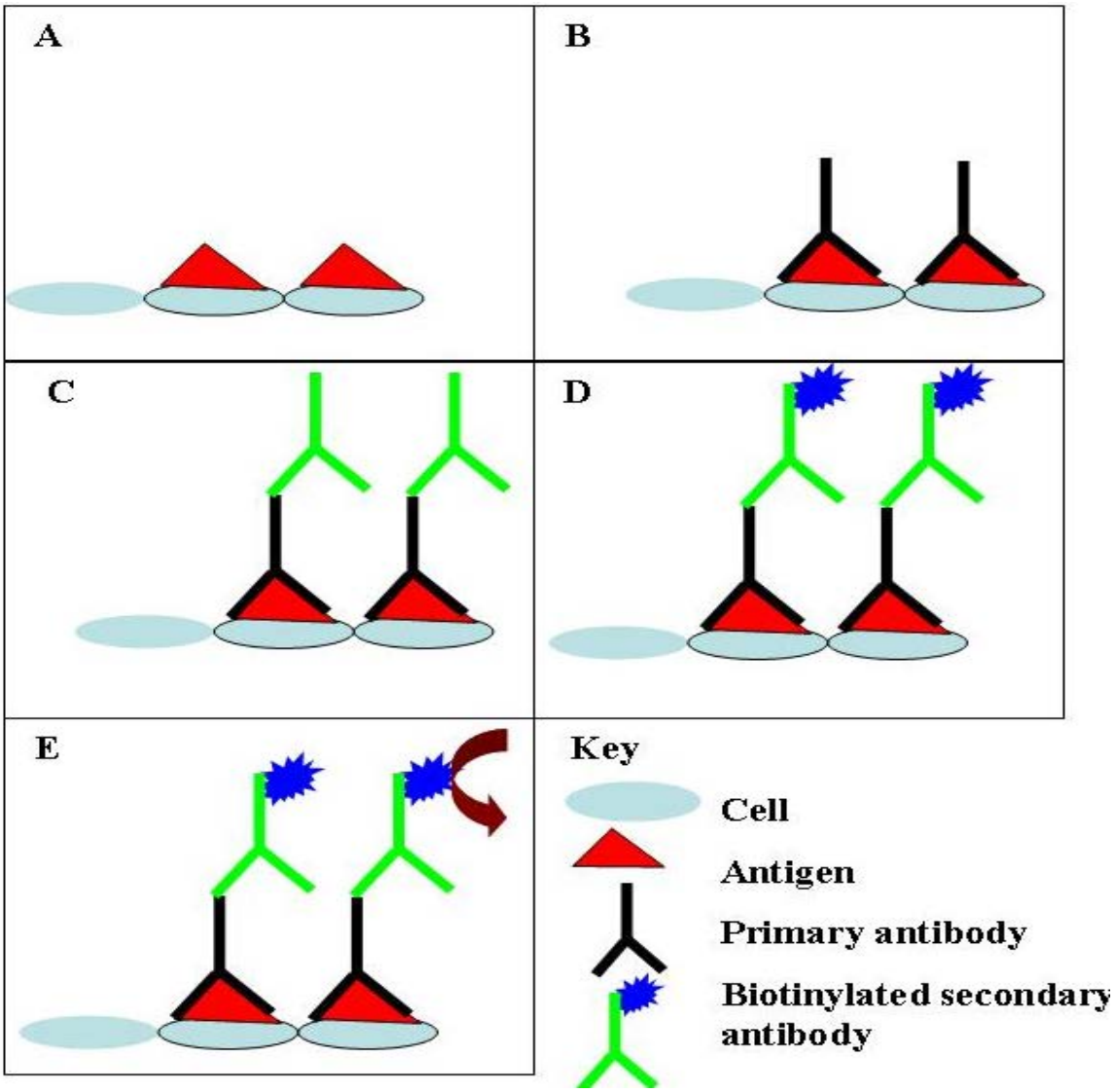

Figure 4.3. Immunohistochemistry protocol of formalin fixed paraffin embedded sections. A) preparation of liver sections includes deparaffinization and rehydration of the liver sections in rotihistol and graded ethanol, antigen retrieval using heated citrate buffer, blocking of endogenous peroxidase using H_2O_2 and blocking of unspecific binding by BSA, B) incubation of liver sections with primary antibodies, C) incubation with biotinylated secondary antibodies D) liver sections incubated with horse radish peroxidase and E) enzymatic detection using the DAB system.

For immunofluorescence staining, both direct (Fig. 4.4A) and indirect (Fig. 4.4B) protocols were used.

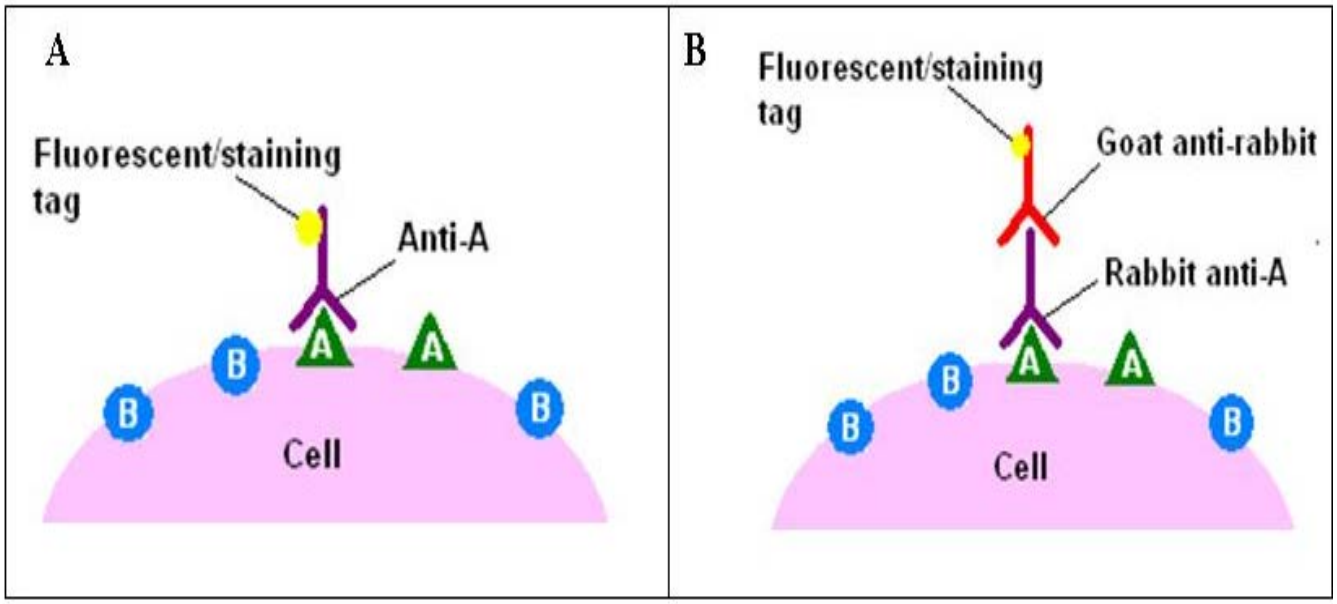

Figure 4.4. Immunofluorescence protocol of vibratome prepared slices. A) Direct immunofluorescence method (A). The primary antibody is chemically linked to a fluorophore. B) Indirect method where an unlabeled primary antibody specifically binds the target antigen and the fluorophore-labeled secondary antibody recognizes the primary antibody (source: en.wikipedia.org/wiki/Immunohistochemistry).

4.4. Liver histology and immunohistochemistry

4.4.1. Hematoxylin and eosin (H&E) staining

The formalin-fixed paraffin embedded sections were stained by H&E using a standard method. The tissue sections were deparaffinized through three washes, 10 minutes each in rotihistol. They were rehydrated in graded isopropanol (98%, 96%, 90%, 80% and 70%) each for 5 minutes. After washing the tissue section in distilled water for 5 minutes, the sections were incubated with Mayer's hematoxylin for 5 minutes and then were washed under running tape water for 15 minutes. Subsequently, the sections were incubated for three minutes in 4% eosin, followed by a short wash in distilled water to remove the eosin. After washing the tissue sections in graded isopropanol for 10 seconds, the sections were washed twice in 100% isopropanol, each was minutes. The

tissue sections were then washed three times in rotihistol and were mounted using entellan. The slides were scanned shortly after the staining procedure using the bright field microscopy BX41.

4.4.2. Picro-sirius red staining

The formalin-fixed paraffin embedded sections were stained by picro-sirius red as described by (Junqueira et al., 1979; Krizhanovsky et al., 2008). The paraffin embedded tissue sections were deparaffinized through three washes, 10 minutes each in rotihistol. Liver sections were rehydrated in graded ethanol (98%, 96%, 90%, 80% and 70%) each for 5 minutes. The nuclei were counterstained using Weigert's haematoxylin for 8 minutes and the sections were washed once in 1X TBS and 10 minutes under running tape water. Subsequently, the sections were incubated for one hour in picro-sirius red and were washed twice in acidified water. Then the sections were dehydrated using the graded ethanol (70%, 90%, 95%, and 100% ethanol, each was 10 seconds) and the sections were washed in rotihistol. The tissue sections were mounted using entellan and stored in the dark at room temperature until further analysis.

4.4.3. Immunohistochemistry of BrdU

BrdU immunohistochemistry was performed as described previously (Hoehme et al., 2010) with slight modifications. Deparaffinization of the tissue sections was done using rotihistol 4 times and the rehydration was performed using descending ethanol gradients (100%, 95%, 90%, 70%, 50% and 30% ethanol, for 5 minutes each). Tissue sections were then heated twice in a microwave oven, 7 minutes each, in 0.01M citrate buffer (pH 6.0). The tissue sections were washed three times in 1X PBS. Subsequently, the tissue sections were incubated for 10 minutes in 2N HCl at room temperature. After washing in 1X PBS, the tissue sections were incubated for 30 minutes in a solution of 7.5% H_2O_2 in methanol to block endogenous peroxidase. All incubations were done in a humidified chamber. To block unspecific binding sites, the tissue sections were incubated in 3% BSA / 0.1% Tween^{R}20 in 1X PBS for 60 minutes. Subsequently,

endogenous biotin and avidin were blocked using DAKO kit which was prepared according to the manufacturer's instructions. Then the blocking solution was dripped off carefully - without washing steps - the tissue sections were incubated with antibodies directed against BrdU (raised in rat, 1:1000) for one hour at room temperature. The tissue sections were subsequently washed three times in 1X PBS. Biotinylated secondary antibodies (raised in goat, 1:250) were selected to bind specifically with the primary antibodies. After 60 minutes incubation at room temperature, the tissue sections were washed again three times in 1X PBS. The tissue sections were incubated with streptavidin-horseradish peroxidase (1:500) for 60 minutes at room temperature. Both primary and secondary antibodies as well as streptavidin-horseradish peroxidase were diluted in 0.3% BSA / 0.1% Tween^{R}20 in 1X PBS. The tissue sections were then washed three times in 1X PBS and were incubated for 5 minutes at room temperature with freshly prepared DAB solution according to the manufacturer's instructions (VectorLab). After this, the tissue sections were rinsed for 5 minutes using distilled water and then were counterstained using Mayer's hematoxylin for 2 minutes. Subsequently, the tissue sections were rinsed for 10 minutes under running tap-water and then dehydrated using the graded ethanol (70%, 90%, 95%, and 100% ethanol, each was 10 seconds). The tissue sections were washed in rotihistol, were mounted using entellan and were stored in the dark at room temperature until further analysis.

4.4.4. Immunohistochemistry of glutamine synthetase (GS)

Glutamine synthetase immunohistochemistry was performed as described previously (Brauening et al., 2010; Hoehme et al., 2010; Schreiber et al., 2011) with slight modifications. Deparaffinization of tissue sections was done using rotihistol four times, and then the sections were hydrated using descending ethanol gradients (100%, 95%, 90%, 70%, 50% and 30% ethanol, for 5 minutes each). Tissue sections were then heated twice in a microwave oven, 7 minutes each, in 0.01M citrate buffer (pH 6.0). After washing in 1X PBS, the tissue sections were incubated for 30 minutes in a solution of

7.5% H_2O_2 in methanol to block endogenous peroxidase. All further incubations were done in a humidified chamber. To block unspecific binding sites, the tissue sections were incubated in 3% BSA / 0.1% Tween^{R}20 in 1X PBS for 60 minutes. To block the endogenous biotin and avidin, tissue sections were incubated with DAKO kit reagents and the incubation was done according to the manufacturer's instructions. Then the blocking solution was dripped off carefully (without washing steps) the tissue sections were incubated with the primary antibody (rabbit anti-GS, 1:1000) for 60 minutes at room temperature. The tissue sections were subsequently washed three times in 1X PBS. Biotinylated secondary antibodies (raised in goat, 1:250) were selected to bind specifically with the primary antibodies. After 60 minutes incubation at room temperature, the tissue sections were washed again three times in 1X PBS. The tissue sections were incubated with streptavidin-horseradish peroxidase (1:500) for 60 minutes at room temperature. Both primary and secondary antibodies as well as streptavidin-horseradish peroxidase were diluted in 0.3% BSA / 0.1% Tween^{R}20 in 1X PBS. The tissue sections were then washed three times in 1X PBS and were incubated for 5 minutes at room temperature with freshly prepared DAB solution according to the manufacturer's instructions (VectorLab). The tissue sections were rinsed for 5 minutes using distilled water and then counter stained using Mayer's hematoxylin for 2 minutes. Subsequently, the tissue sections were rinsed for 10 minutes under running tap-water and then dehydrated using the graded ethanol (70%, 90%, 95%, and 100% ethanol, each was 10 seconds) and then the tissue sections were washed in rotihistol. The tissue sections were mounted using entellan and were stored in the dark at room temperature until further analysis.

4.4.5. Immunohistochemistry of alpha-smooth muscle actin (α-SMA)

Alpha-smooth muscle actin (α-SMA) immunohistochemistry was performed according to (Krizhanovsky et al., 2008) with slight modifications. The tissue sections were deparaffinized using rotihistol four times, and then the sections were rehydrated using

descending ethanol gradients (100%, 95%, 90%, 70%, 50% and 30% ethanol, for 5 minutes each). The tissue sections were then heated twice in a microwave oven, 7 minutes each, in 0.01M citrate buffer (pH 6.0). The tissue sections were incubated for 30 minutes in a solution of 7.5% H_2O_2 in methanol to block endogenous peroxidase. All further incubations were done in a humidified chamber. To block unspecific binding sites, the tissue sections were incubated in 3% BSA / 0.1% Tween^{R}20 in 1X PBS for 60 minutes. Subsequently, the endogenous biotin and avidin were blocked using a commercially (DAKO) available kit according to the manufacturer's instructions. Then the blocking solution was dripped off carefully (without washing steps). The tissue sections were incubated with the primary antibody (rabbit anti-α-SMA, 1:250) for two hours at room temperature. The tissue sections were subsequently washed three times in 1X PBS. Biotinylated secondary antibodies (raised in goat, 1:250) were selected to bind specifically with the primary antibodies. After one hour incubation at room temperature, the tissue sections were washed again three times in 1X PBS. The tissue sections were incubated with streptavidin-horseradish peroxidase (1:500) for one hour at room temperature. Both primary and secondary antibodies as well as streptavidin-horseradish peroxidase were diluted in 0.3% BSA / 0.1% Tween^{R}20 in 1X PBS. The tissue sections were then washed three times in 1X PBS and were incubated for 5 minutes at room temperature with freshly prepared DAB solution according to the manufacturer's instructions (VectorLab). After this, the tissue sections were rinsed for 5 minutes using distilled water and then counter stained using Mayer's hematoxylin for 2 minutes. Subsequently, the tissue sections were rinsed for 10 minutes under running tap-water and then dehydrated using the graded ethanol (70%, 90%, 95%, and 100% ethanol, each was 10 seconds). The tissue sections were washed in rotihistol, were mounted using entellan and were stored in the dark at room temperature until further analysis.

4.5. Immunofluoresence staining using vibratome slices

4.5.1. Architectural staining

Freshly vibratome sliced tissue sections (75 µm thick slices) were used to investigate the hepatic micro-architecture during liver intoxication, regeneration and fibrosis. This protocol has been published on the virtual liver network (VLN) website as SOP (Brauening et al., 2010; Schreiber et al., 2011). The slices were washed three times in 1X PBS. Freshly prepared citrate buffer was heated for 2 minutes in a microwave. Three ml of heated buffer were poured in a well of a 6 well plate and the slices were moved and incubated into the heated buffer for two minutes. During incubation, the buffer was heated for two minutes and the previous step was repeated 10 times. Subsequently, the slices were cooled down to room temperature for ten minutes and washed three times in 1X PBS. Unspecific binding sites were blocked using 3% BSA/1% Tween^{R}20 in 1X PBS for two hours at room temperature, followed by incubation with anti-glutamine synthetase (raised in rabbit, 1:2000) and anti-msDPPIV/CD26 (raised in goat, 1:100) overnight at 4°C. Subsequently, the slices were washed three times in 1X PBS and incubated with Cy3-conjugated anti-rabbit (raised in donkey, 1:100), 488-conjugated anti-goat (raised in donkey, 1:100) and 649-conjugated anti-mouse (raised in donkey, 1:750) as secondary antibodies overnight at 4°C. Primary and secondary antibodies were diluted in 0.3% BSA/1% Tween^{R}20 in 1X PBS. All steps were done on a shaker (200 rpm). The slices were washed three times in 1X PBS and were incubated in freshly prepared DAPI solution for 90 minutes in the dark. The slices were washed three times in 1X PBS and were mounted using mowiol or fluorpreserve™ reagent. Then the slides were stored at 4°C until further analysis.

4.5.2. Proliferation staining

Freshly vibratome sliced tissue sections (75 µm thick slices) were used to investigate the proliferation status of hepatocytes during liver regeneration after intoxication. This protocol has been published on the virtual liver network (VLN) as SOP. The slices were

washed three times in 1X PBS, 1.25 ml of freshly prepared citrate buffer was pipetted in a 2ml tube and the slices were cooked using thermomixer at 95°C for 25 minutes with shaking. Then, the slices were cooled down to room temperature for ten minutes and were washed three times in 1X PBS. Subsequently, the tissue sections were incubated for ten minutes in 2N HCl at room temperature. After three washing steps in 1X PBS, unspecific binding sites were blocked using 3% BSA/1% Tween^{R}20 in 1X PBS for two hours at room temperature and without washing the slices were incubated with anti-BrdU (raised in rat, 1:500) overnight at 4°C. Subsequently, the slices were washed three times in 1X PBS and were incubated with dylight 488-conjugated anti-rat (raised in donkey, 1:100) as a secondary antibody overnight at 4°C. Then, the slices were washed 3 times in 1X PBS and were incubated with anti-glutamine synthetase (raised in rabbit, 1:2000) overnight at 4°C. After this incubation, the slices were washed three times in 1X PBS and were incubated with Cy3-conjugated anti-rabbit (raised in donkey, 1:100) and dylight 649-conjugated anti-mouse (raised in donkey, 1:750) as secondary antibodies overnight at 4°C. Both primary and secondary antibodies were diluted in 0.3% BSA/1% Tween^{R}20 in 1X PBS. All steps were done on a shaker (200 rpm). The slices were washed three times in 1X PBS and were incubated in freshly prepared DAPI solution for 90 minutes in the dark. The slices were washed three times in 1X PBS and were mounted using mowiol or fluorpreserve™ reagent. Then the slides were stored at 4°C until further analysis.

4.5.3. Co-staining of BrdU and different membrane markers

Freshly vibratome sliced tissue sections (75 µm thick slices) were used to investigate the existence of different membrane markers during hepatocyte proliferation (S-phase). The same protocol described in section 4.5.2 was used. The slices were incubated with anti-BrdU (raised in rat, 1:500). Subsequently, the slices were incubated with 488-conjugated anti-rat (raised in donkey, 1:100) as a secondary antibody overnight at 4°C. Then, the slices were incubated overnight at 4°C with one of the following antibodies: 1) anti-

msDPPIV/CD26 (raised in goat, 1:100); 2) anti-Mrp2 (raised in rabbit, 1:1000); 3) anti-Phospho-Ezrin (Thr567)/Radixin (Thr564)/Moesin (Thr558) (raised in rabbit, 1:250); 4) anti-msLDLR (raised in goat, 1:25), 5) anti-E-cadherin (raised in rabbit, 1:100) or 7) anti-claudin1 (raised in rabbit, 1:50). After this incubation, the slices were washed three times in 1X PBS and incubated with Cy3-conjugated anti-goat (raised in donkey, 1:100) or Cy3-conjugated anti-rabbit (raised in donkey, 1:100) as secondary antibodies overnight at 4°C. Primary and secondary antibodies were diluted in 0.3% BSA/1% Tween^{R}20 in 1X PBS. All steps were done on a shaker (200 rpm). The slices were washed three times in 1X PBS and were incubated in freshly prepared DAPI solution for 90 minutes in the dark. The slices were washed three times in 1X PBS and were mounted using mowiol or fluorpreserve™ reagent. Then the slides were stored at 4°C until further analysis.

4.5.4. Co-staining of alpha-tubulin and different membrane markers

Freshly vibratome sliced tissue sections (75 µm thick slices) were used to investigate the existence of different membrane markers during mitosis. The same protocol as described in section 4.5.1 was used. The slices were incubated with FITC-conjugated anti-alpha-tubulin (raised in mouse, 1:25) overnight at 4°C. After three washing steps, the slices were incubated overnight at 4°C with one of the following antibodies: 1) anti-msDPPIV/CD26 (raised in goat, 1:100); 2) anti-Mrp2 (raised in rabbit, 1:1000); 3) anti-Phospho-Ezrin (Thr567)/Radixin (Thr564)/Moesin (Thr558) (raised in rabbit, 1:250); 4) anti-msLDLR (raised in goat, 1:25), 5) anti-E-cadherin (raised in rabbit, 1:100) or 7) anti-claudin1 (raised in rabbit, 1:50). After this incubation, the slices were washed three times in 1X PBS and incubated with Cy3-conjugated anti-goat (raised in donkey, 1:100) or Cy3-conjugated anti-rabbit (raised in donkey, 1:100 dilution) as secondary antibodies overnight at 4°C. Both primary and secondary antibodies were diluted in 0.3% BSA/1% Tween^{R}20 in 1X PBS. All steps were done on a shaker (200 rpm). The slices were washed three times in 1X PBS and were incubated in freshly prepared DAPI solution for

90 minutes in the dark. The slices were washed three times in 1X PBS and were mounted using mowiol or fluorpreserve™ reagent. Then the slides were stored at 4°C until further analysis.

4.5.5. Co-staining of DPPIV/CD26 and Mrp2 or claudin1

Freshly vibratome sliced tissue sections (75 µm thick slices) were prepared to prove the immunoreactivity of DPPIV/CD26 antibody at the apical membranes of the hepatocyte. The same protocol described in section 4.5.1 was used. The slices were incubated overnight at 4˚C with anti-msDPPIV/CD26 (raised in goat, 1:100) and anti-Mrp2 (raised in rabbit, 1:1000) or anti-claudin1 (raised in rabbit, 1:50). After this, the slices were washed three times in 1X PBS and were incubated with Cy3-conjugated anti-goat (raised in donkey, 1:100) and Cy5-conjugated anti-rabbit (raised in donkey, 1:100) as secondary antibodies overnight at 4°C. Primary and secondary antibodies were diluted in 0.3% BSA/1% Tween^{R}20 in 1X PBS. All steps were done on a shaker (200 rpm). The slices were washed three times in 1X PBS and were incubated in freshly prepared DAPI solution for 90 minutes in the dark. The slices were washed three times in 1X PBS and were mounted using mowiol or fluorpreserve™ reagent. Then the slides were stored at 4°C until further analysis.

4.5.6. Co-staining of DPPIV/CD26, ICAM-1 and dylight 649 conjugated donkey anti-mouse (DMs)

To confirm that the dylight 649 conjugated donkey anti-mouse binds the hepatic sinusoidal endothelial cells, freshly vibratome sliced tissue sections (75 µm thick slices) were used. The same protocol as described in section 4.5.1 was used. The slices were incubated overnight at 4˚C with anti-msDPPIV/CD26 (raised in goat, 1:100) and anti-ICAM-1 (raised in rabbit, 1:100). After this incubation, the slices were washed three times in 1X PBS and were incubated with Cy2-conjugated anti-goat (raised in donkey, 1:100), Cy3-conjugated anti-rabbit (raised in donkey, 1:100) and dylight-649-conjugated

anti-mouse (raised in donkey, 1:750) as secondary antibodies overnight at 4°C. Primary and secondary antibodies were diluted in 0.3% BSA/1% Tween^{R}20 in 1X PBS. All steps were done on a shaker (200 rpm). The slices were washed three times in 1X PBS and were incubated in freshly prepared DAPI solution for 90 minutes in the dark. The slices were washed three times in 1X PBS and were mounted using mowiol or fluorpreserve™ reagent. Then the slides were stored at 4°C until further analysis.

4.5.7. Co-staining of DPPIV/CD26 and collagen III

Freshly vibratome sliced tissue sections (75 µm thick slices) were used to investigate the deposition of collagen and extracellular matrix during liver fibrosis. The slices were washed three times in 1X PBS. Freshly prepared citrate buffer was heated for 2 minutes in a microwave. Three ml of heated buffer were poured in a well of a 6 well plate and the slices were moved and incubated into the heated buffer for two minutes. During incubation, the buffer was heated for two minutes and the previous step was repeated ten times. Subsequently, the slices were cooled down to room temperature for ten minutes and washed three times in 1X PBS. Unspecific binding sites were blocked using 3% BSA/1% Tween^{R}20 in 1X PBS for two hours at room temperature, followed by incubation with anti-collagen III (raised in rabbit, 1:200) and anti-msDPPIV/CD26 (raised in goat, 1:100) overnight at 4°C. Subsequently, the slices were washed three times in 1X PBS and incubated with Cy3-conjugated anti-rabbit (raised in donkey, 1:100) and 488-conjugated anti-goat (raised in donkey, 1:100) as secondary antibodies overnight at 4°C. Primary and secondary antibodies were diluted in 0.3% BSA/1% Tween^{R}20 in 1X PBS. All steps were done on a shaker (200 rpm). The slices were washed three times in 1X PBS and were incubated in freshly prepared DAPI solution for 90 minutes in the dark. The slices were washed three times in 1X PBS and were mounted using mowiol or fluorpreserve™ reagent. Then the slides were stored at 4°C until further analysis.

4.6. Image analysis and microscopy:

4.6.1. Fluorescence and bright field microscopy:

All slides were screened shortly within one week after the staining procedure using fluorescence microscopy. The thorough analysis was performed within six weeks. For H&E, picro-sirius red, BrdU immunostaining, glutamine synthetase (GS) immunohistochemistry and α-SMA immunostaining, the slides were scanned and different regions of the liver tissue checked through the whole sections by a bright field microscope.

4.6.2. Confocal laser scanning microscopy and Z-stack preparation:

The vibratome slices stained with conjugated fluorescent dyes were analyzed using a confocal laser scanning microscope. Excitation and emission wavelengths were used as described by the manufacturer (Olympus). The ability of a confocal laser scanning microscope to generate a high-resolution in-focus image of thick liver tissues is one of the biggest advantages of this system. Approximately 75 µm deep vibratome slices of mouse liver have been immunostained using the antibody of interest. Subsequently, these slices were counterstained with DAPI to visualize the nuclei. Then, the Z-stacks were prepared as follows: 1) Adjustment of the signal intensity throughout the Z-direction: to focus into the specimen, the microscope focus was adjusted until the signal of interest was no longer visible in the live view window. The start set button was clicked on the confocal software to set the start position. Then, the microscope focus was moved away from the specimen until the signal of interest was no longer visible. The end set button was clicked on the confocal software to set the end. Laser parameters such as signal intensity, offset and amplification of the signal were adjusted manually; 2) Z-stack acquisition and recording: the start was in the lower position of the objective. The objective then automatically moved up each step (moving against gravity) until the end position was reached, and 3) Z-stack settings: for micro-architecture reconstruction and quantification, the 20x oil objective was used, the Z-step size was 0.54 µm and

speed was 0.4 ms (millisecond). The dataset consisted of 110 – 180 spatially consecutive images. Each image was 1024x1024 pixels in size and included four color channels that corresponded to the local intensity of the emitted fluorescent light by the costained specimen. The colours mapped as following: dylight 488-conjugated – green, Cy3 conjugated– white, dylight 649-conjugated– red and DAPI– blue. The different dyes were detected specifically without crosstalk between the channels. At least, nine Z-stacks per time point were generated and the acquired image stacks processed using imaris 3D-rendering software.

4.7. Quantification of the centrilobular necrosis

In order to quantify the centrilobular damage, screening of hematoxylin & Eosin stained sections was performed using a bright field microscope. Four representative images were acquired using a 4x objective. Subsequently, the total area of each image was recorded using Cell∧F software and the centrilobular necrosis area was measured as a cell mass without visible nuclei (Fig. 4.5A). The central vein lumen was considered healthy tissue. Then the percentage of centrilobular necrosis per image was calculated based on the following equation:

Centrilobular necrosis (%) = centrilobular necrosis (mm^2)/ Total area (mm^2) x 100

The presented data are mean values ±SE of three mice per time point.

4.8. Quantification of BrdU-positive hepatocytes

For BrdU positive hepatocyte quantification, screening of BrdU stained sections was done using a bright field microscope. Five representative images were acquired using the 20x objective. Subsequently, the total area of each image was captured using Cell∧F software and the number of BrdU positive nuclei quantified as brown nuclei (Fig. 4.5B) by image J software. Then the number of BrdU positive hepatocytes per image was calculated in square millimeter and presented as a percentage of the total number of hepatocytes. The presented data are mean values ±SE of three mice per time point.

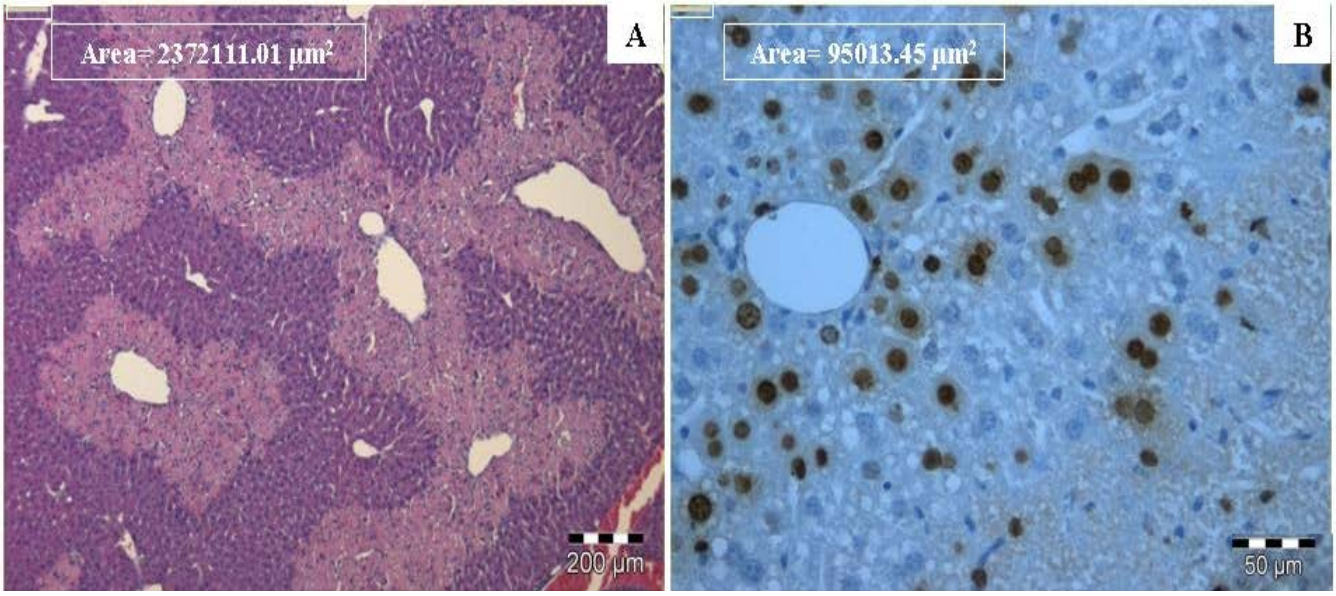

Figure 4.5. Hematoxylin & Eosin staining and BrdU immunohistochemistry of the paraffin embedded mouse livers. A) Hematoxylin & Eosin stained image for centrilobular necrosis quantification and the number showed the total area of the image. B) Quantification of the BrdU incorporated hepatocyte nuclei was performed using BrdU immunostained sections. The BrdU incorporated nuclei (S-phase) appeared brown. The number showed the total area of the image. Scale bars are 200 and 50 µm in A and B, respectively.

4.9. Quantification of alpha-smooth muscle actin (α-SMA) positive area

For quantification of the α-SMA positive area in fibrotic livers, α-SMA immunohistochemistry was used. The whole slide images were captured using an aperio image scanner and were processed by aperio imagescope software. Subsequently, positive pixel count v9 (Version 9.1) algorithm was used (pixel area /millimeter-squared) to quantify the α-SMA positive area. The presented data are mean values ±SE of 5 mice per time point.

4.10. Mathematical modelling

The mathematical modeling of liver intoxication and regeneration was carried out as described (Hoehme et al. 2007, Hoehme et al., 2010). The programming and generation

of simulations was conducted by Stefan Hoehme and Dirk Drasdo at the Interdisciplinary Center for Bioinformatics at the University of Leipzig.

4.11. Statistical analysis

The presented data are mean values ±SE (Standard Error) of three mice per time point. Statistical analysis of mouse body weight and liver/body weight ratio was carried out using Mann-Whitney U test (IBM SPSS statistics 20). Statistical difference of the alpha-SMA positive area in fibrotic livers was performed by T- test (IBM SPSS statistics 20). Graphic designation with asterix (*) refers to statistical significant differences between the control mice and the carbon tetrachloride-treated group.

5. Results

To provide the data of this work, the results are summarized in four sections:

5.1. Establishment of immunostaining protocols.

5.2. Characterization of liver intoxication, regeneration and fibrosis after carbon tetrachloride treatment.

5.3. Hepatocyte polarity during carbon tetrachloride-induced hepatotoxicity and regeneration.

5.4. Reconstruction of the bile canalicular network of the normal, intoxicated, regenerated and fibrotic livers.

5.1. Establishment of immunostaining protocols

Today, several optical microscopes are commercially available which can produce multi-channel images. A confocal microscope has two main advantages 1) production of high resolution images; and 2) generation of deep Z-stacks. The reliability and specificity of the signal of interest depends mainly on the staining protocol used. The main obstacles are the ability of both primary and secondary antibodies to penetrate the relatively deep liver sections.

5.1.1. DPPIV/CD26 antibody labels the bile canaliculi and the hepatic sinusoids

The dipeptidyl peptidase IV (DPPIV/CD26) antibody specificity was investigated using DPPIV-/- mice (kindly provided by Prof. Dr. Bruno Christ - Leipzig). Using the architectural staining protocol (section 4.5.1) wild type and DPPIV-/- mouse livers were immunostained with antibodies directed against DPPIV/CD26, glutamine synthetase and dylight 649-conjugated donkey anti-mouse (DMs). In this co-staining biliary and sinusoidal networks can be labeled as well as the centrilobular hepatocytes. Subsequently, the slices were counterstained with DAPI and were scanned using confocal laser scanning microscopy. Figure 5.1 (upper row) shows representative images of the DPPIV/CD26 immunoreactivity at the apical membranes of hepatocytes

as well as at the hepatic sinusoids (control). In contrast, the DPPIV/CD26 signal disappeared in the transgenic (DPPIV-/-) mice (Fig. 5.1, lower row). The sinusoidal signal of DPPIV/CD26 was confirmed by the co-localization with the DMs immunopositivity (Fig. 5.1). These results indicate that DPPIV/CD26 antibody specifically labels both the bile canaliculi and the hepatic sinusoid. Therefore, this immunostaining can be used to reconstruct the liver micro-architecture in deep slices.

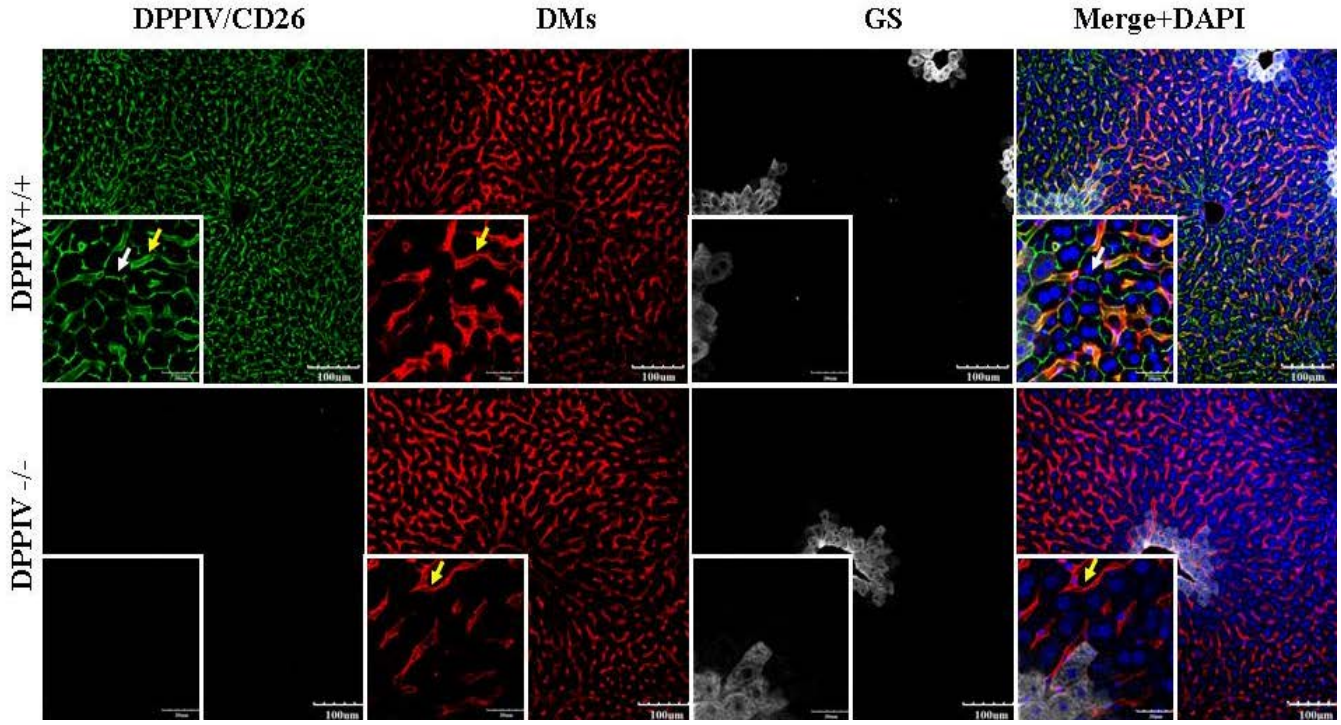

Figure 5.1. DPPIV/CD26 immunoreactivity at the bile canaliculi and the hepatic sinusoid. Liver sections from DPPIV wild type and knockout mice were co-stained as described in section 4.5.1. The DPPIV/CD26 antibody recognized the bile canaliculi (the apical surface of the hepatocytes- white arrows) and the hepatic sinusoids (yellow arrow) in wild type livers whereas it was completely negative in knockout livers. The scale bars are 100 and 30 μm in the low magnification and high magnification, respectively.

5.1.2. The bile canalicular signal of DPPIV/CD26 antibody co-localizes with Mrp2 and claudin1 signals

To confirm the specificity of the DPPIV/CD26 antibody for bile canaliculi, control livers were immunostained with antibodies directed against DPPIV/CD26 and Mrp2

(expressed specifically in the apical membrane of the hepatocyte and serves as biliary transporter, Fickert et al., 2001) or claudin1 (a component of the tight junction) as described in section 4.5.5). The DPPIV/CD26 immunoreactivity (Fig. 5.2, left) appeared at the bile canaliculi as well as at the hepatic sinusoids. While the Mrp2 (Fig. 5.2, middle upper) and claudin1 (Fig. 5.2, middle lower) was seen at the bile canaliculi only. The co-localization of DPPIV/CD26 and Mrp2 or claudin1 was shown in yellow at the bile canaliculi (apical membranes) of hepatocytes (Fig. 5.2, right). In conclusion the DPPIV/CD26 antibody labels specifically the bile canaliculi. Therefore, the alteration of the apical membrane of the hepatocyte during liver intoxication, regeneration and fibrosis can be investigated using the DPPIV/CD26 antibody.

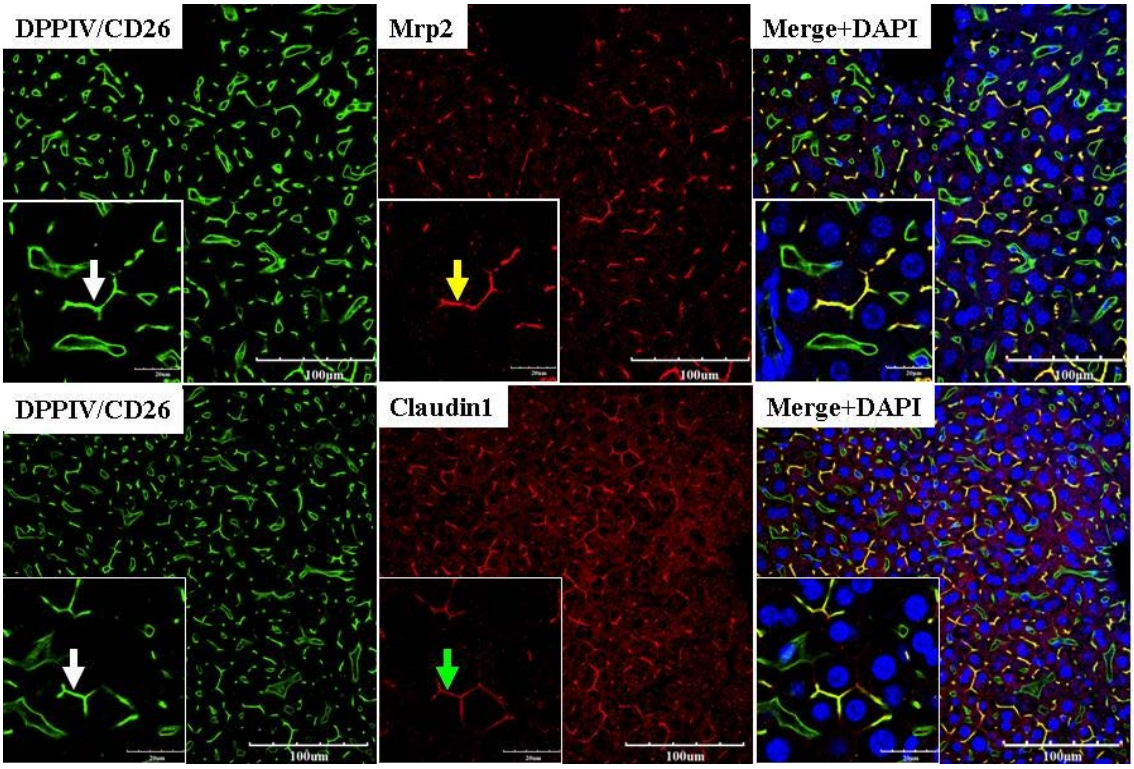

Figure 5.2. The bile canalicular signal of the DPPIV/CD26 antibody co-labeling with Mrp2 or claudin1. The DPPIV/CD26 antibody recognized the bile canaliculi between the hepatocytes (white arrow) and the hepatic sinusoids. The bile canaliculi are visualized by yellow fluorescence indicating co-localization of DPPIV/CD26 and Mrp2 (yellow arrow) or claudin1 (green arrow). The scale bars are 100 and 30 μm in the low magnification and high magnification, respectively.

5.1.3. Glutamine synthetase is a specific marker for the centrilobular hepatocytes

It is well known that glutamine synthetase (GS) is the β-catenin target at the centrilobular compartment of the hepatic lobule (Cadoret et al. 2002; Loeppen et al. 2002). Therefore, the specificity of the GS antibody was investigated using the β-catenin-/- mice (Braeuning et al., 2010) versus wild type mice.

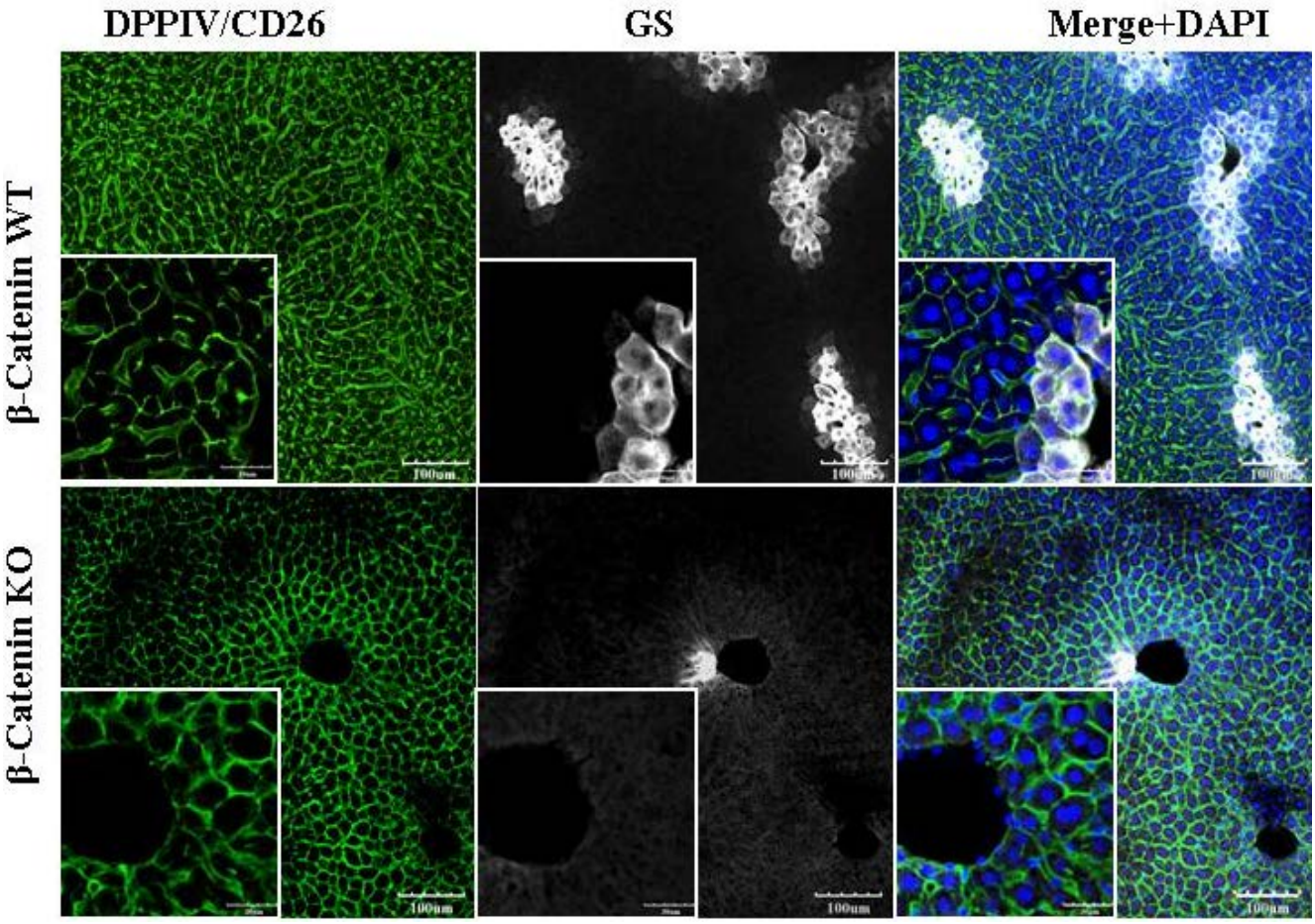

Figure 5.3. Glutamine synthetase signal reported at the centrilobular hepatocytes. Liver sections from β-catenin wild type and knockout were co-stained as described in section 4.5.1. The GS antibody was visualized in the cytoplasm of the centrilobular hepatocytes in wild type livers (upper) whereas it was negligible in the knockout samples (lower). The scale bars are 100 and 30 μm in the low magnification and high magnification, respectively.

Using the architectural staining protocol (section 4.5.1), control and β-catenin-/- livers were immunostained with antibodies directed against glutamine synthetase, DPPIV/CD26 and dylight 649-conjugated donkey anti-mouse (DMs). Figure 5.3 shows

representative images of the glutamine synthetase immunopositivity at the centrilobular hepatocytes in control livers. The GS signal disappeared in the transgenic (β-catenin-/-) mice (Fig. 5.3). A small fraction of hepatocytes escapes the cre-mediated gene knockout and these dispersed GS positive hepatocytes were characterized in Brauening et al., 2010. In conclusion, the glutamine synthetase antibody specifically labels the centrilobular hepatocytes. To analyze the spatial distribution of the hepatocytes during liver intoxication and regeneration, the exact position of the cell is a prerequisite. Therefore, this kind of GS immunoreactivity can be used to locate the central veins as a landmark for the hepatic lobule.

5.1.4. Dylight 649-conjugated donkey anti-mouse (DMs) localizes at the hepatic sinusoids

Due to the species compatibility of the glutamine synthetase (GS) and intercellular adhesion molecule-1 (ICAM-1) antibodies, we established a triple immunostaining technique using the dylight 649-conjugated donkey anti-mouse (DMs) instead of ICAM-1. The DMs labels the hepatic sinusoids un-specifically. To confirm if DMs generate identical signals as ICAM1, the co-staining of DMs, DPPIV/CD26 and ICAM-1 were performed in control livers using the staining protocol (section 4.5.6). In this co-staining, DPPIV/CD26 labeled both the bile canaliculi and hepatic sinusoidal networks, the hepatic sinusoids were visualized by both ICAM-1 and the DMs. Subsequently, the slices were counterstained with DAPI and were scanned using a confocal laser scanning microscope. The representative images of the immunoreactivity of the DMs at the hepatic sinusoids are shown in figure 5.4. This labeling was confirmed by co-localization of both ICAM-1 and DMs signals. Therefore, the DMs immunostaining can be used instead of ICAM-1 to reconstruct the liver microvasculature in deep slices.

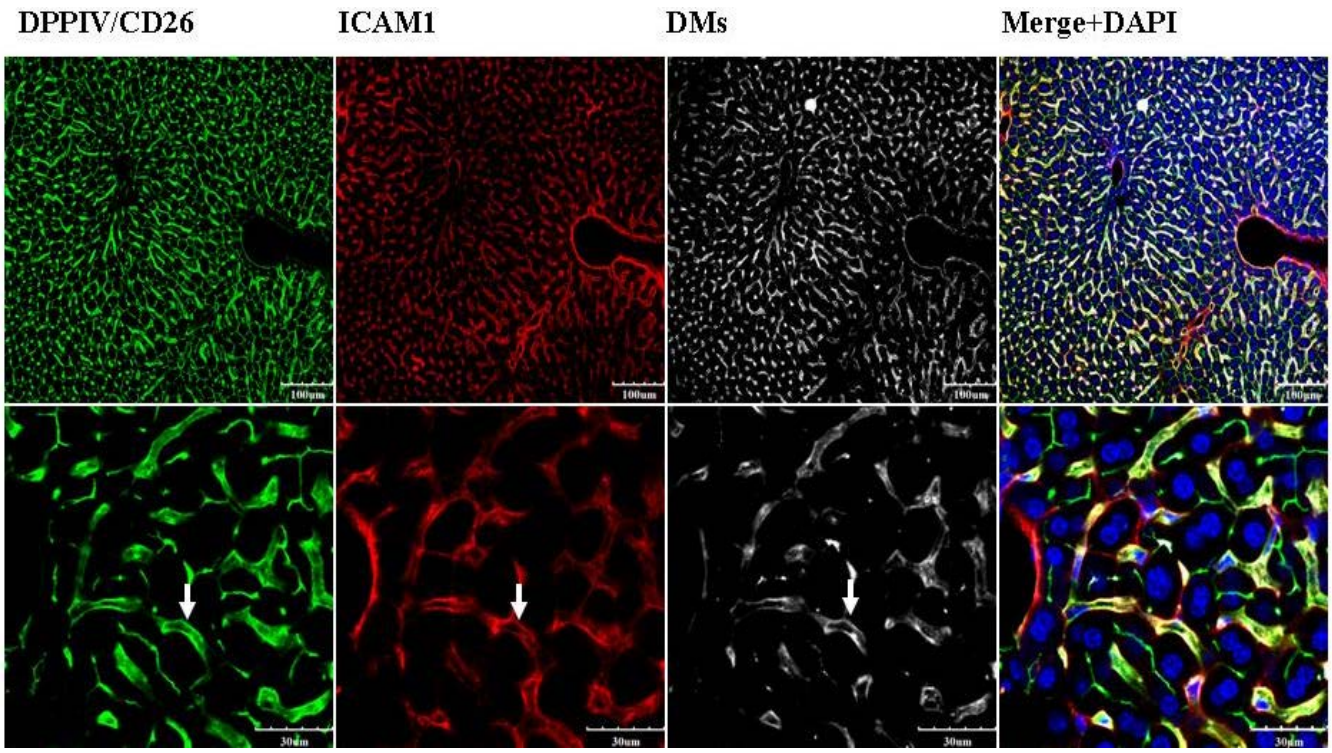

Figure 5.4. The dylight 649-conjugated donkey anti-mouse (DMs) signal visualized at the hepatic sinusoids. To confirm this finding, control livers were co-stained with antibodies directed against DPPIV/CD26 and ICAM-1 as described in section 4.5.6. The DMs secondary antibody was expressed at the hepatic sinusoids as well as ICAM-1 and DPPIV/CD26. The scale bars are 100 and 30 μm in the upper row and the lower row, respectively.

5.2. Characterization of liver intoxication and regeneration after CCl_4 injection

To investigate the acute hepatotoxicity of carbon tetrachloride as well as the regenerative capacity of mouse liver, male C57BL/6N mice were treated intraperitoneally with a single dose of 1.6 g/kg carbon tetrachloride (Fig. 4.1). Subsequently, mice received three doses of BrdU intraperitoneally 2, 4 and 6 hours before preparation of the livers. Three mice were analyzed for each of the time periods.

5.2.1. Mouse weight and liver weight (%)

The intraperitoneal administration of 1.6 g/kg carbon tetrachloride did not produce any mortality in treated mice.

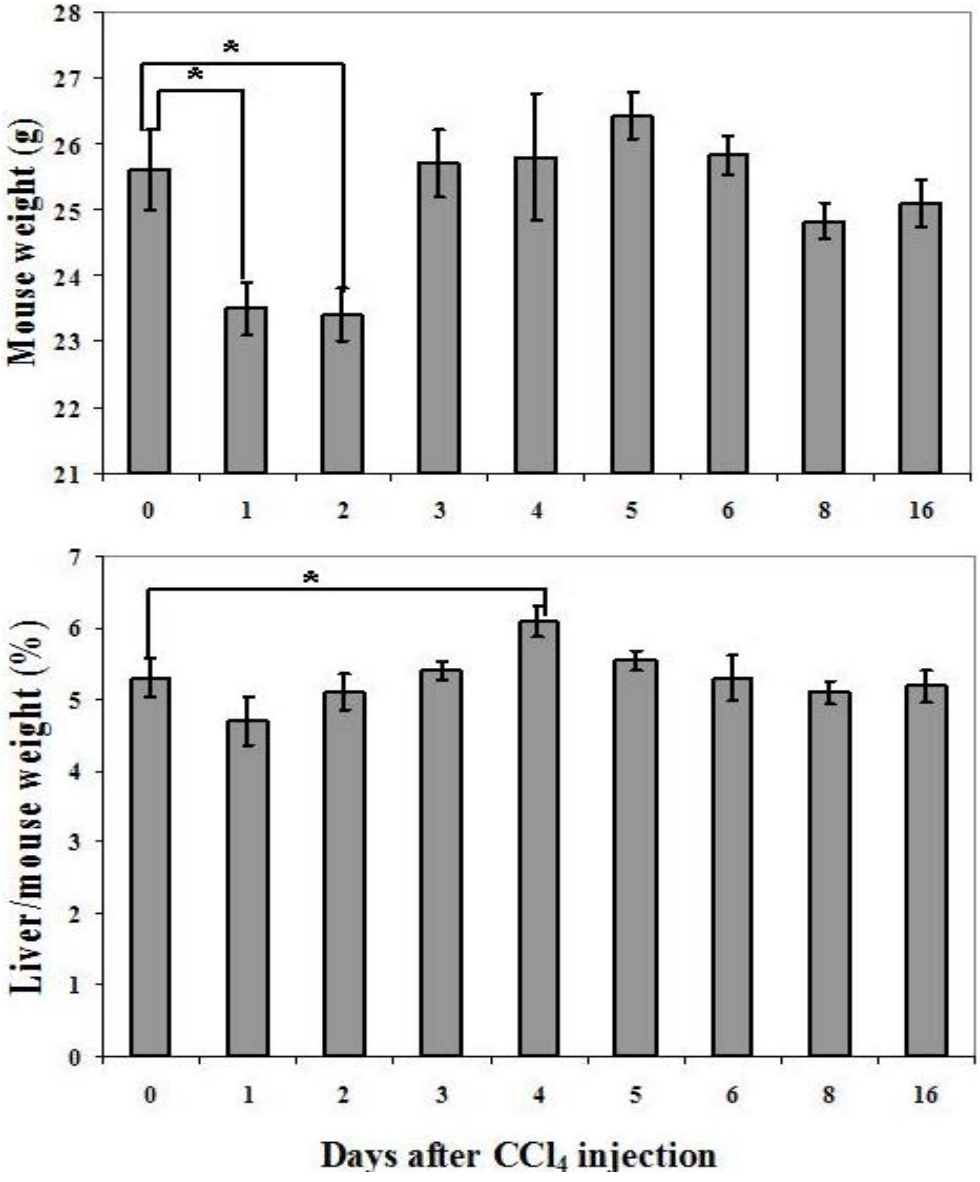

Figure 5.5. Mouse weight (g) and liver weight as a percentage of body weight at different time points after carbon tetrachloride injection. The data are mean values ±SE of 3 mice per time point. *P ≤ 0.05 compared to control.

It is well-known that the total body weight of an adult C57BL/6N mouse is nearly 25g and the liver weight is approximately 1.4 g and by percentage, liver represents about 4.5-5% of the total body weight (Koniaris, et al., 2003). During the first and second days after carbon tetrachloride intoxication, the mouse weight decreased significantly ($P \leq 0.05$). Then, it gradually recovered and reached its control level (Fig. 5.5). There were no significant differences ($P \leq 0.05$) in the percentage of the liver/mouse weight ratios in the treated mice in comparison with controls, the only statistical difference recorded at day four after intoxication during the massive regeneration process (Fig. 5.5).

5.2.2. Analysis of the centrilobular necrosis

5.2.2.1. Macroscopical analysis

The carbon tetrachloride treated mice and controls were photographically documented (Fig. 5.6). Livers of the treated mice showed a characteristic pattern of small white spots, because carbon tetrachloride caused toxicity in only a fraction of hepatocytes in the center of the liver lobules (centrilobular necrosis). These spots appeared and could be macroscopically recognized at day one, became more distinct one day later and almost disappeared 96 hours after carbon tetrachloride administration. At later time points after treatment, livers were undistinguishable from the control livers. Thus, a maximum macroscopic damage to the liver occurs between 24 hours and 48 hours after carbon tetrachloride administration.

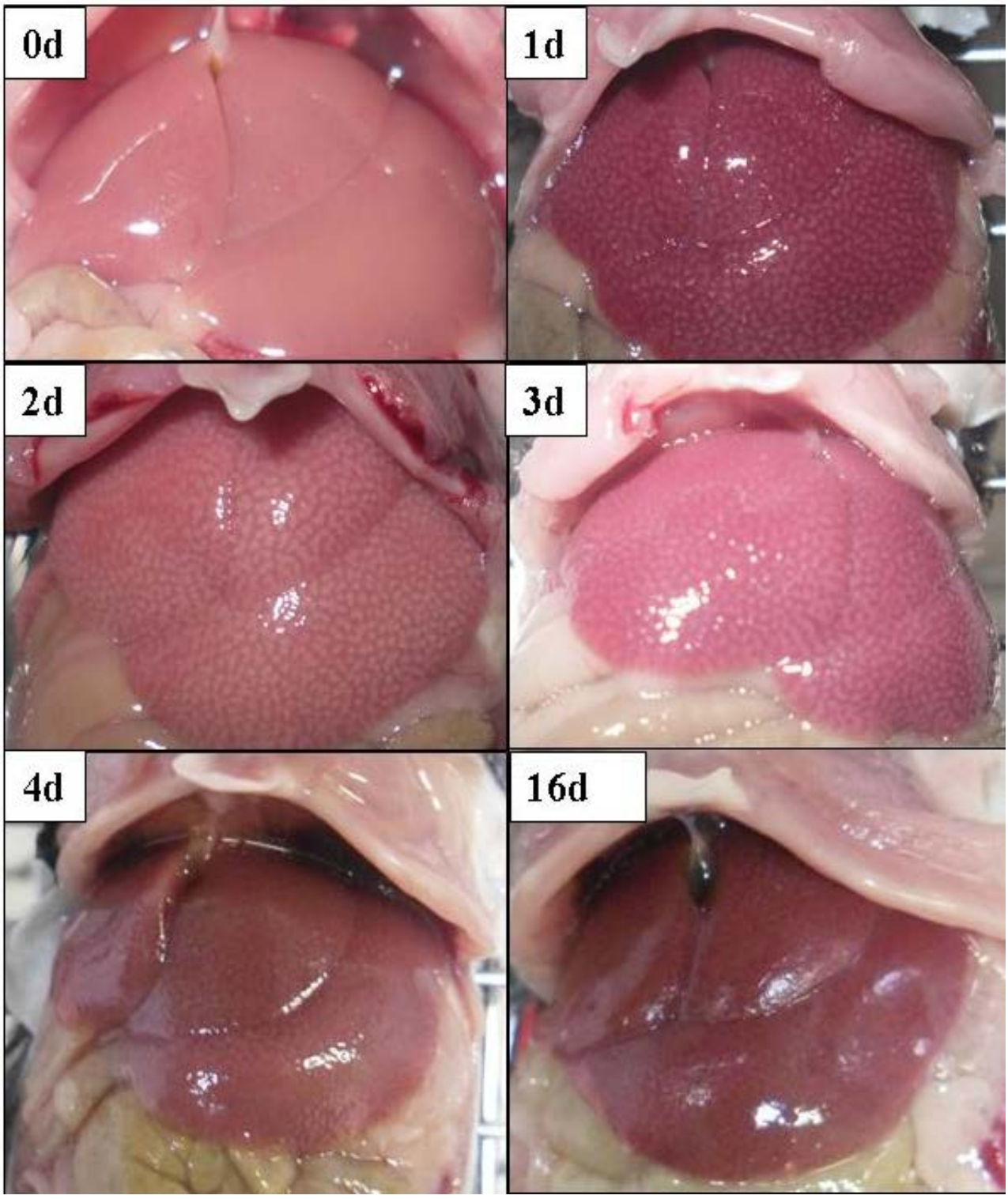

Figure 5.6. Macroscopical appearance of mouse livers at different time points after administration of 1.6 g/kg carbon tetrachloride. The livers showed a characteristic pattern of small white spots. These spots appeared between 24 and 72 hours after carbon tetrachloride intoxication and correspond to the centrilobular necrosis.

5.2.2.2. Microscopical analysis

To quantify the centrilobular necrosis, the paraffin sections were stained with hematoxylin and eosin (section 4.4.1) and images were captured by a light microscope.

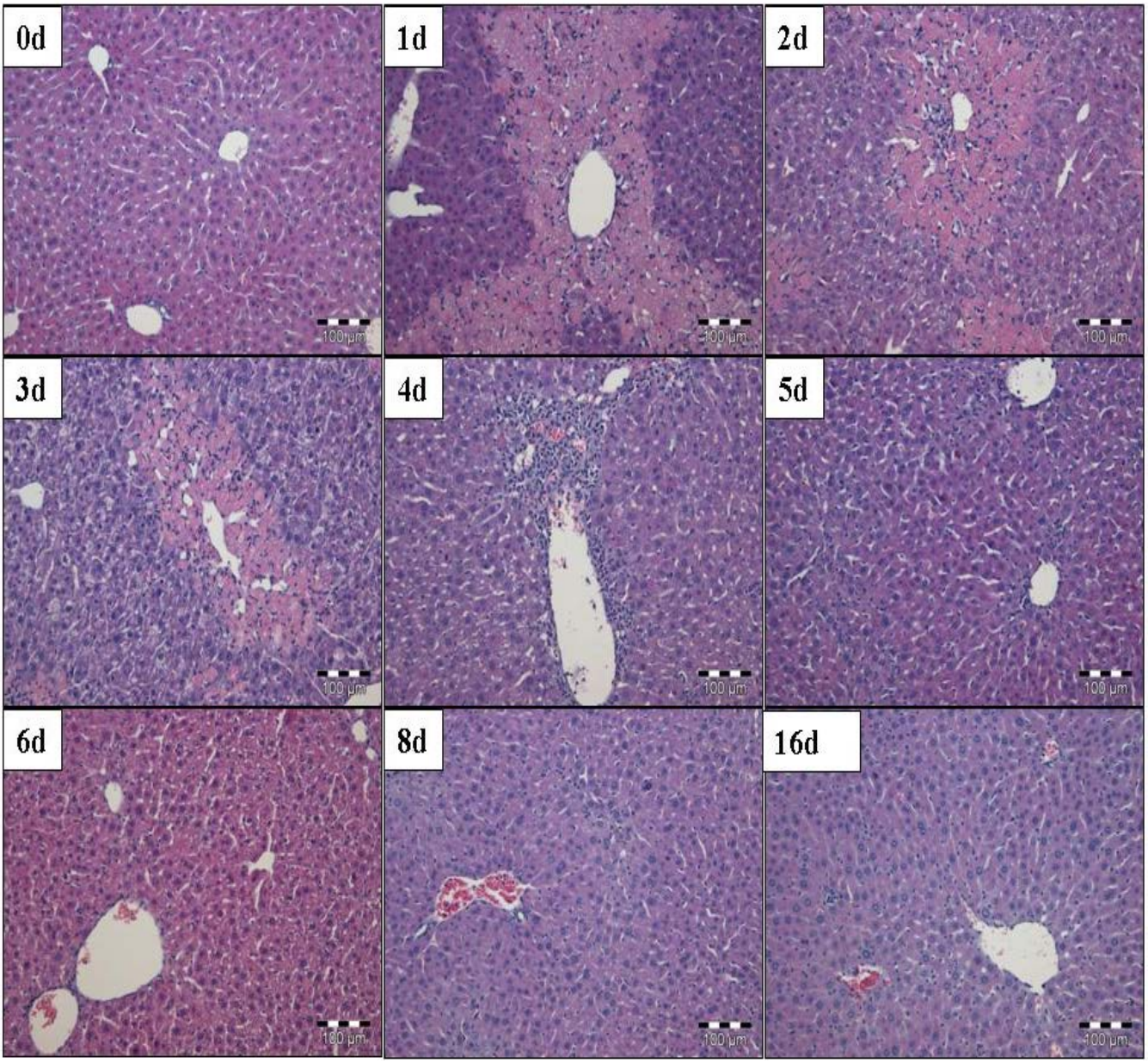

Figure 5.7. Microscopical appearance by hematoxylin and eosin (H&E) staining of mouse livers intoxication. The maximal necrosis of the centrilobular hepatocytes appeared at day one and two after carbon tetrachloride intoxication and gradually regenerated in the later time points. The scale bars are 100 μm.

Image analysis and quantification was performed by Cell^F software. The centrilobular necrosis was first seen at day one after carbon tetrachloride administration, with later infiltration of macrophages observed on day four after treatment (Fig. 5.7). Quantification of the dead cell area indicated that the maximum damage of the centrilobular areas occurred at day one and two after treatment (Fig. 5.8 and Table 5.1) which was in agreement with the liver marcoscopical pathology. The dead cell area was eventually closed by regenerating hepatocytes, and on day 6, it became histologically difficult to differentiate between treated and untreated livers

Table 5.1. Quantification of the necrotic area after carbon tetrachloride intoxication. The data are mean values ±SE of three mice per time point. The total area analyzed for necrosis was 2.37 mm^2 per image.

Days after CCl_4 injection	**Necrotic area / mm^2**	**Necrotic area [%]±SE**
0	0	0.00±0.00
1	1.17±0.67	49.36±1.63
2	1.28±0.99	53.99±2.18
3	0.82±0.57	34.59±1.49
4	0.51±0.35	21.51±0.86
5	0.27±0.09	11.37±2.04
6	0.04±0.03	1.68±1.30
8	0	0.00±0.00
16	0	0.00±0.00

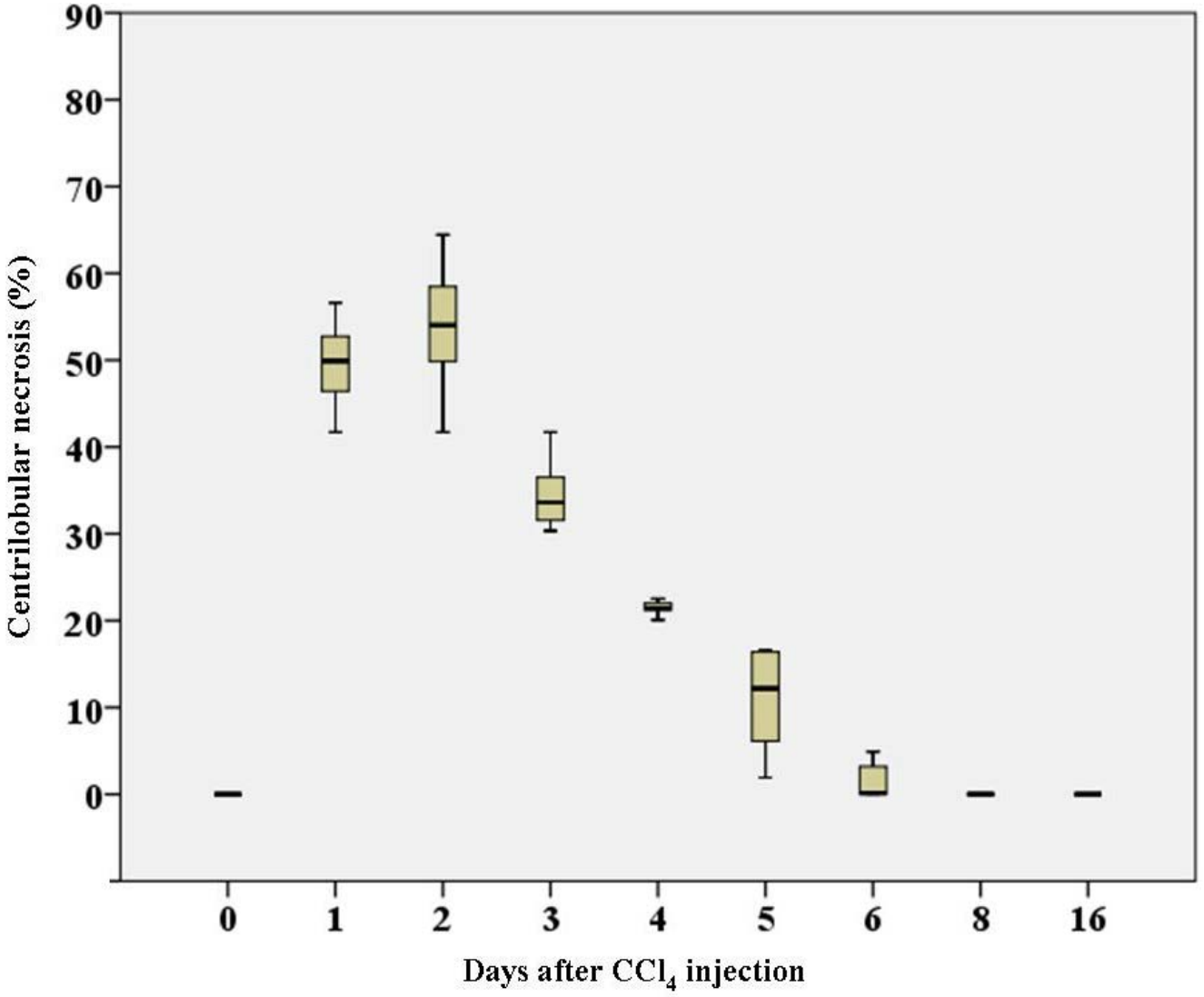

Figure 5.8. Quantification of the centrilobular necrosis in hematoxylin and eosin (H&E) stained liver sections. The data are mean values ±SE of three mice per time point.

5.2.2.3. Confirmation of the centrilobular carbon tetrachloride-induced necrosis by fluorescence microscopy

To confirm the centrilobular necrosis of carbon tetrachloride, 75 µm deep slices were prepared from the liver of control and carbon tetrachloride treated mice. The slices were stained to visualize bile canaliculi, hepatocytes around central veins, and the sinusoidal network. For this purpose, antibodies directed against DPPIV/CD26, glutamine synthetase and dylight 649-conjugated donkey anti-mouse (DMs) was used (section 4.5.1). Subsequently, the slices were counterstained with DAPI and were scanned using

a confocal laser microscope (Fig. 5.9). The dead cell area two days after carbon tetrachloride administration could also be seen in immunostained slices, appearing around the central veins as red background fluorescence. No hepatocyte nuclei were seen in the central dead cell area.

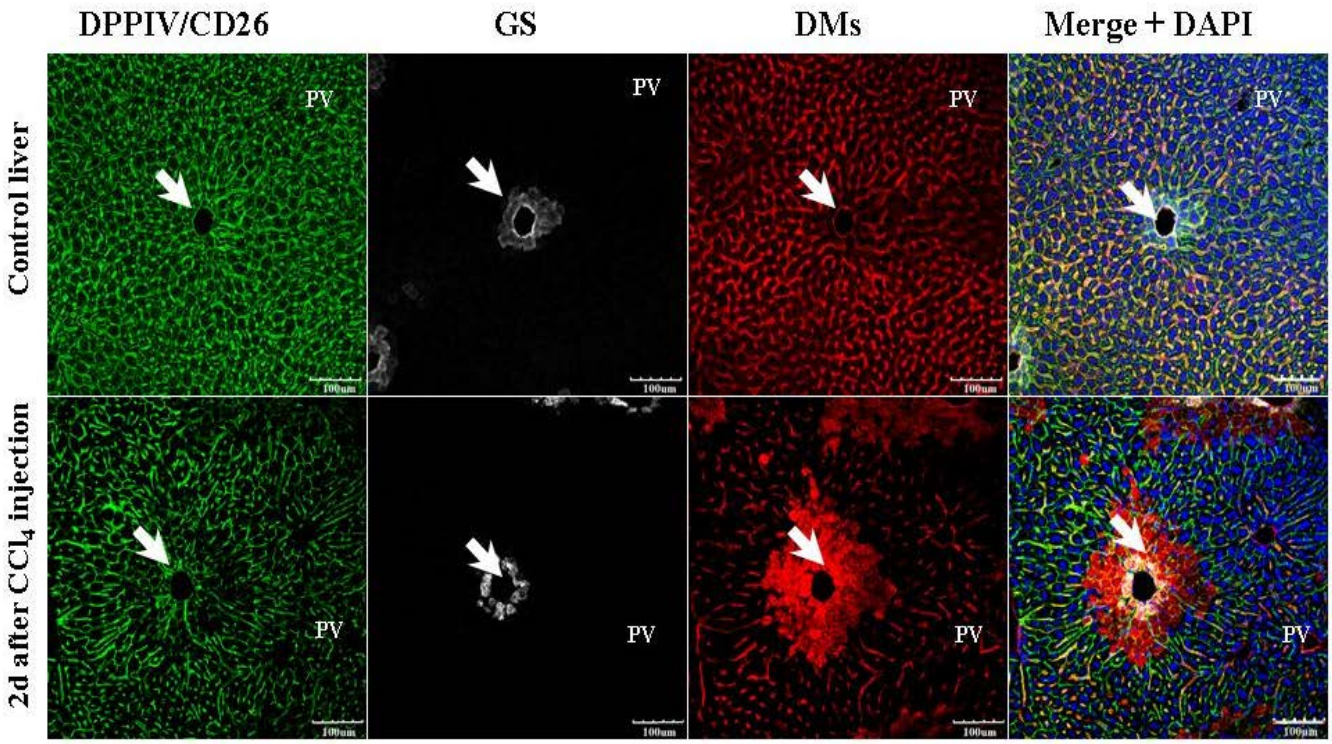

Figure 5.9. Microscopical appearance of control mouse liver and two days after carbon tetrachloride-intoxication using confocal laser scanning microscopy of immunostained slices. White arrows show the intact centrilobular hepatocytes in control liver (upper row) and damaged centrilobular hepatocytes (lower row). The scale bars are 100 µm.

5.2.3. Hepatocyte proliferation

5.2.3.1. Quantification of BrdU incorporation

To quantify the hepatocytes in S-phase, the mice were exposed to 1.6 g/kg carbon tetrachloride intraperitoneally and untreated mouse livers were used as a control tissue. All mice received three intraperitoneal doses of BrdU 2, 4 and 6 hours before liver preparation. Paraffin sections were stained with antibodies directed against BrdU (section 4.4.3) and images were captured using a light microscope (Fig. 5.10). Image

analysis and quantification was performed using Image J software. The percentage of BrdU positive hepatocytes was 0.54±0.02 in control livers, increasing to 32.59±2.21 two days after carbon tetrachloride administration (Fig. 5.10, Fig. 5.11 and Table 5.2). Subsequently, the fraction of BrdU positive nuclei decreased whereby, the values returned to control levels after six to eight days.

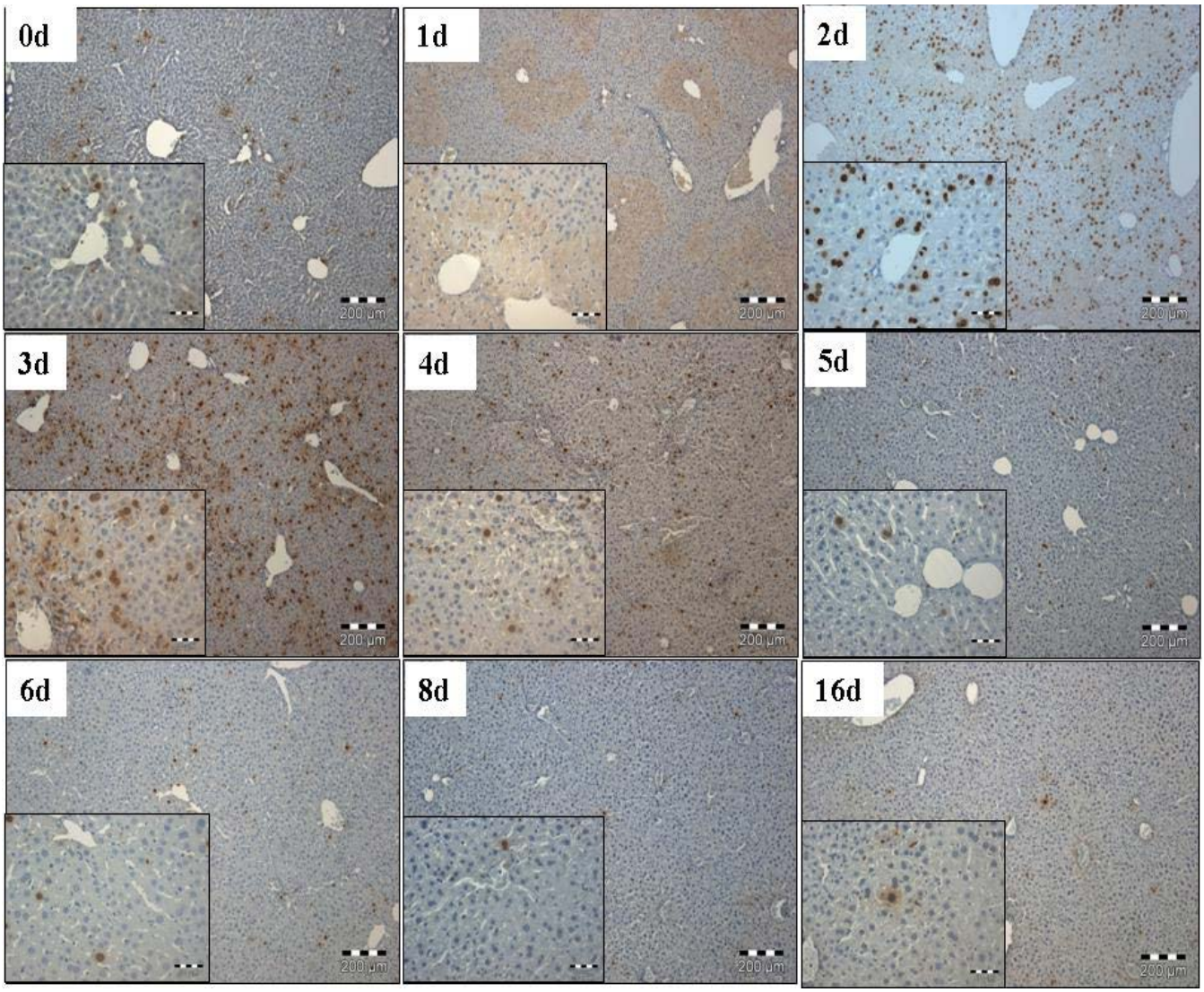

Figure 5.10. Proliferation status of hepatocytes was investigated by BrdU immunostaining of control and carbon tetrachloride-intoxicated mouse livers. All mice received three doses of BrdU 2, 4 and 6 hours before liver preparation. BrdU-positive nuclei appeared brown while negative nuclei are blue. The scale bars are 200 and 50 μm in the low magnification and high magnification, respectively.

Table 5.2. Number of BrdU-positive hepatocytes after intoxication with carbon tetrachloride. The data are mean values ±SE of three mice per time point.

Days after CCl_4 injection	BrdU positive nuclei per mm^2±SE	BrdU negative nuclei per mm^2±SE	Total nuclei per mm^2±SE	BrdU positive nuclei [%]±SE
0	9.82±0.15	1793±8.18	1803±33.87	0.54±0.88
1	3.51±0.12	1060±4.01	1063±31.99	0.33±0.67
2	334.1±1.87	691.9±3.19	1025±11.47	32.59±7.54
3	267.4±2.76	774.7±3.81	1042±27.09	25.65±11.86
4	222.5±1.79	970.5±3.24	1192±18.51	18.65±11.99
5	93.33±0.74	1607±4.58	1700±18.19	5.49±8.69
6	17.54±0.21	1762±8.65	1779±55.29	0.99±1.45
8	11.93±0.19	1784±7.32	1796±46.30	0.66±1.76
16	13.33±0.20	1764±7.30	1778±46.67	0.75±1.33

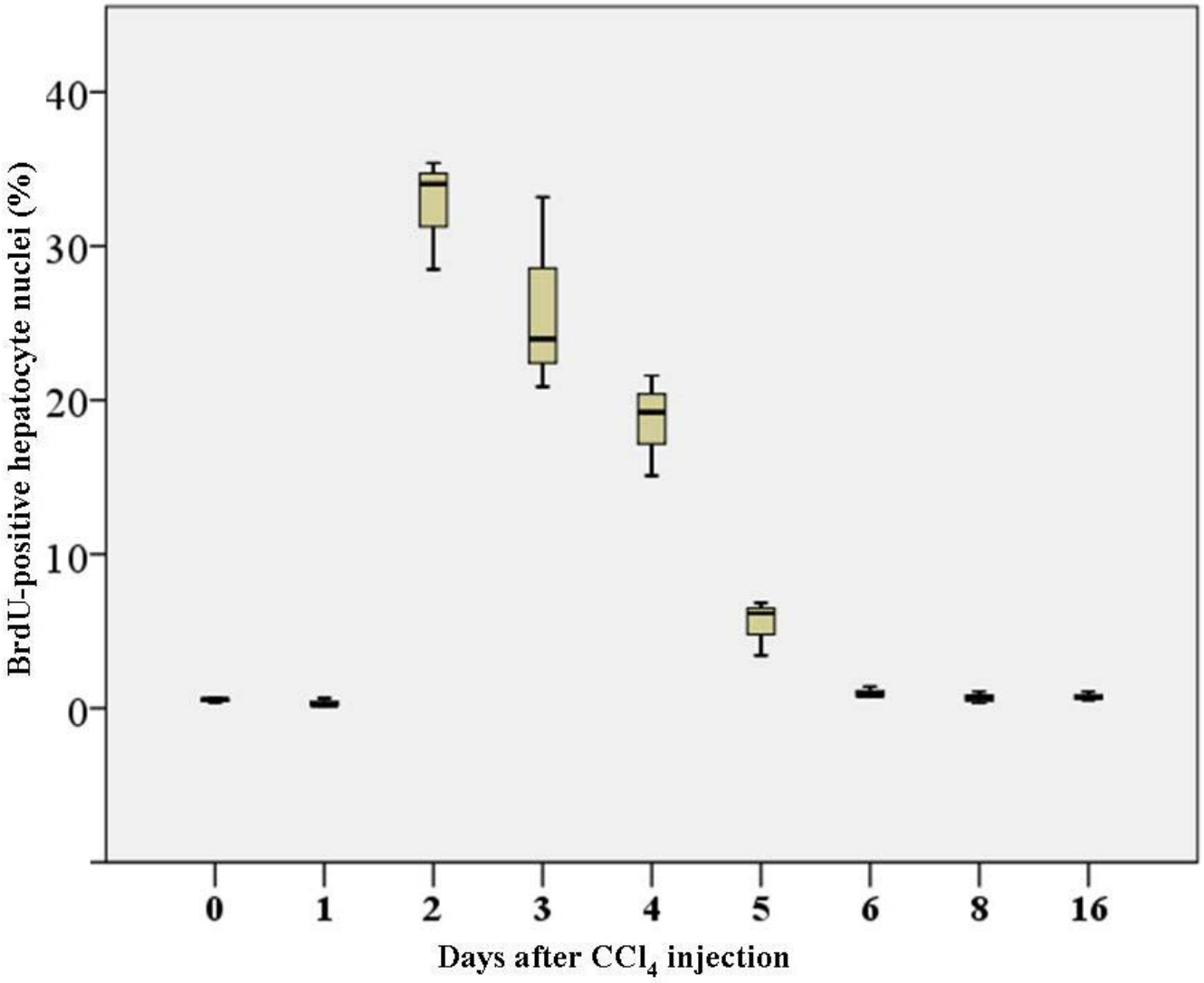

Figure 5.11. Quantification of the BrdU-positive hepatocytes in control and intoxicated livers. It was investigated by BrdU immunohistochemistry of mouse livers at different time points after carbon tetrachloride administration. Untreated mouse livers were used as controls. All mice received three doses of BrdU 2, 4 and 6 hours before liver preparation. The data are mean values ±SE of three mice per time point.

5.2.4. Total hepatocyte nuclei number per square millimeter

The total number of hepatocyte nuclei was quantified using paraffin sections. These sections were stained with antibodies directed against BrdU and images were captured using a light microscope (Fig. 5.12). Image analysis and quantification was performed using Image J software. The number of hepatocyte nuclei in square millimeter (mm^2)

was 1803±33.87 in control livers, decreasing to 1063±31.99 and 1025±11.47 at day one and day two after carbon tetrachloride administration, respectively (Fig. 5.12 and Table 5.2). Subsequently, the values returned to control levels after six to eight days.

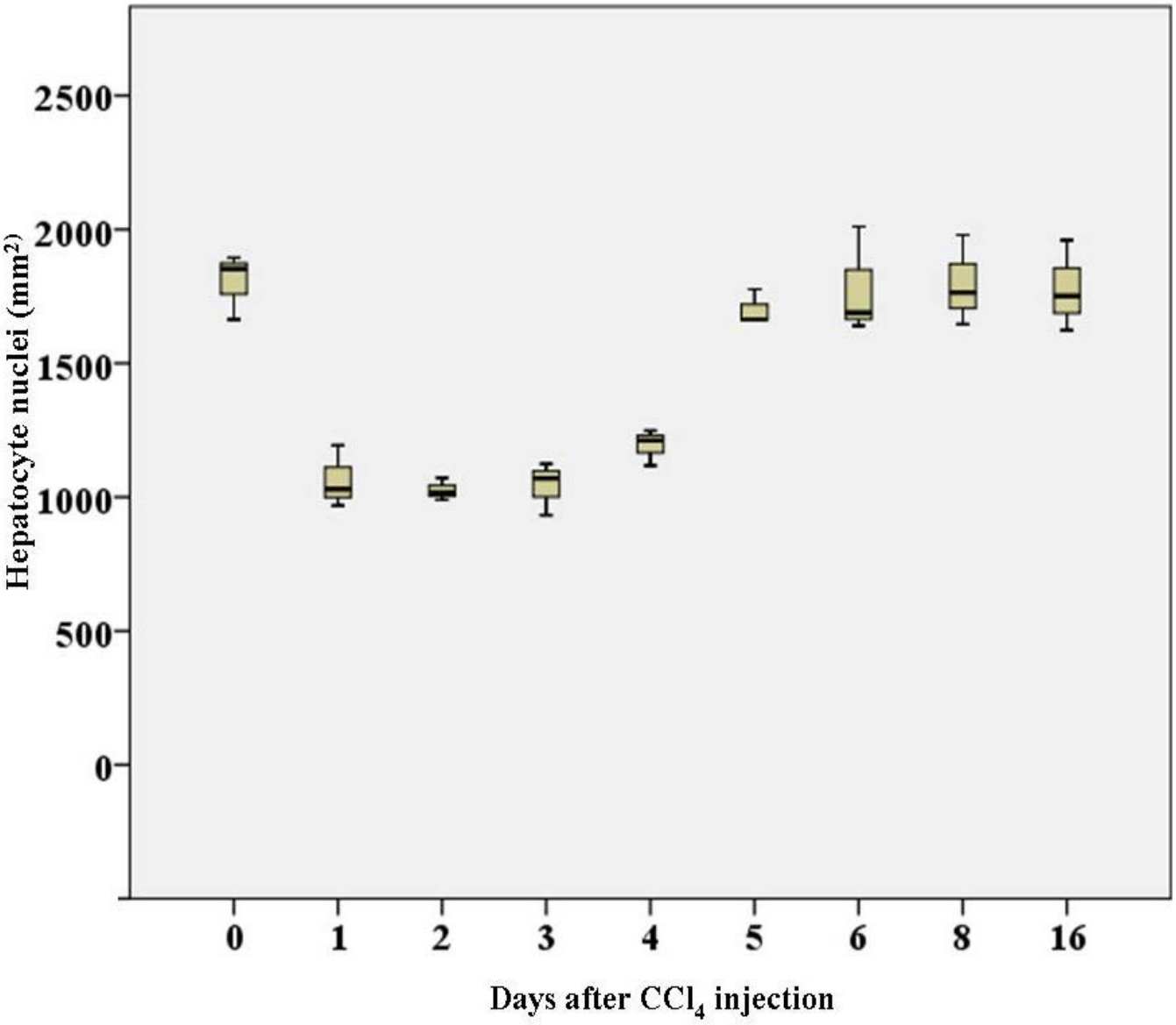

Figure 5.12. The total number of hepatocyte nuclei per mm^2 was investigated by BrdU immunostaining of mouse livers at different time points after intoxication. Untreated mouse livers were used as controls. All mice received three doses of BrdU 2, 4 and 6 hours before liver preparation. The data are mean values ±SE of three mice per time point.

5.2.5. Simulation of the destruction and regeneration processes after carbon tetrachloride by a mathematical model

Recently, a technique of spatial-temporal modelling has been established that allows the simulation of tissue intoxication and regeneration as well as the involved architectural alterations (Hoehme et al., 2010). After carbon tetrachloride intoxication similar processes occur in almost all hepatic lobules, therefore, we modeled only a single lobule according to (Matsumoto and Kawakami, 1982) used this model (Hoehme et al., 2010) and included the experimentally determined parameters from sections 5.2.2.2, 5.2.3 and 5.2.4. The model can be visualized as a movie. Stills from this movie are shown in figure 5.13 illustrating the centrilobular necrosis followed by proliferation of some of the surviving hepatocytes. Later the dead cell area becomes smaller in agreement to the experimental data (Fig. 5.8, Fig. 5.11, Fig. 5.12, Table 5.1 and Table 5.2). It is no longer visible after six days. The entire movie can be seen on the following website: http//www.ifado.de.

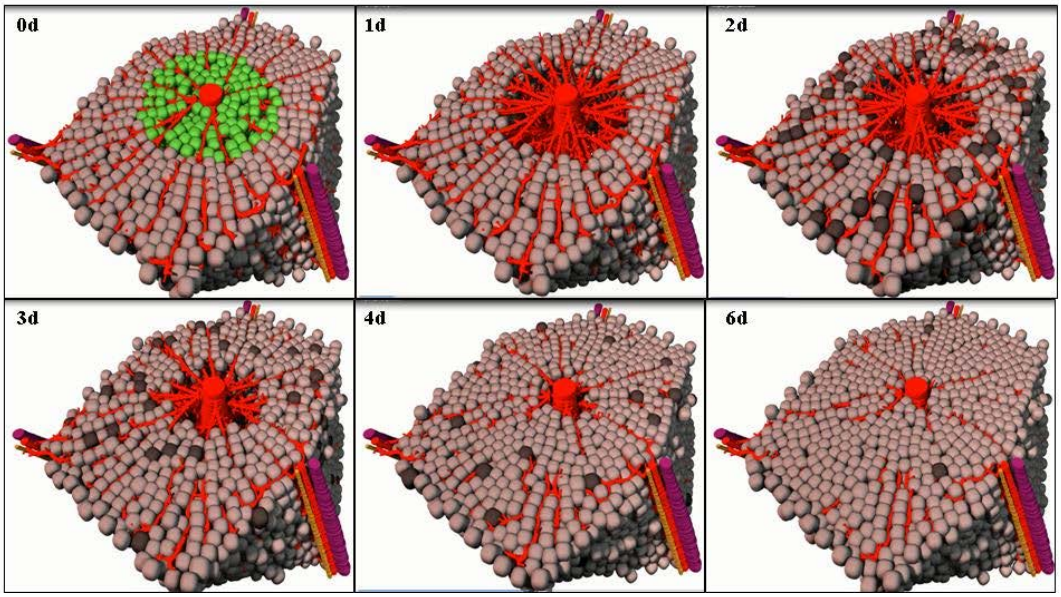

Figure 5.13. Mathematical modelling of liver intoxication and regeneration. The model consisted of one hepatic lobule. It contained central vein and hepatic artery (red), portal vein (violet) and the bile duct (yellow). The centrilobular hepatocytes appeared green, the periportal ones visualized as a grey and the proliferating hepatocytes seen as black. Stills of a movie showing the centrilobular necrosis followed by proliferation of some of the surviving hepatocytes. Later the necrotic area becomes smaller in agreement to the experimental data. The movie can be seen on http//www.ifado.de. (Source: Hoehme et al., 2010)

5.2.6. Characterization of liver fibrosis induced by repetitive carbon tetrachloride injections

To investigate the impact of repetitive doses of carbon tetrachloride on the liver, male C57BL/6J mice were treated by repeated intraperitoneal carbon tetrachloride three times a week (1.6 g /kg body weight in olive oil) during six weeks (section 4.1.4). A control group received olive oil only. Mice were sacrificed 48 hours after the last carbon tetrachloride injection. Five mice were used for each of the time point. To investigate the progression of liver fibrosis, the paraffin sections were stained with hematoxylin and eosin (sections 4.4.1) and picro-sirius red (sections 4.4.2). The images were captured by a light microscope. In the control livers, the normal hepatic architecture and lobulation were preserved as well as a normal distribution of collagen around the big blood vessels (Fig. 5.14, H&E and picro-sirius red). In carbon tetrachloride-treated liver tissue, the centrilobular necrosis became distinct, massive infiltrates appeared around the central vein and the extracellular matrix (ECM) and collagen was deposited and bridged between the central veins (Chobert et al., 2012) forming a pseudolobulation (Fig. 5.14, H&E and picro-sirius red). The expression of alpha-smooth muscle actin (α-SMA)- as a marker of ECM and collagen producing cells- was done by immunohistochemistry in the paraffin sections (section 4.4.5). The images were taken by a light microscope. The α-SMA positive cells were observed in the vicinity of the centrilobular area of the hepatic lobule in fibrotic livers (Fig. 5.14, α-SMA). These cells are mostly activated hepatic stellate cells (HSCs) and myofibroblasts. The quantification of α-SMA positive area revealed a significant difference between control and carbon tetrachloride -treated groups. They are producing collagen which is deposited around the central veins. Furthermore, the liver micro-architecture distributions were investigated using the architectural staining (section 4.5.1). In the control group, the liver lobule showed a normal distribution of the centrilobular hepatocytes, while in fibrotic livers the infiltrations filled the central part of the hepatic lobule (Fig. 5.15, upper row). The deposition of collagen was confirmed by collagen III immunofluorescence staining

(section 4.5.7). Under normal conditions, collagen was seen at the blood vessels only and after chronic treatment with carbon tetrachloride the collagen was deposited at the centrilobular area and extended between the neighboring veins. This deposition is correlated with picro-sirius red positive area and alpha-SMA immunohistochemistry findings.

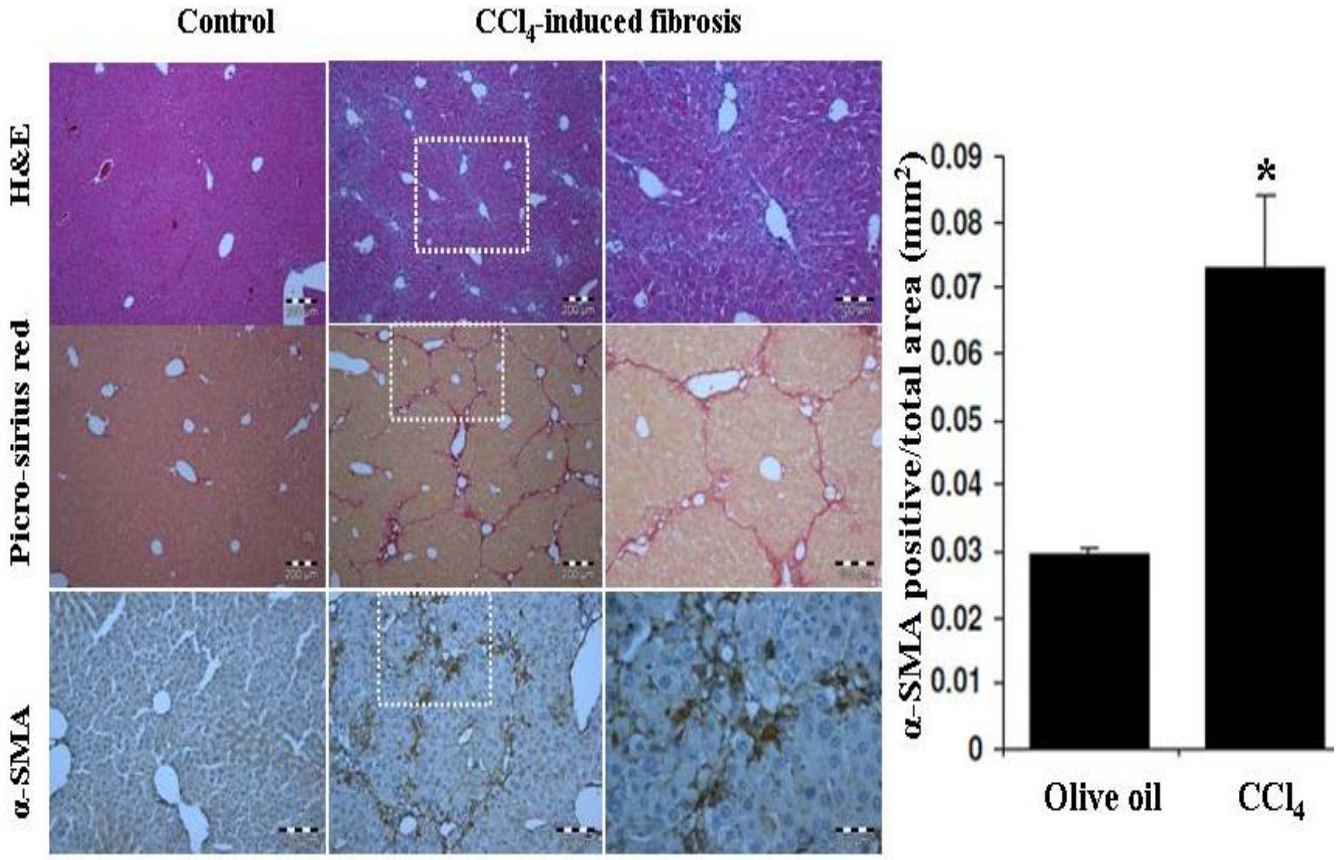

Figure 5.14. Histopathological examination of mouse livers by H&E, picro-sirius red and alpha-smooth muscle actin (α-SMA) staining. Mice receiving olive oil revealed normal hepatic architecture (H&E staining, scale bar is 200 µm) and a normal collagen distribution (picro-sirius red staining, scale bar is 200 µm) also α-SMA immuno-localized at the smooth musculature (α-SMA immunohistochemistry, scale bar is 100 µm). Liver tissue from 6 weeks carbon tetrachloride-treated group showed extensive infiltrations (H&E staining, scale bar is 200 µm and 100 µm), collagen deposition and bridging fibrosis (picro-sirius red staining, scale bar is 200 µm and 100 µm) as well as many α-SMA-positive myofibroblasts (α-SMA immunohistochemistry, scale bar is 100 µm and 50 µm) were detected and the hepatic micro-architecture were disrupted.

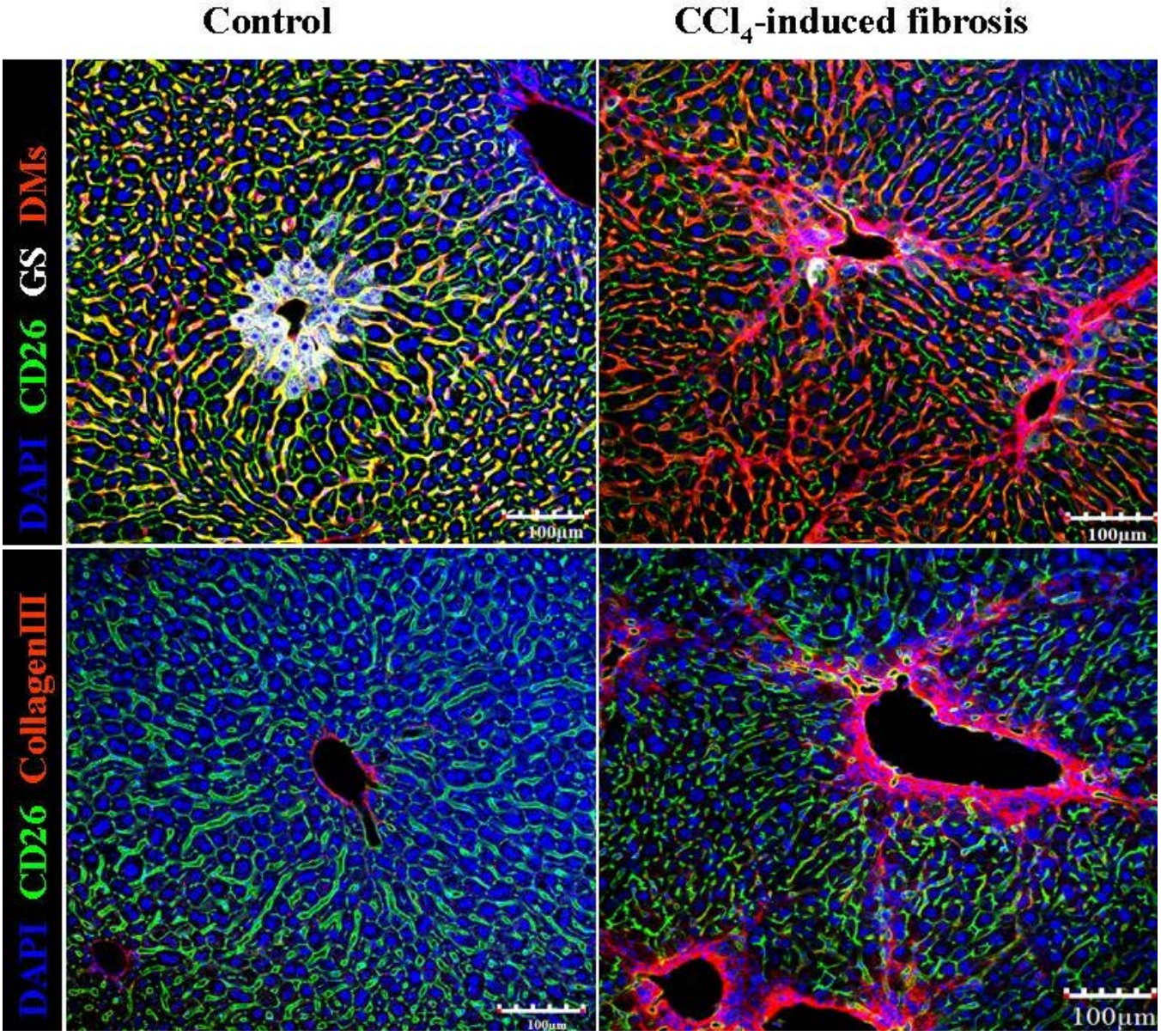

Figure 5.15. The liver micro-architecture and collagen deposition were analyzed using immunofluorescence staining of deep liver slices. The upper row images showed the normal architecture (left) of the control mice, while in the carbon tetrachloride-treated livers the infiltration of macrophages between the compromised centrilobular hepatocytes (right) was predominant. The deposition of ECM and collagen were confirmed by collagen III immunostaining (lower row). Under physiological conditions, the collagen localized at the blood vessels (left). However, in the fibrotic livers, the collagen reactivity appeared at the centrilobular compartment of the hepatic lobule and extended to connect the neighboring veins (right) as evidenced by picro-sirius red staining. Scale bars are 100 µm.

5.3. Hepatocyte polarity during carbon tetrachloride-induced hepatotoxicity and regeneration

There are several basolateral and apical poles per hepatocyte and the maintenance of hepatocyte polarity is of major importance for liver physiology. Asymmetric distribution of the protein and lipid content of hepatocyte membranes reflects the different functions of both poles, which in turn controls the balance between architecture stability and plasticity. To test whether hepatocytes transiently loose (Lecuit and Lenne, 2007) or maintain their polarity during liver regeneration, male C57BL/6N mice were treated intraperitoneally with a single dose of carbon tetrachloride (1.6 g/kg). To study the hepatocyte membranes during the S-phase of the cell cycle, the mice received three doses of BrdU intraperitoneally 2, 4 and 6 hours before preparation of the livers (Fig. 4.1). Three mice were analyzed for each of the time points. Liver sections were costained with antibodies directed against BrdU (S-phase hepatocyte) or alpha-tubulin (to visualize mitotic spindle) and different apical, tight junction and basolateral markers (section 4.5.3 and section 4.5.4). Liver sections from both control and carbon tetrachloride-treated (two days) mice were scanned using a confocal microscope and Z-stacks were prepared. The acquired image stacks were processed using Imaris 3D-rendering software.

5.3.1. The apical domains of hepatocytes are maintained during both S- and M-phases

There are several transporters that control biliary function and these transporters need to be correctly established at the apical pole. The apical poles of hepatocytes were visualized using the following antibodies 1) Dipeptidyl peptidase-4 (DPPIV/CD26) - a cell surface ectopeptidase that is expressed mainly on the bile canaliculi (Hong et al., 1989) and to lesser extent on hepatic sinusoidal endothelial cells; 2) Multidrug resistance protein 2 (Mrp2) - a canalicular organic anion transporter, which is therefore expressed specifically at the bile canaliculi (Fickert et al., 2001); and 3) phospho-Ezrin

(Thr567)/Radixin (Thr564)/ Moesin (Thr558) that detects ezrin, radixin and moesin (ERM family). The ERM family of proteins serves as linker between the plasma membrane and the actin cytoskeleton.

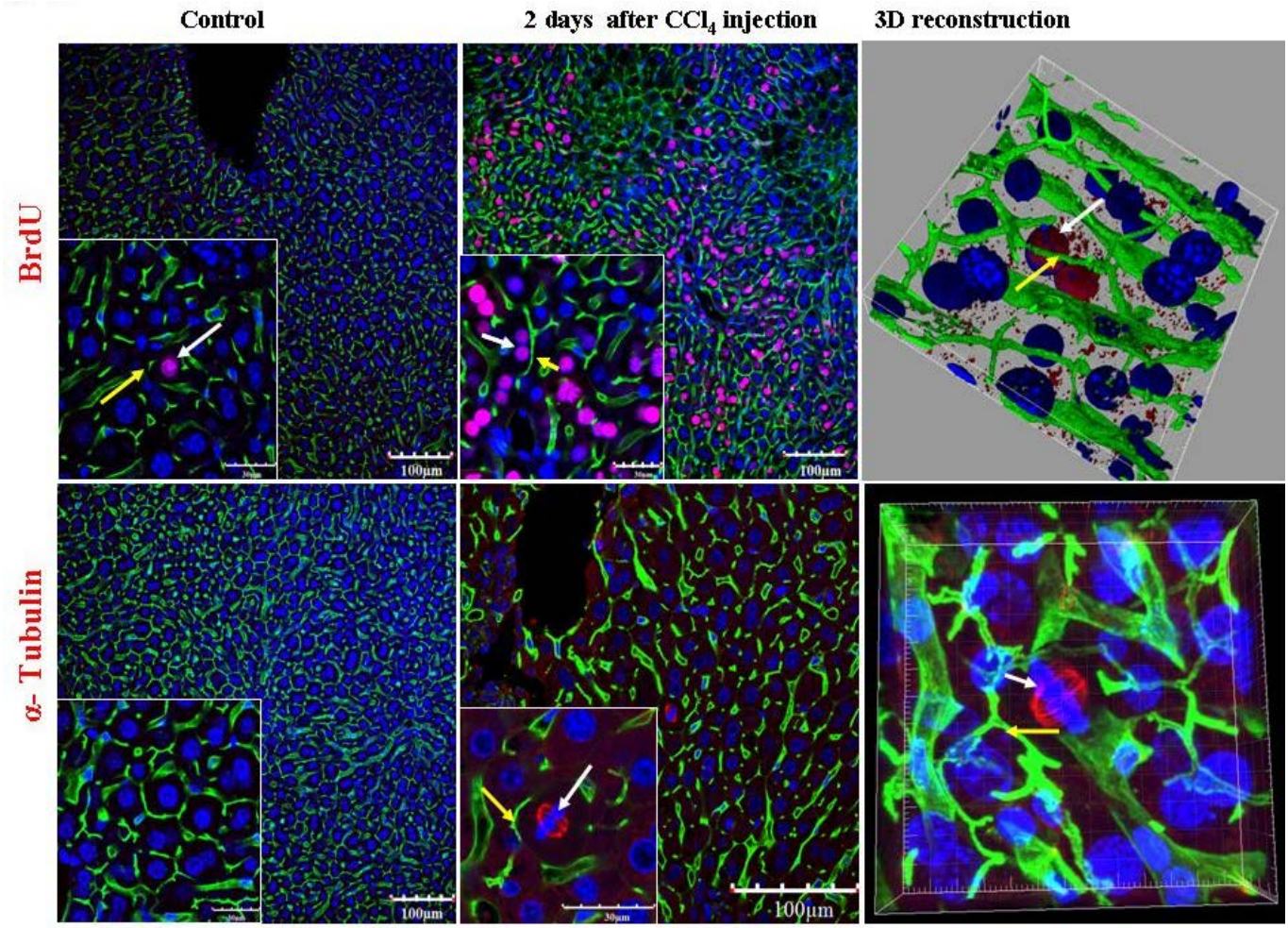

Figure 5.16. Immunofluorescence microscopy of DPPIV/CD26 on mouse liver slices during S-phase and metaphase. The expression of DPPIV/CD26 (green fluorescence, yellow arrow) maintained during the cell cycle. BrdU incorporated (S-phase marker, upper white arrows) hepatocytes labeled in red and hepatocytes in metaphase appeared in red using an alpha-tubulin (mitotic spindle protein, lower white arrows). The acquired image stacks were processed using Imaris 3D-rendering software. The scale bars are 100 and 30 µm in the low magnification and high magnification, respectively.

Radixin is the main member in hepatocytes, which is primarily localized to the apical membrane of hepatocytes (Wang et al., 2006). The immuno-positivity of the previous markers visualizes bile canaliculi pathways. In order to analyze hepatocytes in S-phase and M-phase, the previously described markers (DPPIV/CD26, Mrp2 and radixin) were costained with antibodies directed against BrdU and alpha-tubulin, respectively. The stained sections were scanned by confocal microscopy. In G0 hepatocytes, all markers were expressed specifically at the bile canalicular membrane of hepatocytes as expected, and formed a belt-like structure around the hepatocytes (Fig.5.16 and Fig.5.17). The distribution of the bile canalicular markers in the examined liver tissue was approximately homogeneous. There was no difference in the immunopositivity and localization of these proteins in the bile canaliculi of G0 and S- and M-phase hepatocytes. Thus, it can be concluded that hepatocytes are able to maintain their apical domains (DPPIV/CD26, Mrp2 and radixin) as well as bile forming capacities during proliferation.

5.3.2. Hepatocytes maintain basolateral domains during both S- and M-phases

The basolateral membrane of a liver cell represents approximately 85% of the total cell surface (Bacon et al., 2006; Kuntz and Kuntz, 2008). This membrane serves as: 1) a contact surface with hepatic sinusoids, where nutrients and blood constituents are exchanged between hepatocytes and hepatic sinusoids, and 2) hepatocyte-hepatocyte contact surface, where hepatocytes can communicate and exchange information with one another. In order to investigate alterations of the basolateral membranes of hepatocytes during cell cycle, an immunofluorescence technique was established using the following antibodies: 1) Low density lipoprotein receptor (LDLR) - a cell surface receptor that plays an important role in cholesterol homeostasis and is bound to the basolateral membrane of hepatocytes and 2) Epithelial Cadherin (E-Cadherin) - a cell surface protein and transcript under control of the transcription factor SNAIL (Cano et al., 2000).

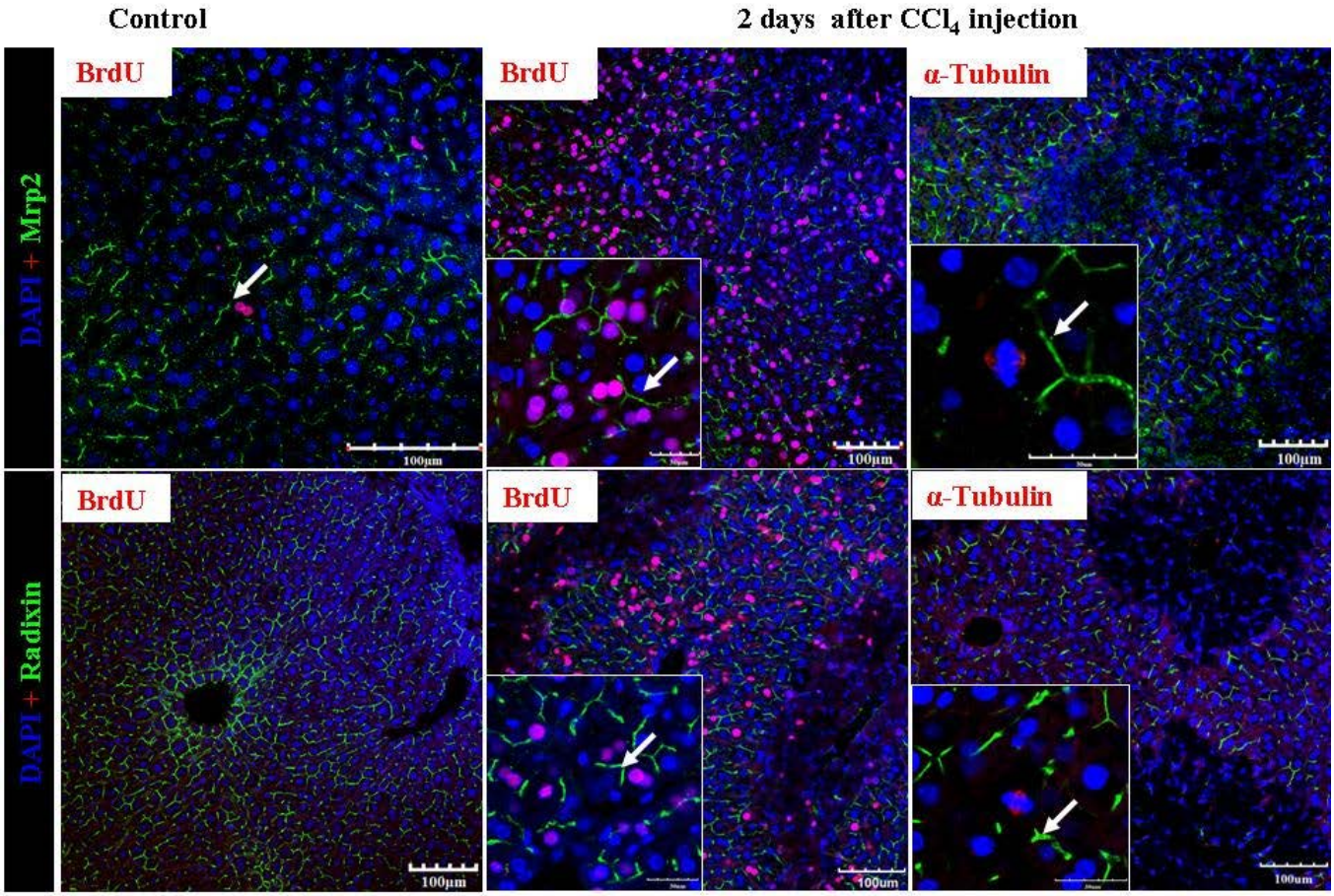

Figure 5.17. Immunoreactivity of both Mrp2 and radixin on the bile canaliculi during cell cycle. Hepatocytes maintained expression of Mrp2 (upper row, white arrows) and radixin during (lower row, white arrows) S-phase (red fluorescence) and metaphase (red fluorescence). The scale bars are 100 and 30 µm in the low magnification and high magnification, respectively.

E-Cadherin is important for cell adhesion and is expressed at the basolateral surface of the periportal hepatocyte. To investigate the hepatocyte in S and M-phase, the antibodies above (LDLR and E-cadherin) were co-stained with antibodies directed against BrdU and alpha-tubulin. The stained sections were scanned by a confocal microscope. In G0 hepatocytes, all markers were specifically expressed at the basolateral surface. This localization was comparable to the situation in both S- and M- phase hepatocytes (Fig. 5.18). In conclusion, hepatocytes are able to maintain their basolateral domains (LDLR and E-cadherin) during liver regeneration.

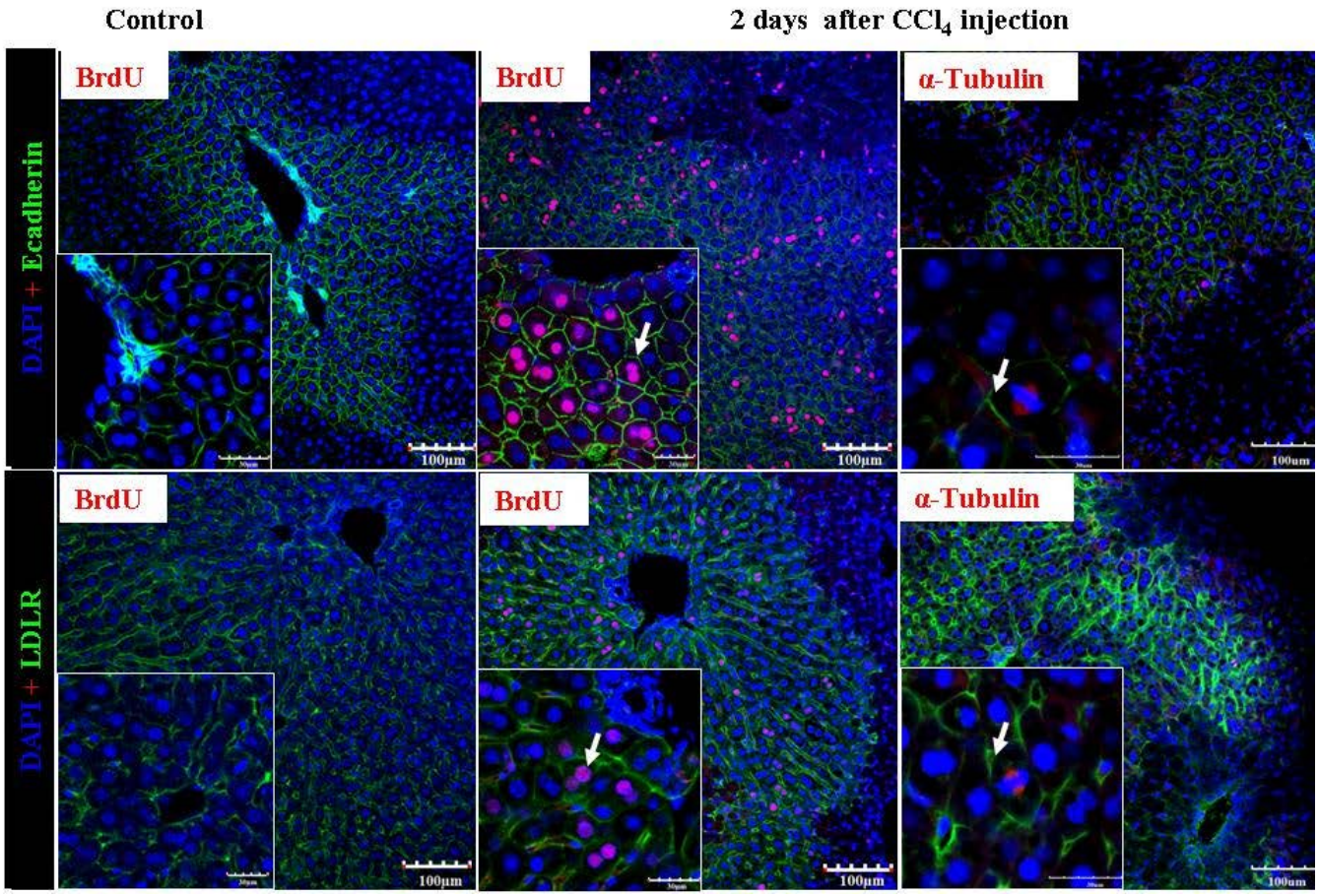

Figure 5.18. Immunolocalization of E-cadherin and LDLR at the basolateral surface of the hepatocytes during cell proliferation. Hepatocyte maintained expression of E-cadherin (green fluorescence, upper row) and LDLR (green fluorescence, lower row) during S-phase (red fluorescence, left and middle column) and metaphase (red fluorescence, right column). The scale bars are 100 and 30 μm in the low magnification and high magnification, respectively.

5.3.3. Hepatocytes preserve claudin1 (tight junction protein) during both S- and M-phases

Tight junctions (zonula occludens) are the closely associated areas that separate the apical from the basolateral membranes between hepatocytes forming an impermeable barrier. It maintains the polarity of cells by preventing the lateral diffusion of integral membrane proteins between the apical and basolateral membranes. It also prevents bile diffusion into the blood stream. Claudin1 is one of tight junction–associated proteins that localizes to the apical membrane of hepatocytes. To determine the localization of

claudin1 at the apical membrane of proliferating hepatocytes, the claudin1 antibody was co-stained with antibodies directed against BrdU and alpha-tubulin. The stained slices were scanned by confocal microscopy. In G0 hepatocytes, claudin1 was specifically expressed at the apical pole of hepatocytes. This was comparable to the situation in both S- and M- phase hepatocytes (Fig.5.19). Therefore, hepatocytes are able to maintain their physiological arrangement of tight junction during regeneration.

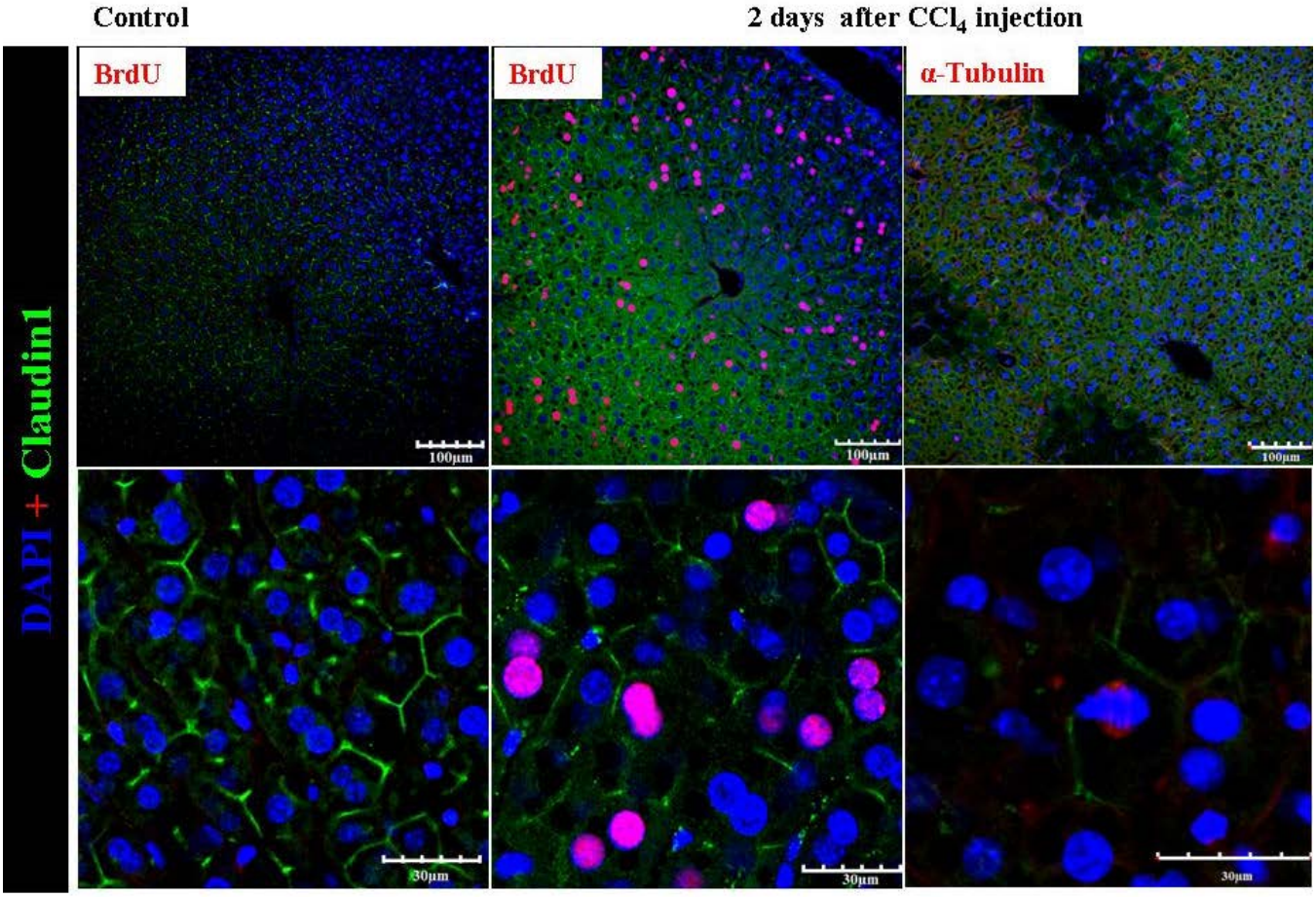

Figure 5.19. Immunopositivity of a tight junction protein (claudin1) during cell division. Hepatocyte preserved expression of claudin1 during S-phase and metaphase. The scale bars are 100 and 30 µm in the low magnification and high magnification, respectively.

5.3.4. Bile canaliculi are preserved during different phases of mitosis

The existence of bile canaliculi during different stages of mitosis were analyzed in livers after carbon tetrachloride intoxication. The liver slices co-stained with alpha-tubulin and

DPPIV/CD26 to visualize the mitotic spindle and bile canaliculi, respectively. Subsequently, the liver sections were scanned by a confocal scanning microscope. The acquired image stacks were processed using Imaris 3D-rendering software. The DPPIV/CD26 immunoreactivity was positive at the bile canaliculi of the hepatocytes (white arrows) undergoing prophase (Fig. 5.20A), prometaphase (Fig. 5.20B), metaphase (Fig. 5.20C), anaphase (Fig. 5.20D) and telophase (Fig. 5.20E). Thus, it can be concluded that hepatocytes are able to maintain their apical domain (DPPIV/CD26) during different phases of mitosis.

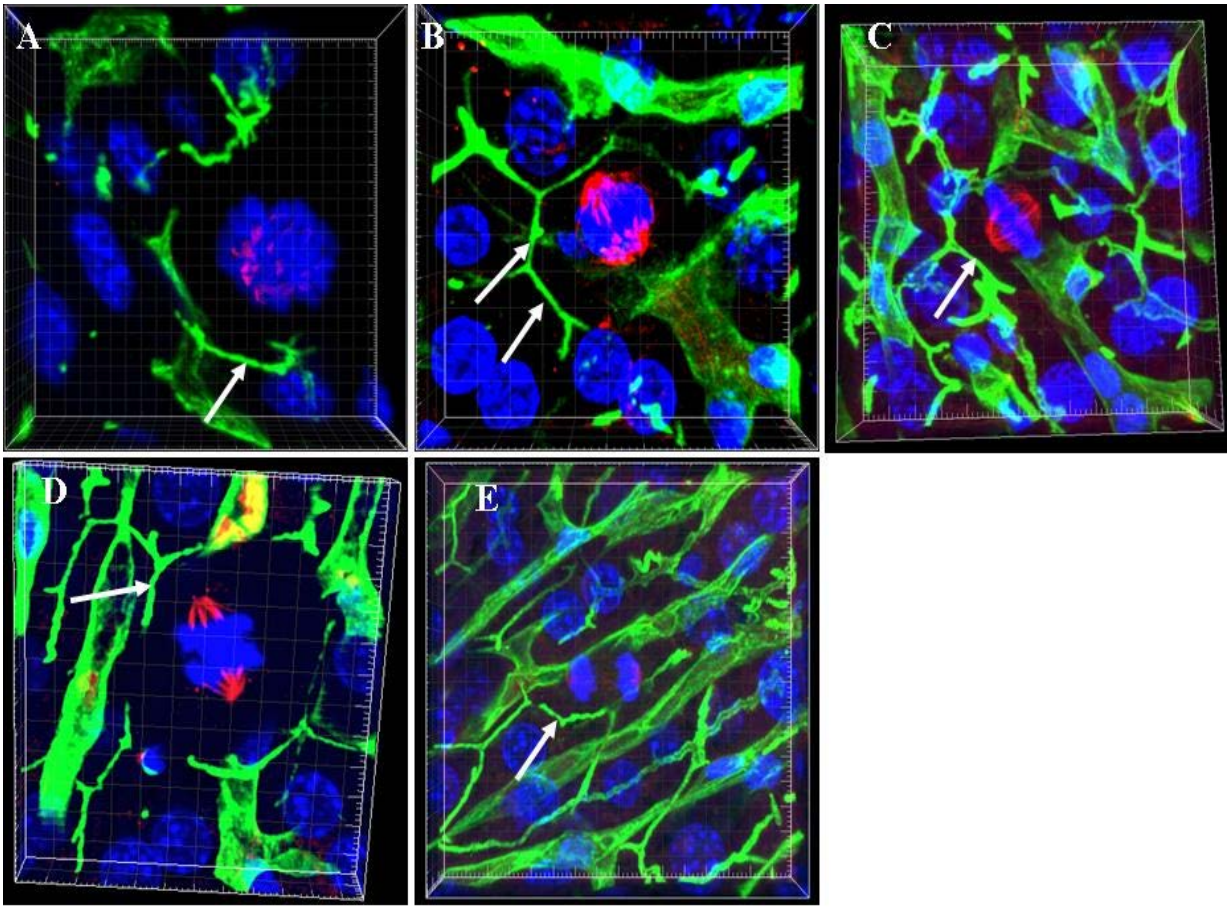

Figure 5.20. Hepatocytes maintained the bile canaliculi during different phases of mitosis. The acquired image stacks were generated by a confocal microscope and were processed using Imaris 3D-rendering software. The mitotic spindle was visualized by α-tubulin staining (red fluorescence). DPPIV/CD26 was expressed at the apical membrane (white arrows) of the hepatocytes different stages of mitosis (A) prophase, (B) prometaphase, (C) metaphase, (D) anaphase and (E) telophase and cytokinesis.

5.3.5. Establishment of bile canaliculi between daughter hepatocytes

The daughter hepatocytes aligned along the nearest hepatic sinusoidal endothelial cell, and the hepatic architecture was restored within two weeks after intoxication (Hoehme et al., 2010). To prove that the bile canaliculi established between the daughter hepatocytes, a pulse-chase experiment was performed. In this experiment, male C57BL/6N mice were treated intraperitoneally with a single dose of 1.6 g/kg carbon tetrachloride and exposed intraperitoneally to a dose of 80 mg/kg BrdU at 46 hours after intoxication. The mice were sacrificed at 0, 2, 4, 6, 8, 10, 12, 24, 48, 72, 96 hours after BrdU injection (Fig. 4.2). Three mice were collected for each of the time periods. Liver sections of control and carbon tetrachloride-treated mice were co-stained with antibodies directed against BrdU, Mrp2 and DPPIV/CD26. Liver sections were scanned using a confocal scanning microscope and Z-stacks were prepared. The acquired image stacks were processed using Imaris 3D-rendering software. The neighboring hepatocytes retained bile canaliculi during S-phase (Fig. 5.16, Fig. 5.17, Fig.5.21A) and M-phase (Fig. 5.16, Fig. 5.17, Fig.5.21B and C). The majority of BrdU-incorporated hepatocytes entered M-phase between 6 and 10 hours after BrdU injection in agreement with text book literature. The bile canaliculi then established between daughter cells after cytokinesis between 10 and 24 hours after BrdU incorporation. Thus, the bile canaliculi are established between the daughter hepatocytes directly after cell division. The newly formed bile canaliculi may have originated from an already existing network or a bleb in the membrane of daughter cells or possibly from both origins. To investigate these theories, a pulse-chase experiment was performed. Liver sections of control and intoxicated mice were co-stained with antibodies directed against BrdU, Mrp2 and DPPIV/CD26. Z-stacks were prepared using a confocal microscope. The acquired image stacks were processed using Imaris 3D-rendering software. Surprisingly, the immunoreactivity for DPPIV/CD26 and Mrp2 between the daughter hepatocytes was not observed. This means the bile canaliculi originated from an already established neighboring network (Fig.5.21B and C). The careful analysis of 8, 10 and 12 hours after

BrdU administration revealed the presence of unconnected branches of bile canaliculi as well as an invagination of the bile canalicular belt. These branches started from the existing network and invaded the cleavage furrow. In conclusion, the daughter cells established their apical sides through an invagination and bleb formation on the already existing canalicular network. A novel bile canalicular branch established between the daughter hepatocytes.

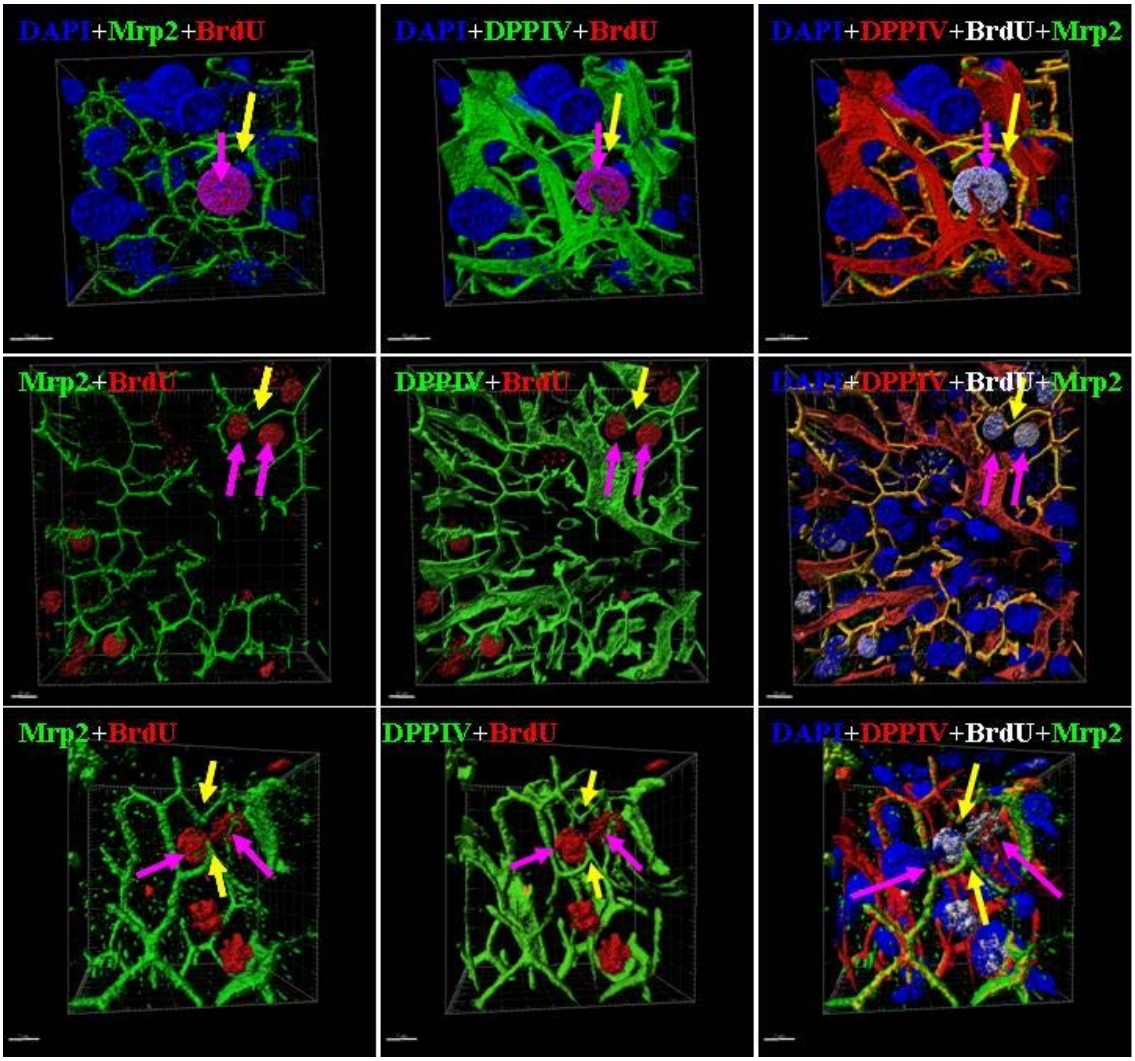

Figure 5.21. Establishment of bile canaliculi between daughter hepatocytes. The liver slices were co-stained with antibodies directed against BrdU (daughter cell marker), DPPIV/CD26 and Mrp2 (both are bile canalicular marker). The acquired image stacks were generated by a confocal microscope and were processed using Imaris 3D-rendering software. Pink arrows show the BrdU incorporated nuclei and the yellow arrows refer to the bile canalicular around the corresponding hepatocyte.

5.4. Reconstruction of the bile canalicular network of the normal, intoxicated, regenerated and fibrotic livers

The bile canalicular domain represents approximately 15% of the hepatocyte surface (Bacon et al., 2006). Bile canaliculus is a space 0.5-2 µm wide formed between the adjacent hepatocytes (Ludwig et al., 1998; Boyer et al., 2006). The bile canaliculi are interconnected, build a network and drain the bile through bile ductules at the portal triads. Currently, no technique is available to quantify this network. To bridge this gap and to better understand the architecture of the bile canalicular network, a method for analyzing three dimensional organizations of the bile canaliculi and hepatic sinusoids using confocal images was established. The mouse livers were sliced using a vibratome into relatively deep (75µm) sections. Subsequently, the liver sections were immunostained by antibodies directed against DPPIV/CD26 and glutamine synthetase (section 4.5.1). The hepatic microvasculature was visualized by the DMs labeling. The slices were counterstained with DAPI and were scanned using a confocal laser scanning microscope then Z-stacks were generated. Z-stack processing and manipulation were performed by Imaris software. The reconstructed Z-stack was used to investigate the organization of liver micro-architecture and bile canalicular network (Fig. 5.22).

5.4.1. Reconstruction of the bile canalicular network of the normal livers

In normal livers, the bile canaliculi form a low order network which contains a repetitive basic unit that may show some degree of variability. This basic unit is formed of three hepatocytes; most hepatocytes are surrounded by three half-hexagonal belts of bile canaliculi and one sinusoid in the center.

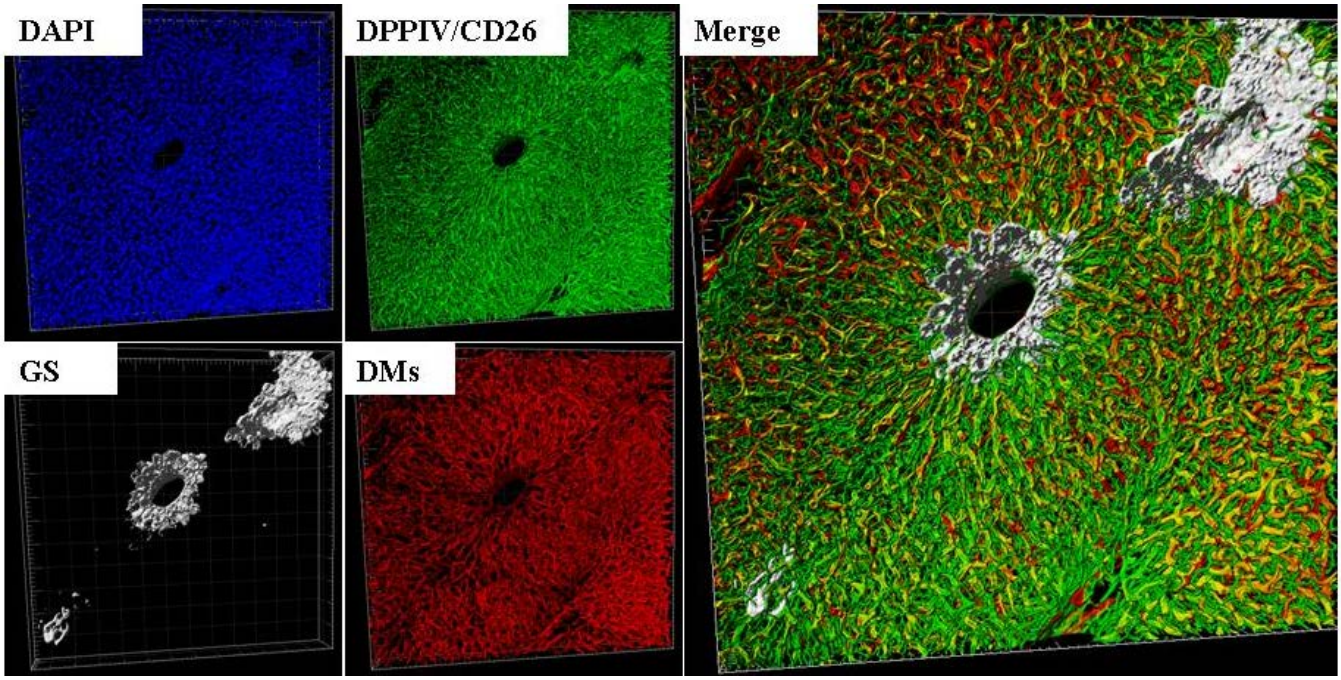

Figure 5.22. A confocal Z-stack of deep liver slices after Imaris processing (normal mouse liver). The bile canalicular network was visualized by DPPIV/CD26 (green fluorescence), the liver microvasculature was recognized by DMs (red and yellow fluorescence), the central veins are detected by glutamine synthetase (white fluorescence) and the nuclei were counterstained with DAPI (blue fluorescence). The staining protocol is described in section 4.5.1. The Z-stack was generated by a confocal microscope and was processed by Imaris software. The scale bar of the original dataset is 100 μm.

5.4.1.1. The bile canaliculi form three half-hexagonal belts around the hepatocytes

The basic unit is formed of a hepatocyte with three half-hexagonal belts of the bile canaliculi. To visualize this unit, deep liver slices were immunostained with antibodies directed against DDPIV/CD26 and GS (section 4.5.1). The Z-stack was produced using a confocal laser scanning microscope and was processed by Imaris software. The three half-hexagonal belts of bile canaliculi (Fig. 5.23A, white arrow) indicated the triangular nodal formation around hepatocytes. These basic units were repeated in an irregular fashion. An idealized hepatocyte including the half-hexagonal belts and the sinusoids was designed using AutoCAD software. The hepatocyte was designed as a polygonal object (Fig. 5.23B, black object). It contained three membranes and twelve facets.

However, this cell shape represents a theoretical assumption and was not derived from Z-stacks. The bile canaliculi were represented as three half-hexagonal belts surrounding the hepatocyte (Fig. 5.23B, green tubes) and the hepatic sinusoids were visualized as red cylinders (Fig. 5.23B, red cylinder). In this idealized version the hepatocyte contained three half-hexagonal belts of bile canaliculi and surrounded by three hepatic sinusoids.

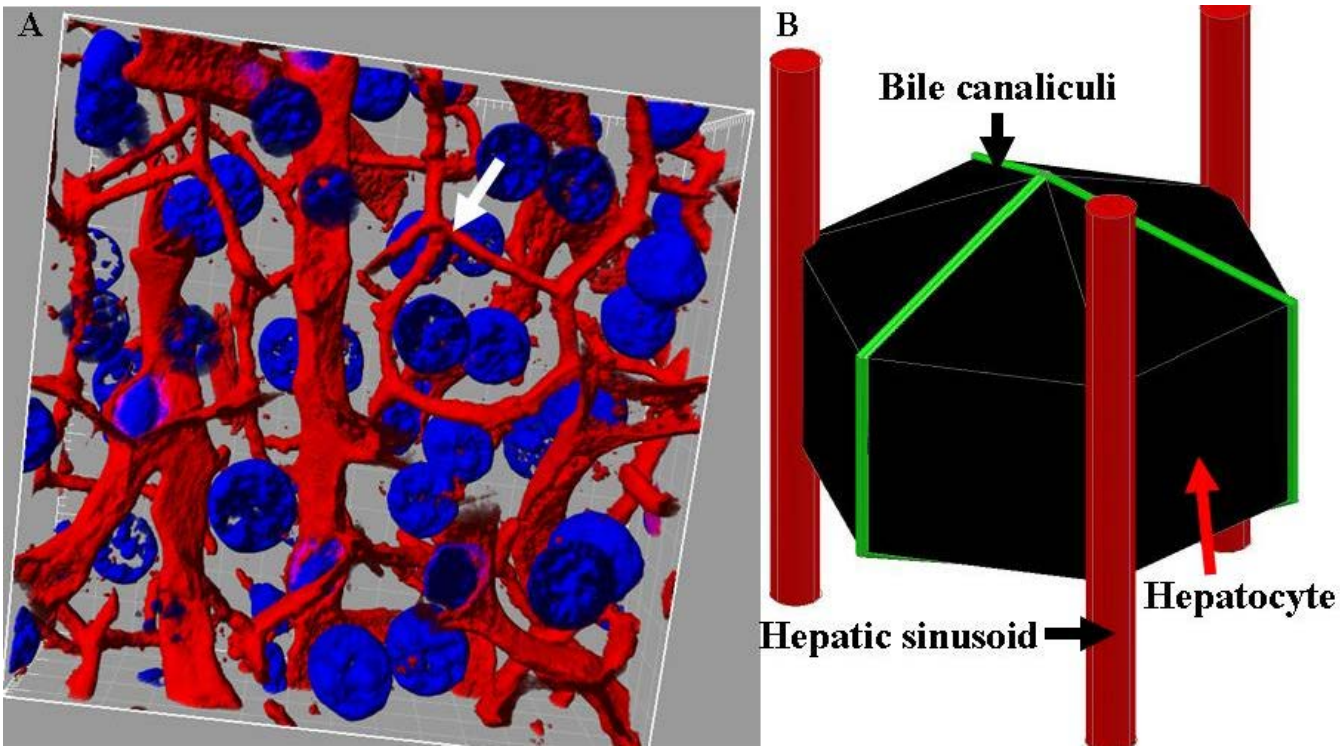

Figure 5.23. The bile canaliculi form three half-hexagonal belts around the hepatocytes. The bile canalicular network was investigated in deep liver slices. A) The bile canalicular network was visualized by DPPIV/CD26 (red fluorescence, thin tubular structure) and the nuclei were counterstained with DAPI. The Z-stack was processed by imaris software. The white arrow indicates the triangular nodal formation of bile canaliculi around binucleated hepatocytes. The scale bar of the original dataset is 100 µm. B) Using AutoCAD software, one idealized hepatocyte was designed (black object), the bile canalicular network was visualized as green connected tubes and the hepatic sinusoids were represented as red tubes.

5.4.1.2. Two classes of bile canaliculi

According to their orientation to the closest hepatic sinusoid, two classes of bile canaliculi can be differentiated. The first (primary canaliculi) classes (Fig. 5.24A red

dashed lines) are parallel to the closest hepatic sinusoid (Fig. 5.24A white dashed lines). The second (secondary canaliculi) classes (Fig.5.24A pink lines) are perpendicular to the closest hepatic sinusoid (Fig. 5.24A white dashed lines). This organization was also represented in the idealized schedule of a single hepatocyte (Fig.5.24B). In this schedule, the angle between the first and second class bile canaliculi is approximately 105°. Therefore, the first class (Fig. 5.24B red dashed line) is parallel to the hepatic sinusoid (Fig. 5.24B white dashed line). The second class (Fig. 5.24B pink line) is almost perpendicular on both hepatic sinusoid and first class.

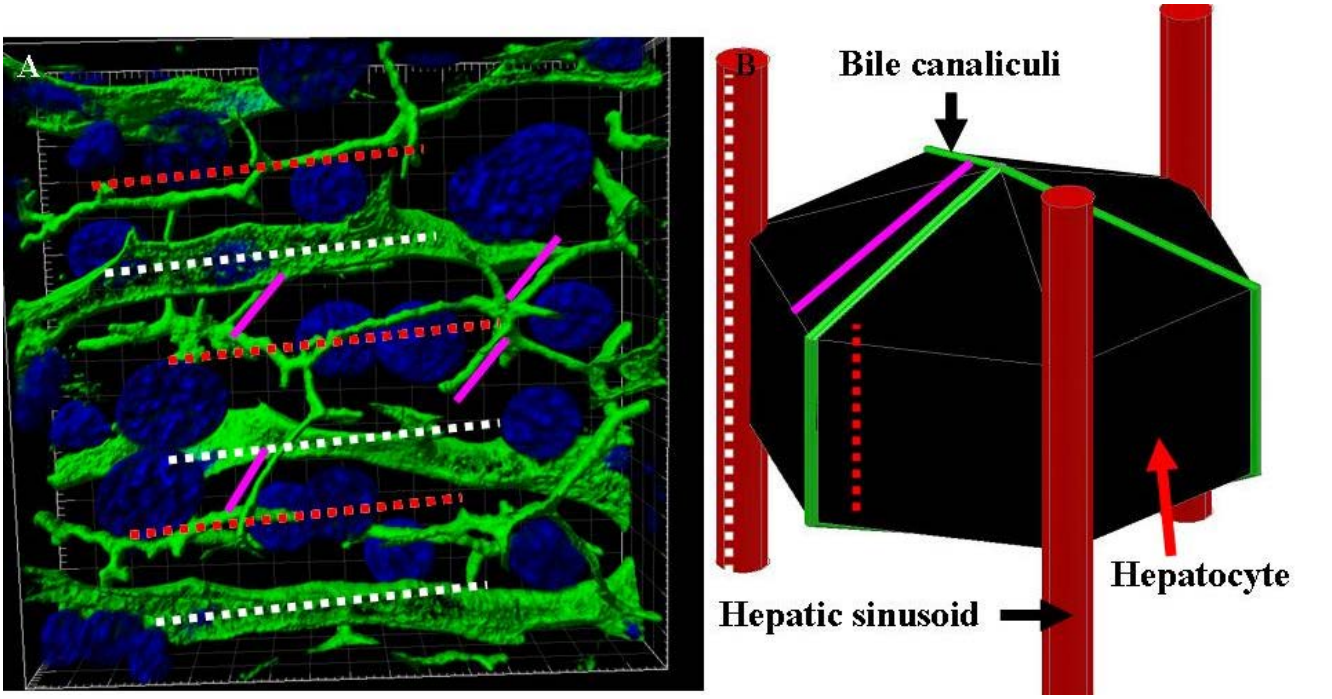

Figure 5.24. The bile canalicular network forms two classes based on their alignment to the closest sinusoid. A) The bile canalicular networks were investigated in deep liver slices. The bile canalicular network was visualized by DPPIV/CD26 (green fluorescence, thin tubular structure) and the nuclei were counterstained with DAPI. The Z-stack was processed by Imaris software. The red dashed lines refer to the primary classes of the bile canalicular network while the pink lines indicate the secondary classes. Both classes were differentiated according to their alignment (parallel or perpendicular) to the closest hepatic sinusoids (white dashed lines), respectively. The scale bar of the original dataset is 100 µm. B) Using AutoCAD software, the bile canalicular network contains two classes parallel (red dashed line) or perpendicular (pink line) to the hepatic sinusoids (white dashed line).

5.4.1.3. Three hepatocytes surrounding one sinusoid form a frequently observed basic building block

In the previous (one cell based) model, the presence of the three half-hexagonal belts of bile canaliculi was observed as a frequent scenario. Next, the previous model was extended to include three hepatocytes. The three-cell-based model was composed of a hepatic sinusoid in the center surrounding by three hepatocytes. This unit was frequently seen in the liver sections (Fig. 5.25A) and therefore, named basic building block. The AutCAD design of the basic building block was performed (Fig. 5.25B). In this design the hepatic sinusoid (Fig. 5.25B, yellow arrow) was surrounded by three hepatocytes (black objects).

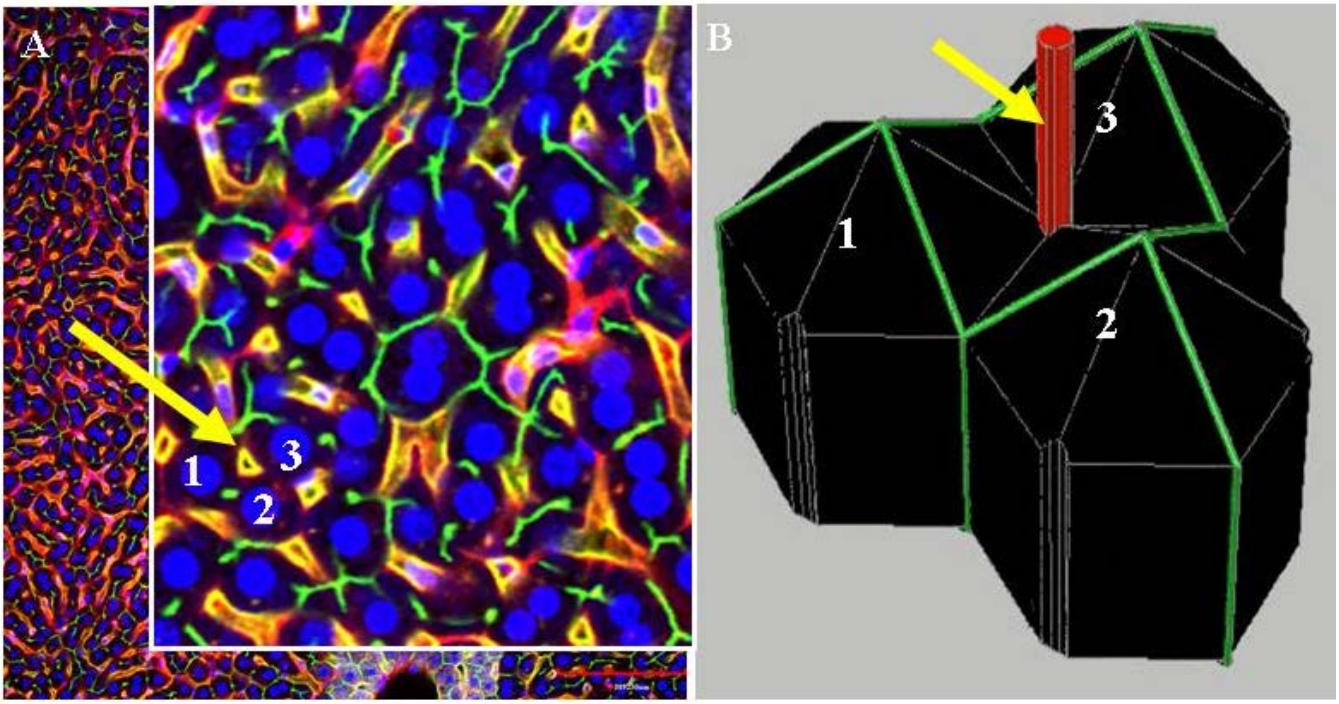

Figure 5.25. Observation of a basic building block consisting of one sinusoid and three hepatocytes. A) The yellow arrow refers to the hepatic sinusoid which was surrounded by three hepatocytes named 1, 2 and 3. The scale bar of the original dataset is 100 µm. B) The AutoCAD design of the basic building block was carried out. The hepatic sinusoid (yellow arrow) was surrounded by three connected hepatocytes named 1, 2 and 3..

5.4.1.4. Hepatic sinusoids surrounded by a hexagonal belt of bile canaliculi

To investigate the intertwined networks of hepatic sinusoids and bile canaliculi, deep liver slices were immunostained with architectural staining (section 4.5.1). The networks were reconstructed using Imaris software. The bile canaliculi formed complete or incomplete belts (Fig. 5.26A, white arrows) around the hepatic sinusoids (Fig. 5.26A, yellow asterisk). Therefore, there are two types of bile canalicular belts the first one is surrounding the hepatocyte (Fig. 5.23A) and the second type of belt surrounds the hepatic sinusoids (Fig. 5.26A). For better understanding of this situation, an idealized drawing was made using AutoCAD. Similar, as seen in the reconstructed Z-stacks, the idealized drawing contains three hepatocytes with a hepatic sinusoid (Fig. 5.26B, yellow asterisk) in the center. The bile canaliculi were included as three half-hexagonal belts around each hepatocyte (Fig. 5.26B). The resulting idealized picture illustrates the following aspects: 1) a hexagon of bile canaliculi surrounds the hepatic sinusoid; 2) in agreement with figure 5.23A, each hepatocyte is surrounded by three half-hexagonal belts of bile canaliculi and 3) this unit is formed by three hepatocytes and one hepatic sinusoid. These characteristics of the idealized picture correspond well to the features observed in the Z-scans.

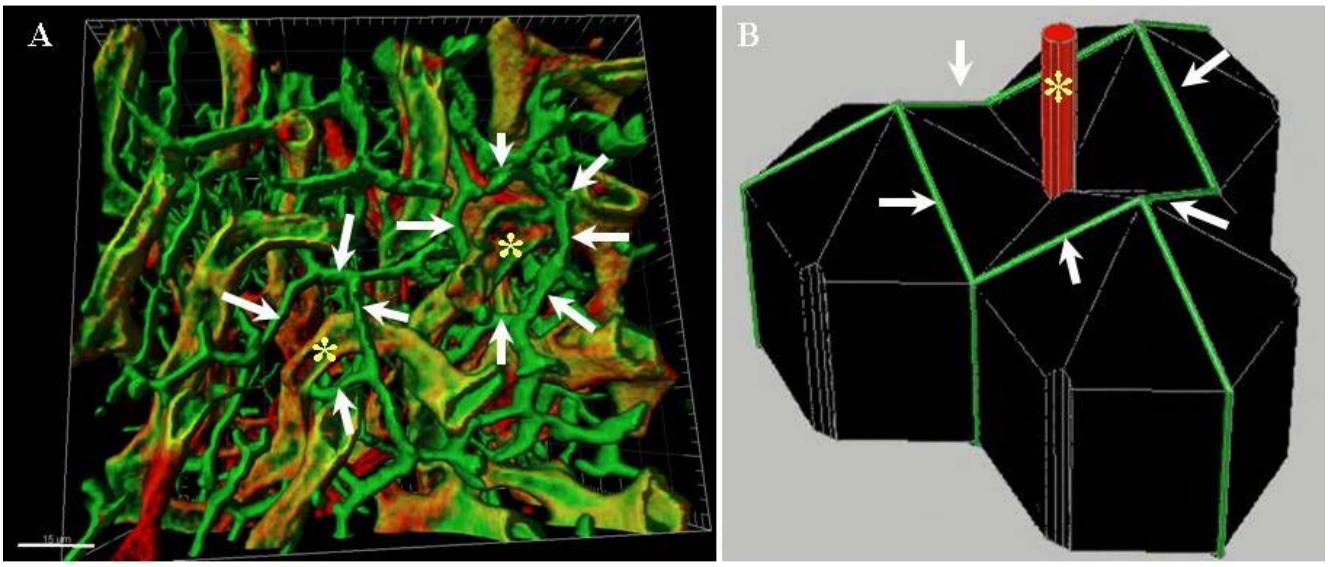

Figure 5.26. The hepatic sinusoid is surrounded by complete or incomplete belt of bile canaliculi. A) To investigate this hypothesis, deep liver slices were immunostained as described in section 4.5.1. The yellow asterisk indicates the hepatic sinusoid which was surrounded by a belt of bile canaliculi (white arrows). The scale bar of the original dataset is 30 μm. B) In the idealized version using AutoCAD software, the hepatic sinusoid (asterisk) was surrounded by a hexagonal belt of bile canaliculi (white arrows).

5.4.1.5. Unconnected branches of the bile canalicular network ´dead ends`

To further evaluate the integrity of the bile canalicular network, the deep liver slices were immunostained with the architectural staining (section 4.5.1). Z-stacks were generated by a confocal scanning microscope and were processed using Imaris software. Careful analysis of the deep liver slices revealed the presence of several unconnected (connected only from one side) branches of the bile canalicular network (Fig. 5.27, yellow arrows). These branches had normal bile canalicular morphology and varied in their length.

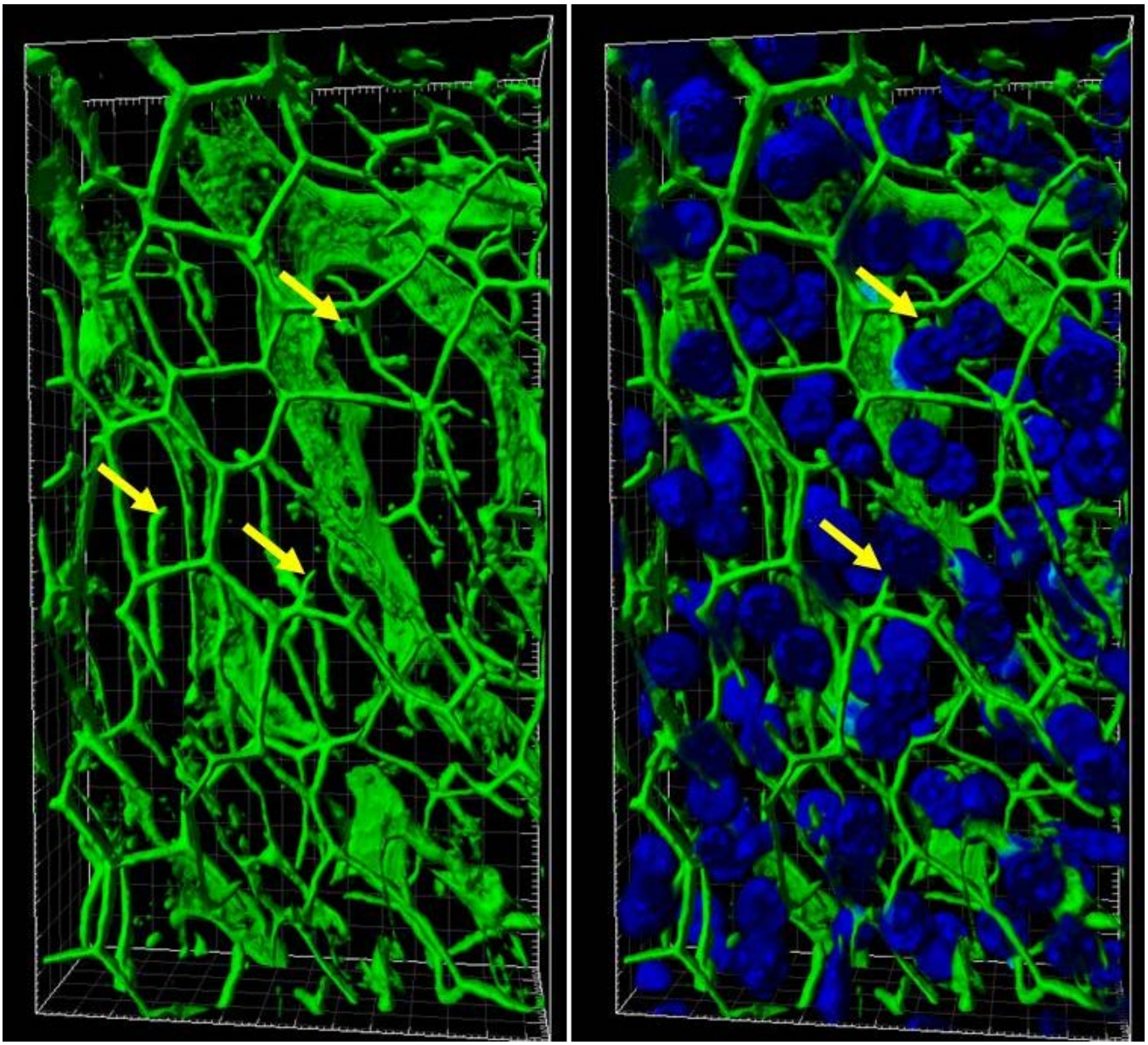

Figure 5.27. Unconnected branches of the bile canalicular network. Left image shows the reconstructed DPPIV/CD26 immunostained section with several unconnected branches (yellow arrows) and the right image is the corresponding reconstruction with DAPI. The scale bar of the original dataset is 20 μm.

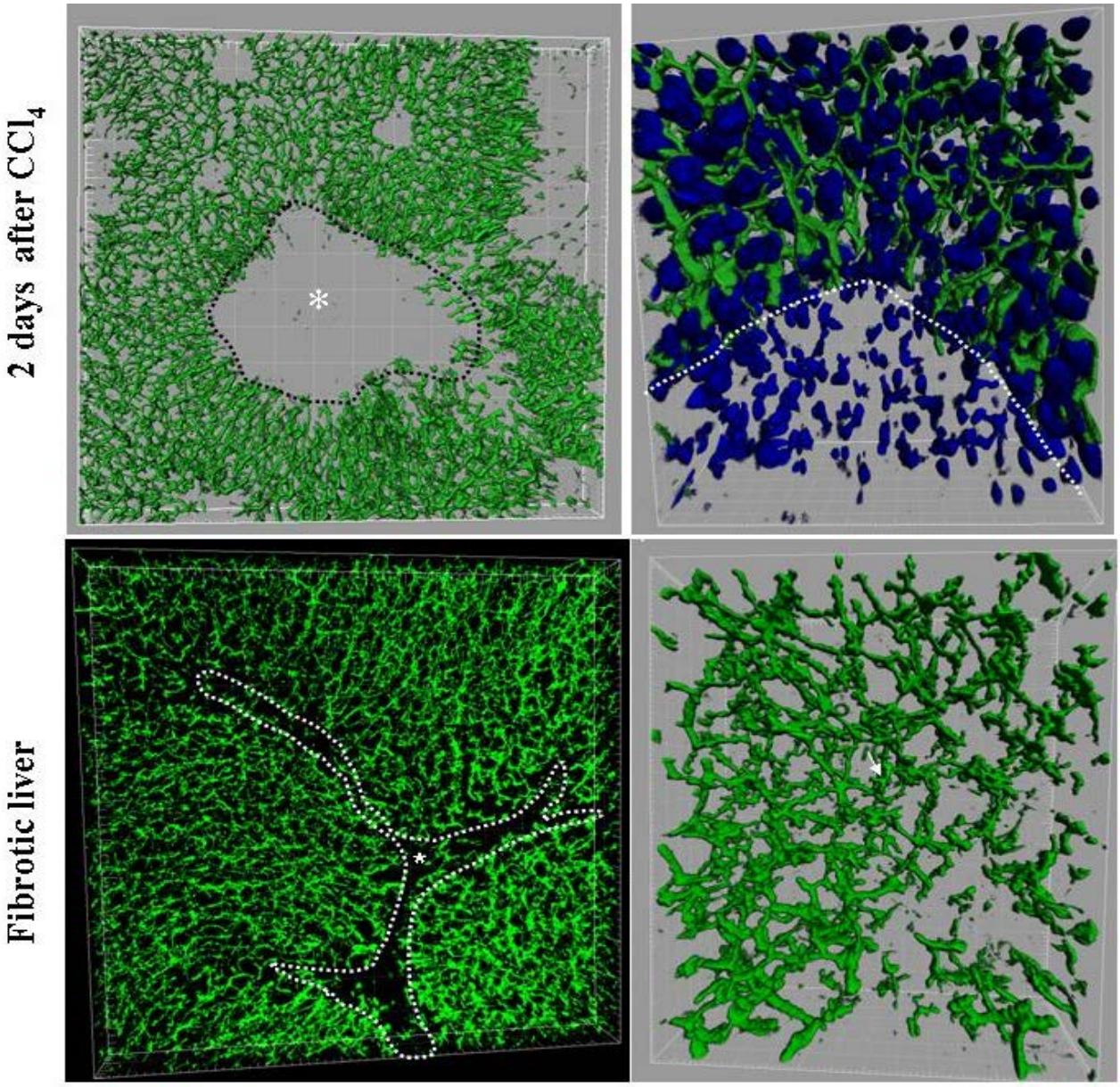

Figure 5.28. Disruption of the bile canalicular network after intoxication and fibrosis. The disrupted hepatic micro-architecture was investigated using deep liver slices of CCl_4-treated mice and fibrotic livers. The liver slices have been immunostained as described in section 4.5.1. The Z-stacks were produced using a confocal scanning microscope and were processed by Imaris software. The centrilobular hepatocytes were destroyed by intoxication and the hepatocyte nuclei disappeared and the bile canalicular network was disrupted at the central part of the lobule (upper row, asterisk). In fibrotic livers, the hepatocyte disappeared at fibrotic bands (asterisk) and the curling as well as the unconnected branches of the bile canaliculi were obvious. The scale bars are 100 μm and is 20 μm .

5.4.2. Bile canalicular network integrity during intoxication and fibrosis

To investigate the integrity of the bile canalicular network during liver intoxication, male C57BL/6N mice were treated intraperitoneally with a single dose of 1.6 g/kg carbon tetrachloride (Fig. 4.1). To induce liver fibrosis, the experimental design was described in section 4.1.3. Liver sections from the intoxicated and fibrotic livers as well as control livers were scanned using a confocal microscope and Z-stacks were generated. The acquired image stacks were processed using Imaris 3D-rendering software. The key features of the damaged bile canalicular network are: i) interruption at the border of the central dead cell region as well as at the fibrotic regions (Fig. 5.28, selected areas); and ii) more unconnected branches (dead ends) and curling of the bile canaliculi (white arrow).

6. Discussion

6.1. Carbon tetrachloride intoxication as a model situation for acute liver damage

One of the main functions of the liver is xenobiotic biotransformation and detoxification. Although there are many reports on the mechanisms of liver intoxication and detoxification, very little is known about the organization of the hepatic micro-architecture during the intoxication, regeneration and fibrosis processes. Liver physiology and pathophysiology are tightly dependent on the hepatic micro-architecture. Currently, no technique is available to quantify liver micro-architecture (Hoehme et al., 2010). Therefore, the goal of the current PhD thesis is to initially describe the bile canalicular network in healthy mouse liver, and use this to compare the situation to the network in acute and chronic liver damage. For this purpose, an in vivo scenario for acute liver damage was needed. Since carbon tetrachloride intoxication is frequently used for the induction of acute liver damage (Kuo and Darnell, 1991; Gebhardt, 1992; Yamada and Fausto, 1998; Hoehme et al., 2007; Alhassan et al., 2009; Dalton et al., 2009; Hoehme et al., 2010; Wei et al., 2010) this in vivo system was chosen for the present study. One preliminary study was to compare the basic features of the liver intoxication data in the present study to published data. For this purpose, mice were exposed to a toxic dose of carbon tetrachloride (1.6g/kg body weight) to induce acute liver damage (Fig. 4.1). The mouse body weight was decreased by 9.17 and 9.14% at days one and two, respectively (Fig. 5.5). Since this decrease was less than ten percent of the mouse body weight it was not considered as a major weight loss. Liver-to-body-weight ratio (Fig. 5.5) increased on days three and four. The results corresponded to already published data of Dorn and colleagues (Dorn et al., 2012). The liver damage was seen as whitish spots during the first 72 hours (Fig. 5.6) after carbon tetrachloride intoxication (Hoehme et al., 2010, supplemental data page 7; Dorn et al., 2012). These spots disappeared gradually and the normal situation was recovered on day four, corresponding to the quantification of the centrilobular necrotic areas (Fig. 5.7, Tab. 5.1

and Fig. 5.8). To study regeneration after carbon tetrachloride-driven liver damage, hepatocyte proliferation was quantified after BrdU administration (Fig. 5.10, Tab. 5.2 and Fig. 5.11). The maximal hepatocyte proliferation occurred on days two and three after intoxication in agreement with (Yamada and Fausto, 1998; Hoehme et al., 2010; Wei et al., 2010). The number of hepatocyte nuclei per square millimeter was quantified and the results showed that the number of nuclei decreased to a maximal level on day two after a toxic challenge, followed by recovery to the control level on day five (Fig. 5.12, Tab. 5.2). The centrilobular necrosis was confirmed by immunostaining and scanning of deep liver slices with confocal microscopy. It was shown (Fig. 5.9) that the injured areas were centrilobular compartments of the hepatic lobule (Kuo and Darnell, 1991; Gebhardt, 1992; Hoehme et al., 2010). Overall, data obtained in the present study correspond to previously published data (Yamada and Fausto, 1998; Alhassan et al., 2009; Dalton et al., 2009; Hoehme et al., 2010). Therefore, the liver tissue after carbon tetrachloride administration could be used to analyze the bile canalicular network under conditions of acute liver damage.

6.2. Prolonged administration of carbon tetrachloride as a model situation for liver fibrosis

Liver fibrosis is induced by chronic damage to the liver, and is characterized by accumulation of collagen and extracellular matrix proteins (Bataller and Brenner, 2005). To induce liver fibrosis, mice were exposed to carbon tetrachloride (Sakaida et al., 2004; Constandinou et al., 2005; Jeong et al., 2006; Teixeira-Clerc et al., 2006; Domenicali et al., 2009) three times weekly for six weeks (Fig. 4.2). Using hematoxylin and eosin staining, the liver sections revealed accumulation of macrophages and myofibroblasts as well as activated stellate cells in the damaged area (Fig. 5.14 H&E). The picro-sirius red staining confirmed the deposition of collagen and extracellular matrices at the central compartment of the hepatic lobule and extensive bridging between central veins (Fig.5.14 picro-sirius red staining). This type of fibrosis was

septal fibrosis (Zhao et al., 2005) and led to formation of a pseudolobulation (Chobert et al., 2012). Furthermore, the quantification of the alpha-smooth muscle actin positive area (Fig. 5.14 α-SMA) verified the presence of liver fibrosis (Bataller and Brenner, 2005; Zhao et al., 2005; Jeong et al., 2006). There were dramatic alterations in the organization of the hepatic micro-architecture (Fig. 5.15, architectural staining) as well as deposition of collagen and extracellular matrix at the borders of a pseudolobule (Fig. 5.15, collagen III staining). Thus, the liver tissue after repetitive administration of carbon tetrachloride could be used to analyze the bile canalicular network under conditions of liver fibrosis.

6.3. Maintenance and establishment of hepatocyte polarity during liver intoxication and regeneration

There is asymmetric distribution of the protein and lipid content of hepatocyte membranes (Simons et al., 1988; van Meer et al., 1988). This distribution reflects the different functions of the basolateral and apical poles, which in turn controls the balance between architecture stability and tissue plasticity. One of the most critical processes that have to be accomplished at the cellular scale is polarity establishment. Establishment of cell polarity is well studied in cultivated cells (in vitro system). Cell polarity is established according to the simplified schedule (Fig. 6.1A, from the review: Hoehme et al., 2012) of the basic machinery (Martin-Belmonte and Mostov, 2008): (i) The cell-cell contact initiates the formation of both adherent and tight junctions; (ii) Polarity complex proteins localize to the tight junctions including Par3 (partitioning-defective protein 3); (iii) PTEN (phosphatase and tensin homolog) localizes in the apical region. PTEN leads to enrichment of phosphatidylinositol 4,5-bisphosphate at the apical region and restricts phosphatidylinositol 3,4,5-trisphosphate to the basolateral domain; (iv) PI3K (phosphatidylinositol 3-kinase) localizes to the adherent junctions and support the presence of phosphatidylinositol 3,4,5-trisphosphate at the basolateral region; (v) Phosphatidylinositol 4,5-bisphosphate at the apical membrane recruits and promotes

Cdc42 (cell division cycle 42). This process can be enhanced by further factors (GEFs, Annexin 2, etc.). Active Cdc42 activates Par 6 (partitioning-defective protein 6) /aPKC (atypical protein kinase C) and other polarity complexes and in turn maintain the apical domain; (vi) Active Cdc42 mediates exocytosis. This process leads to fusion of a specialized organelle, the actin cytoskeleton and the vacuolar apical compartment (VAC), with the plasma membrane to form the apical lumen; (vii) Membrane detachment and luminal space can be induced and enhanced through several anti-adhesive factors e.g., large transmembrane glycoproteins or polysaccharides; and (viii) A complex transport machinery is established that orchestrates the sorting of proteins to either the apical or the basolateral membranes.

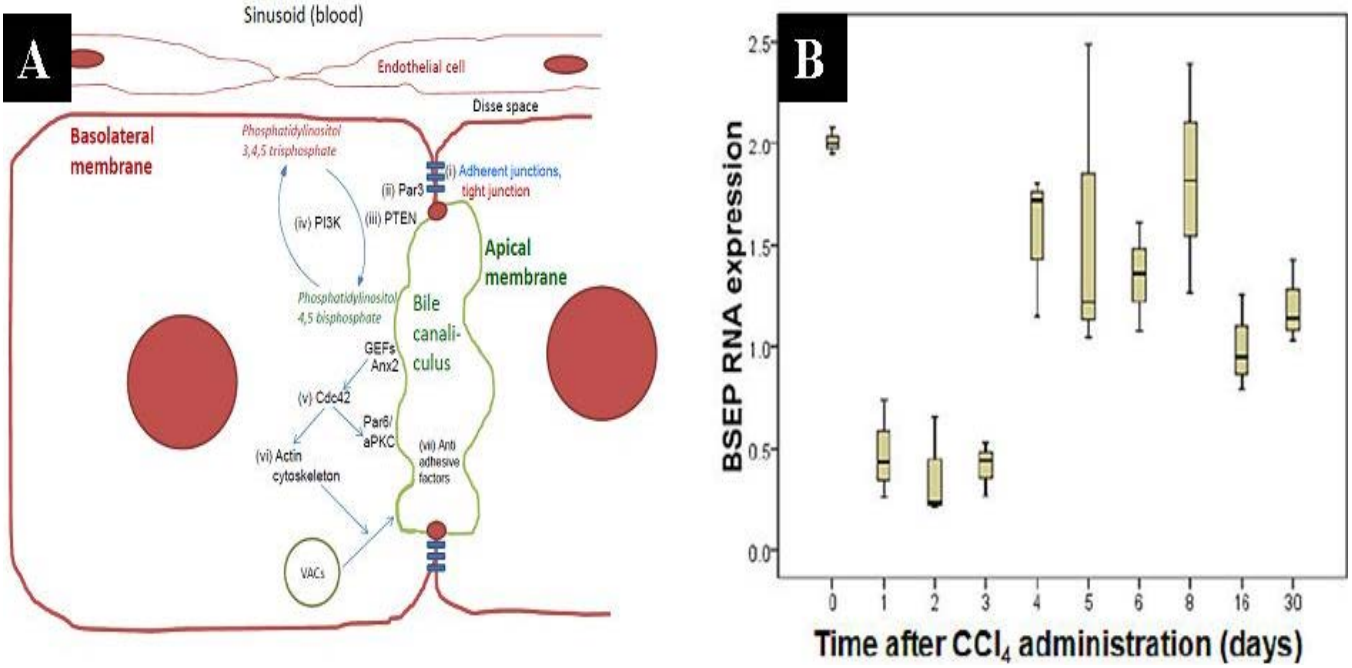

Figure 6.1. Establishment of hepatocellular polarity. A) Steps of cell polarity establishment were described by (Martin-Belmonte and Mostov, 2008; Hoehme et al., 2012). B) The mRNA level of bile sort export pump (BSEP) was down regulated transiently after carbon tetrachloride intoxication (Hoehme et al., 2010).

To understand if hepatocyte polarity is maintained or given up during cell division, I analyzed dividing hepatocytes in mouse livers after intoxication. For this purpose, mice were exposed to a single dose of carbon tetrachloride (Fig. 4.1). Before liver

preparation, mice were injected with three doses of BrdU to analyze S-phase hepatocytes. To test whether the hepatocellular polarity is transiently lost (Lecuit and Lenne, 2007; Hoehme et al., 2010) or maintained during the regeneration process, the liver tissues were costained with antibodies directed against BrdU with different markers directed against basolateral and apical poles as well as tight junction. The results showed that hepatocytes maintained basolateral domains (E-cadherin, LDLR and Beta-catenin) and apical domains (Mrp2, DPPIV/CD26 and radixin), as well as tight junction protein (claudin1) during S-phase and mitosis (Fig. 5.16; Fig. 5.17; Fig. 5.18; Fig. 5.19; Fig. 5.20). This result suggests that the proliferating hepatocytes are able to maintain functions e.g. bile forming capacities, also in actively dividing cells. Interestingly, these results did not correspond to the mRNA level of the bile sort export pump (BSEP) which decreased transiently after carbon tetrachloride intoxication (Fig. 6.1.B; Hoehme et al., 2010 supplemental data). When hepatocytes divide, a novel apical domain and bile canalicular branch have to be established between the daughter hepatocytes. To analyze this process, a pulse chase experiment was performed (Fig. 4.2). Careful analysis of the immunostained liver sections revealed that the liver micro-architecture was completely restored on day three after BrdU administration. Most of the BrdU positive hepatocytes went through the cell cycle towards the M-phase between 6 and 8 hours after BrdU injection. During this period the proliferating hepatocytes maintained the apical domains (Fig. 5.21; Fig. 6.2). At the late stage of mitosis, the bile canalicular belt invaginated toward the center between the daughter hepatocytes to fill the cleavage furrow. Subsequently, this invaginated domain extended between the daughter hepatocytes. Finally, a novel bile canalicular branch is established between the daughter hepatocytes. Restoration of the hepatic micro-architecture requires the following steps: i) the proliferating hepatocytes to remain polarized (Fig. 5.16; Fig. 5.17; Fig. 5.19; Fig. 5.20); ii) the daughter hepatocytes to align to the closest hepatic sinusoid (Hoehme et al., 2010); iii) the apical domains to establish between the daughters immediately after mitosis; and iv) the existing bile canaliculus to invaginate between the daughter

hepatocytes to establish a novel branch in addition to the existing bile canalicular network (Fig. 5.21). Figure 6.2 shows the different steps required for establishment of the new apical domain between the daughter cells.

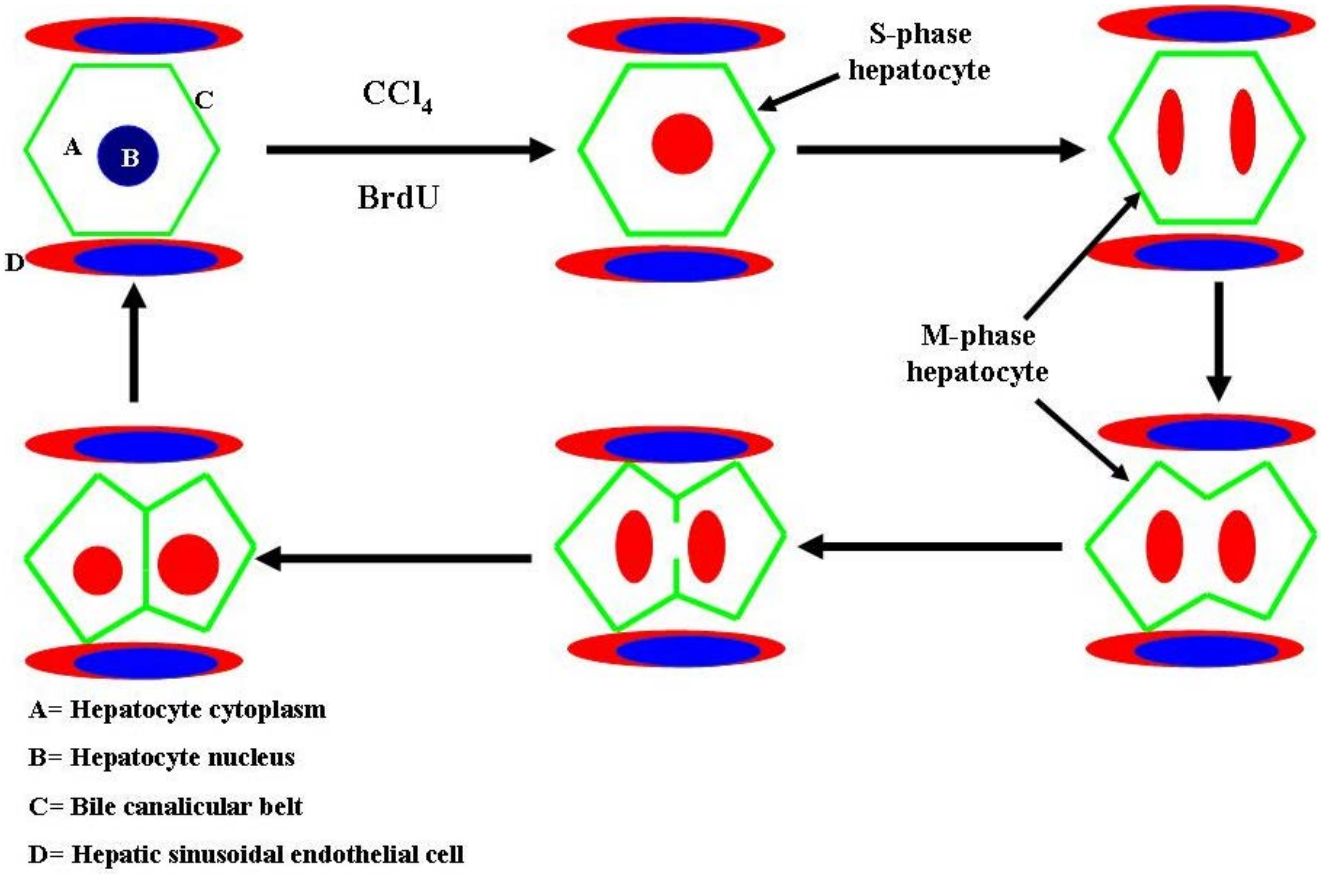

Figure 6.2. Establishment of a novel apical domain and bile canaliculus between the daughter hepatocytes. The schedule shows that a hepatocyte is surrounded by a belt of bile canaliculi. During both S- and M-phases, the hepatocyte preserves the bile canaliculi with neighboring cells. At the late stage of mitosis, one branch of the already existing network invaginates to fill the cleavage furrow. Subsequently, a branch of bile canaliculi is extended and connected to the network. The corresponding real reconstructions are shown in figure 5.21.

6.4. Reconstruction of the bile canalicular network during the intoxication, regeneration and fibrosis processes

Studies on the complex molecular mechanism controlling hepatocyte polarity, together with the polarity of other mammalian cells other than hepatocytes have been difficult largely because of technical obstacles (Wang and Bayer, 2004). One limitation is that it

was not yet possible to quantitatively separate apical and basolateral membranes for an unbiased analysis of the proteome and lipidome during the process of cell polarity establishment. This limitation leads to a shortage of detailed explanations of the bile canalicular network in reviews and textbooks. Hans Elias (Elias, 1949) described the relationship between the hepatocyte shapes and the bile canalicular network (Fig. 2.3A). Hansen and Koepen (2002) described a belt of bile canaliculi as one hexagon (Fig. 2.3B). To bridge this gap and to better understand the architecture of the bile canalicular network, a method for analyzing three dimensional organizations of the bile canaliculi and hepatic sinusoids using confocal images was established. The careful analysis of the reconstructed data sets of the healthy mice meant that I could detect some basic structures of the biliary network including 1) the bile canaliculi form three half-hexagonal belts around the hepatocytes; 2) two classes of bile canaliculi; 3) three hepatocytes surrounding one sinusoid form a frequently observed basic building block; 4) hepatic sinusoids surrounded by a hexagonal belt of bile canaliculi; 5) unconnected branches of the bile canalicular network (dead ends) and 6) bile canaliculi are located mainly at center of lateral surface. The mentioned basic structures will be discussed in the following paragraphs:

1) Three half-hexagonal belts of bile canaliculi around the hepatocytes are observed. Two of these belts are connected frequently to form a complete hexagon (Fig. 5.23 and Fig. 6.3A).

2) Two classes of bile canaliculi can be differentiated according to their alignment to the corresponding hepatic sinusoid. The first class of bile canaliculi (Fig. 6.3C, white line) was parallel to the hepatic sinusoid (Fig. 5.24 and Fig. 6.3C). It serves as a bile collector and drainer from the corresponding hepatocytes toward the bile duct. The second class of bile canaliculi (Fig. 6.3C, white line) was perpendicular to the hepatic sinusoid. The

main function of the second class is to collect the bile from the corresponding hepatocytes, which is then drained into the first class of bile canaliculi.

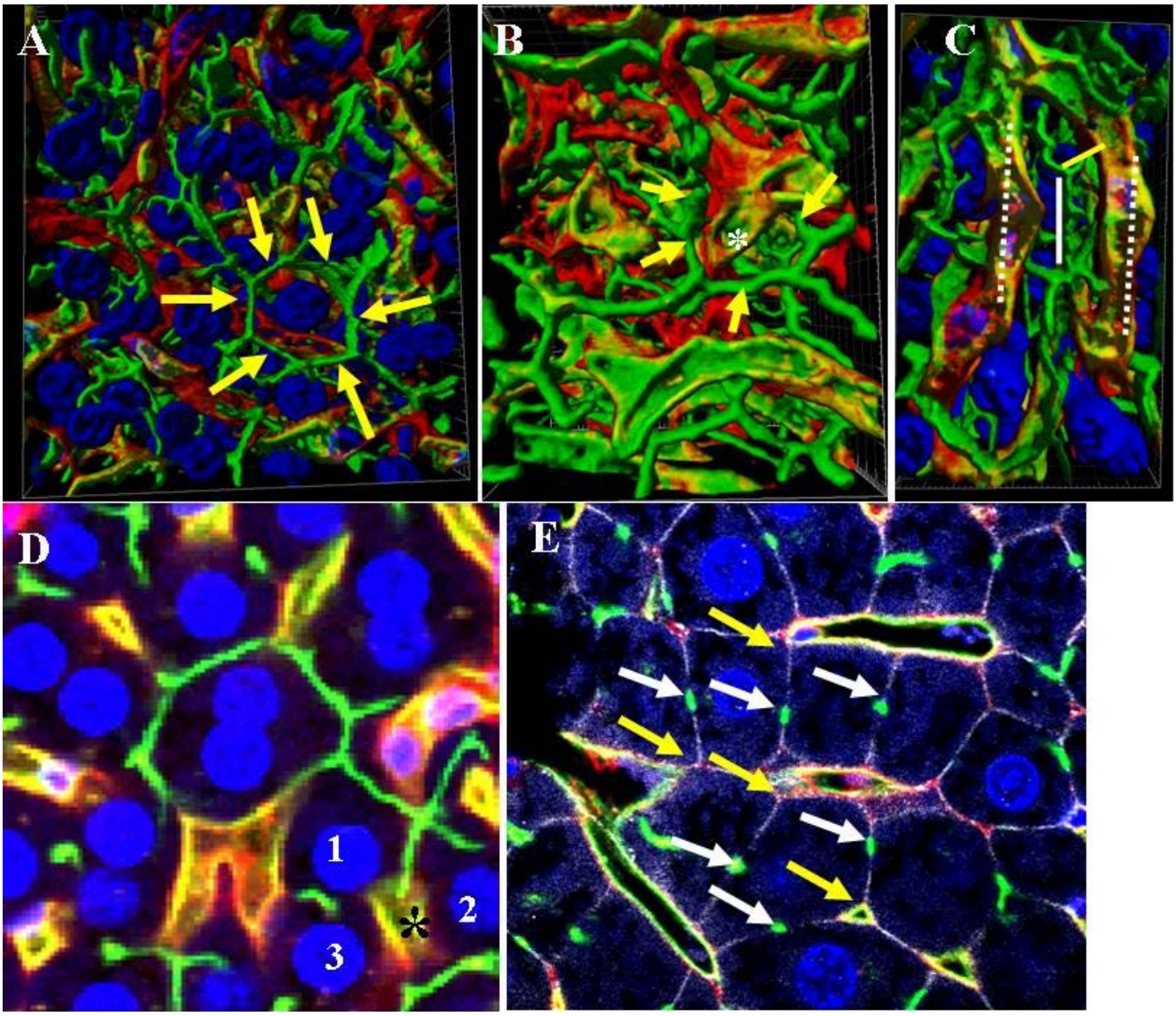

Figure 6.3. Some basic structures of the bile canalicular network. A) Mononucleated hepatocyte is surrounded by a hexagonal belt of bile canaliculi (yellow arrows). B) A hepatic sinusoid (white asterisk) surrounded by a ring of bile canaliculi (yellow arrows). C) There are two classes of bile canaliculi based on their orientation to the sinusoid. The first class is parallel (white line) and second class is perpendicular (yellow line) to the sinusoid (dashed lines). D) Most of hepatic sinusoids (black asterisk) are surrounded by three hepatocytes (named 1, 2 and 3). E) Bile canaliculi (white arrows) are located

mainly at center of lateral surface not at the corner (yellow arrows) as previously thought.

3) Most of hepatic sinusoids surrounded by three hepatocytes. This basic building unit is composed of one hepatic sinusoid (Fig. 5.25 and Fig. 6.3D, black asterisk) surrounded by three hepatocytes (Fig. 6.3D) on different levels.

4) Hepatic sinusoids are surrounded by a hexagonal belt of bile canaliculi (Fig. 5.26 and Fig. 6.3B, white asterisk). The bile canaliculi formed complete or incomplete polygonal belts around the hepatic sinusoids (Fig. 5.26 and Fig. 6.3B, yellow arrows). These bile canalicular belts are composed of the second classes surrounding the hepatocytes.

5) Unconnected branches of the bile canalicular network 'dead ends'. Several unconnected (connected only from one side) branches of the bile canalicular network (Fig. 5.28A and B) are present. These branches had normal bile canalicular morphology and varied in length. The existence of dead ends is interpreted as a way to increase the surface area of the bile canalicular network.

6) Bile canaliculi are located mainly at the center of lateral surface. It seems to be that the bile canaliculus is located at the center of the lateral surface (Fig. 6.3E white arrows and Fig. 6.4D, white arrows) and not at the corner as previously thought (Fig. 6.3E yellow arrows and Fig. 6.4D, yellow arrows). Therefore, in most cases the hepatocyte is surrounded by three hepatic sinusoids and three-half belts of bile canaliculi.

7) Idealized design. An idealized hepatocyte including the half-hexagonal belts and the sinusoids was built using AutoCAD software. The hepatocyte contained three half-hexagonal belts of bile canaliculi and is surrounded by three hepatic sinusoids. The cell shape presented in this design represents a theoretical assumption and was not derived from Z-stacks. In this design, (Fig. 6.4A, B and C) the hepatocytes are polygonal cells. Basal, lateral and apical membranes were visualized facing the hepatic sinusoids,

neighboring hepatocytes and bile canaliculi, respectively. The bile canaliculi are curved to connect two cells. The curvation angle was approximately 109°. This idealized version was in agreement with several observations e.g., hepatocytes are polygonal objects, the bile canaliculi form three halves belt around the hepatocyte, the hepatic sinusoid is surrounded by a belt of bile canaliculi, as well as existence of primary and secondary classes.

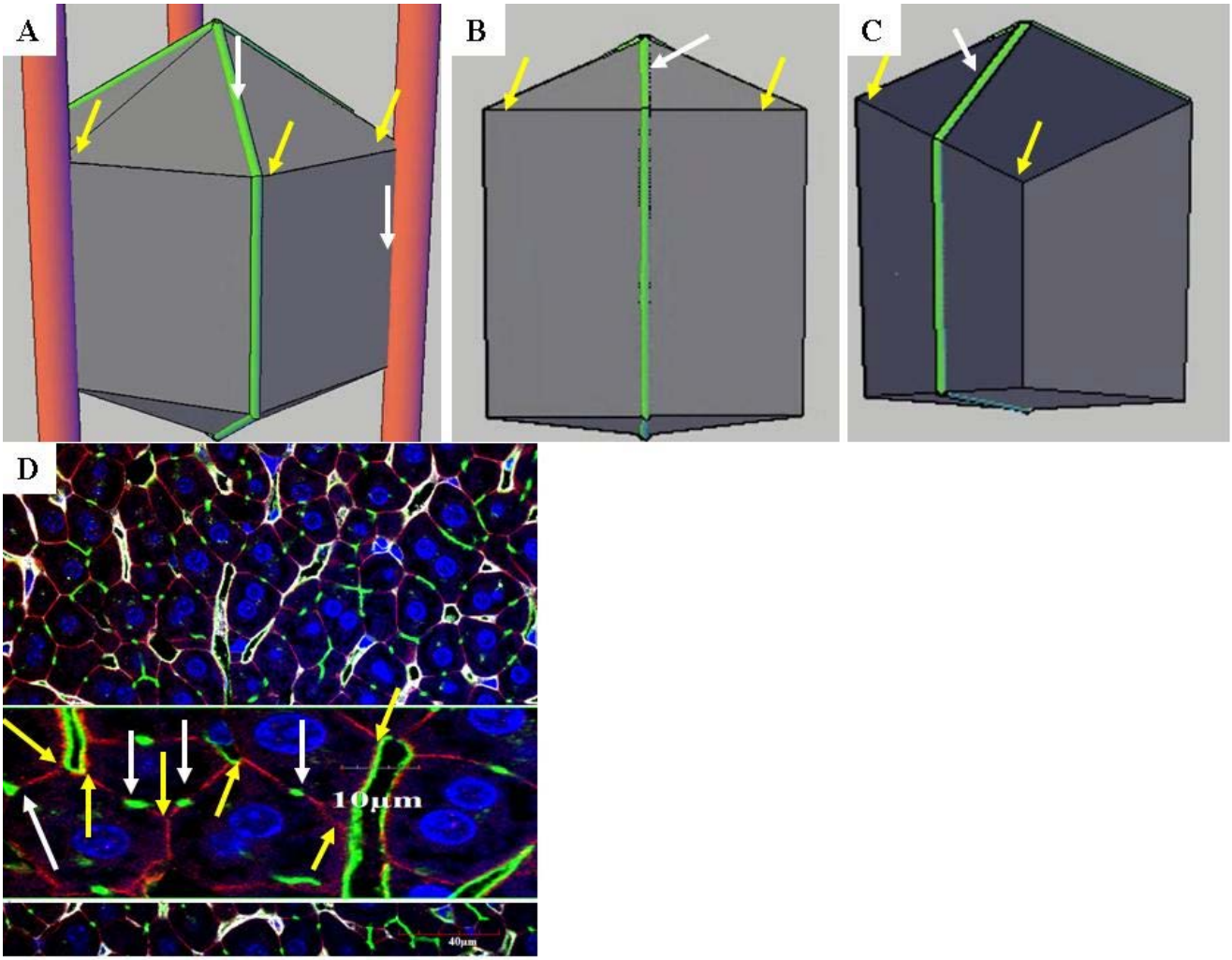

Figure 6.4. Bile canaliculi are located mainly at the center of lateral surface. One cell based model consisted of black polygonal object (hepatocyte), three red cylinder (hepatic sinusoid) and the green connected tubes (bile canaliculi) are designed using AutoCAD software. A) The bile canaliculi (white arrows) are located at the corners (yellow arrows) of the hepatocyte. B and C) The bile canaliculi (white arrows) are located at the center of the lateral

surface (yellow arrows). D and E) Bile canaliculi (white arrows) are located mainly at center of lateral surface not at the corner (yellow arrows) as previously thought.

Reconstruction of the bile canalicular network during intoxication, regeneration and fibrosis processes

In case of liver intoxication and regeneration processes, the centrilobular damaged areas revealed that the bile canaliculi were dramatically altered. The reconstructed dataset on day two (maximal damage time) after carbon tetrachloride injection indicated the presence of intact hepatic sinusoid and disappearance of the bile network. Qualitatively, there is a clear increase in the number of unconnected branches of bile canalicular network. One interpretation for this increase is a compensatory functional mechanism due to massive loss of the hepatocytes. Another interpretation might be that the unconnected branches fill the cleavage between the daughter hepatocytes (Fig. 5.28). Similarly, this observation (increase number of unconnected branches of bile canaliculi) was also recorded in the fibrotic livers.

7. Summary

The liver contains two networks: 1) the microvessels network also named liver sinusoids and 2) the bile canalicular network. The disruption of the bile canalicular network leads to improper bile flow, cholestasis and toxicity of the liver cells. Relatively little is known about the organization of the bile canalicular network in healthy livers and it is not completely described after liver intoxication, regeneration and fibrosis processes. Therefore, the goals of the present study are to: i) establish a mouse model of acute hepatoxicity by carbon tetrachloride injection; ii) determine the maintenance and establishment of hepatocellular polarity during the intoxication and regeneration processes; and iii) reconstruct the bile canalicular network of the normal, intoxicated and regenerated as well as fibrotic mouse livers. In the present study, I used carbon tetrachloride as a well accepted model for liver cell destruction, intoxication and fibrosis induction. The obtained results describing the liver intoxication and regeneration process were in agreement with published data. Therefore, the liver tissue after acute and chronic administration of carbon tetrachloride could be used to analyze the bile canalicular network under conditions of acute liver damage and fibrosis. The steps of the normal hepatic micro-architecture restoration after liver intoxication could be summarized as follows: i) the proliferating hepatocytes maintained their polarity; ii) the daughter hepatocytes are aligned in the direction of the closest microvessels; and iii) the existing bile canaliculus is invaginated between the daughter hepatocytes to establish a novel branch. Currently, there is no technique available to quantify the bile canalicular network. Therefore, to understand the architecture of the bile canalicular network and to bridge this gap, a method for analyzing three dimensional organization of the bile canaliculi and hepatic sinusoids was established using confocal microscopy and image analysis. Based on the reconstructed data sets of the healthy mice, I could detect some basic structures of the bile canalicular network including: 1) the bile canaliculi form three half-hexagonal belts around the hepatocytes. Two halves are connected to form a

belt and third half sometimes is connected to the belt or formed an unconnected branch; 2) two classes of bile canaliculi could be differentiated. Whereby canaliculi of first class are oriented in parallel to the closest sinusoid and the second class of bile canaliculi are perpendicular to the sinusoid; 3) three hepatocytes surrounding one sinusoid form a frequently observed basic building block; 4) hepatic sinusoids are surrounded by a hexagonal belt of bile canaliculi; 5) unconnected branches of the bile canalicular network 'dead ends' were observed; and 6) bile canaliculi are located mainly at the center of the lateral surface or very rarely at the edges of the hepatocyte surface. The disruption of the bile canalicular network was recorded in injured livers. This disruption includes disappearance of the network in damaged areas (necrotic and fibrotic) and an increase in the number of the unconnected branches in the surviving tissue. A 'fish bone' appearance was also frequently recorded in the tissue with the surviving hepatocytes. The current study demonstrates that the architecture of the bile canalicular network clearly differs from the way it is presented in textbooks. It represents a low order network but some basic features and building principles are maintained all over the tissue. Liver damage induces a tightly controlled sequence of events by which the bile canalicular network is reconstructed.

7. Zusammenfassung

Die Leber besteht aus zwei unabhängigen Netzwerken: 1) dem Mikrogefäßnetzwerk, Sinusiodalnetzwerk genannt und 2) einem Netzwerk von Gallengängchen. Beeinträchtigungen am Gallengangnetzwerk führen zu Cholestase und zur Schädigung von Leberzellen. Über die Organisation des Gallengangnetzwerks in der Leber ist bisher wenig bekannt und ist nur zu Teilen für Vergiftung, Regeneration und Fibrose beschrieben. Das Ziel dieser Arbeit ist es i) ein Modell der akuten Tetrachlorkohlenstoffvergiftung zu erstellen, ii) die Erhaltung bzw. den Neuaufbau der Leberzellenpolarität während der Lebervergiftung und der Regeneration zu untersuchen und iii) eine Rekonstruktion des Gallengangnetzwerks der gesunden, vergifteten und regenerierenden Mausleber zu erstellen. In dieser Arbeit verwendete ich Tetrachlorkohlenstoff als Lebertoxin. Dieses Modell ist gut verstanden und akzeptiert zur Untersuchung von Leberzelltod, Vergiftung und Leberfibrose. Die erhaltenen Daten bestätigen die bereits publizierten Ergebnisse, so dass die gewonnenen Gewebeproben von akuter und langzeitbehandelter Leber zur Analyse des Gallengangnetzwerks in geschädigter und fibrotischer Leber gebraucht werden konnten. Die Schritte der Wiederherstellung der normalen Lebermikroarchitektur können wie folgt zusammengefasst werden: i) die proliferierenden Zellen behalten die Zellpolarität bei, ii) Tochterzellen richten sich an den anliegenden Sinusoidzellen aus und iii) aus bereits bestehenden Gallengängen werden neue zwischen die Tochterhepatozyten getrieben, um weitere Zweige auszubilden. Bis heute gibt es noch keine Möglichkeit zur Quantifizierung des Gallengangnetzwerk. Zum besseren Verständnis des Netzwerks wurde eine Methode zur Analyse der dreidimensionalen Organisation des Gallengang- und des sinusoidalen Netzwerks mit Hilfe von konfokaler Mikroskopie und Bildverarbeitung entwickelt. Basierend auf den gemessenen Datensätzen von gesunden Mäusen konnte ich einige grundlegende Strukturen des Netzwerks finden: 1) die Gallengängchen bilden drei halbhexagonale Gürtel um die Hepatozyte. Zwei Halbe sind

miteinander verbunden und bilden einen Gürtel und der dritte Halbe kann ebenfalls verbunden sein oder aber auch ein Sackgassenende ausbilden; 2) es können zwei Klassen von Gallengängen unterschieden werden. Wobei Gallengänge der ersten Klasse sich parallel am angrenzenden Sinusoid ausrichten, im Gegensatz dazu aber die Gallengänge der zweiten Klasse sich senkrecht dazu erstrecken; 3) drei Hepatozyten, die einen Sinusoid umgeben bildet eine oft vorgefunden Grundstruktur; 4) Sinusoide sind von einem hexagonalen Gürtel aus Gallengängchen umgeben; 5) es existieren freie Enden im Gallengangnetzwerk - ‚dead ends'; und 6) Gallengängchen befinden sich hauptsächlich in der Mitte der flachen Seite der Hepatozyte, nur sehr selten sind sie entlang der Kante der Hepatozyte zu finden. Die Zerstörung des Gallengangnetzwerks wurde in Tetrachlorkohlenstoff geschädigter Leber untersucht. Diese Zerstörung zeigt sowohl ein Verschwinden des Netzwerks in den geschädigten Arealen (nekrotisch und fibrotisch), als auch eine vermehrte Anzahl an freien Enden der Gängchen in den gesunden Arealen. Das Gallengangnetzwerk im angrenzenden gesundeten Gewebe zeichnete sich häufig durch ein fischgrätenartiges Muster aus. Diese Studie zeigt, dass die Architektur der Gallengänge sich von den gängigen Beschreibungen in Lehrbüchern unterscheidet. Es handelt sich um ein Netzwerk von geringer Ordnung, aber mit einigen grundlegenden Mustern und Aufbauprinzipien des Gewebes. Leberschädigung löst einen streng regulierten Regenerationsmechanismus aus, der zur Wiederherstellung des Gallengangsystems führt.

8. References

Alhassan AJ, Sule MS, Aliyu SA and Aliyu MD (2009)

Ideal hepatotoxicity model in rats using carbon tetrachloride (CCl_4).

Bayero journal of pure and applied sciences, volume 2(2), pages: 185-187.

Bacon BR, O'Grady JG, Di Bisceglie AM and Lake JR (2006)

Comprehensive clinical hepatology.

Mosby publisher, second edition, printed in China.

Bataller R and Brenner DA (2005)

Liver fibrosis.

Journal of clinical investigation, volume 115(2), pages: 209-218.

Benedetti A, Fulceri R, Ferrali M, Ciccoli L, Esterbauer H and Comporti M (1982)

Detection of carbonyl functions in phospholipids of liver microsomes in CCl_4- and BrCCl3-posioned rats.

Biochimica biophysica acta, volume 712(3), pages: 628-638.

Boehm F, Koehler UA, Speicher T and Werner S (2010)

Regulation of liver regeneration by growth factors and cytokines.

EMBO Molecular medicine, volume 2(8), pages: 294-305.

Boyer TD, Wright TL and Manns MP (2006)

Zakim and Boyer's hepatology: A textbook of liver disease.

Saunders, Elsevier Inc, volume 1, fifth edition, printed in Canada.

Braet F and Wisse E (2002)

Structural and functional aspects of liver sinusoidal endothelial cell fenestrae: a review.

Comparative hepatology, volume 1(1):1.

Braeuning A, Singh Y, Rignall B, Buchmann A, Hammad S, Othman A, von Recklinghausen I, Godoy P, Hoehme S, Drasdo D, Hengstler JG and Schwarz M (2010)

Phenotype and growth behavior of residual β-catenin positive hepatocytes in livers of β-catenin-deficient mice.

Histochemistry and cell biology, volume 134(5), pages: 469-481.

Cadoret A, Ovejero C, Terris B, Souil E, Lévy L, Lamers WH, Kitajewski J, Kahn A and Perret C (2002)

New targets of βeta-catenin signaling in the liver are involved in the glutamine metabolism.

Oncogene, volume 21(54), pages: 8293-8301

Cano A, Perez-Moreno MA, Rodrigo I, Locascio A, Blanco MJ, del Barrio MG, Portillo F and Nieto MA (2000)

The transcription factor Snail controls epithelial-mesenchymal transitions by repressing E-cadherin expression.

Nature cell biology, volume 2(2), pages: 76-83.

Chobert MN, Couchie D, Fourcot A, Zafrani ES, Laperche Y, Mavier P and Brouillet A (2012)

Liver precursor cells increase hepatic fibrosis induced by chronic carbon tetrachloride intoxication in rats.

Laboratory investigation, volume 92(1), pages: 135-150.

Cook MJ (1965)

The Anatomy of the Laboratory Mouse.

Academic press.

Cohen D, Brennwald PJ, Rodriguez-Boulan E and Muesch A (2004)

Mammalian PAR-1 determines epithelial lumen polarity by organizing the microtubule cytoskeleton.

The journal of cell biology, volume 164(5), pages: 717-727.

Constandinou C, Henderson N and Iredale JP (2005)

Modeling liver fibrosis in rodents.

Methods in molecular medicine, volume 117(III), pages: 237-250.

Dalton SR, Lee SML, King RN, Nanji AA, Kharbanda KK, Casey CA and McVicker BL (2009)

Carbon tetrachloride-induced liver damage in asialoglycoprotein receptor-deficient mice.

Biochemical pharmacology, volume 77(7), pages: 1283-1290.

Decaens C, Durand M, Grosse B and Cassio D (2008)

Which in vitro models could be best used to study hepatocyte polarity?

Biology of the cell, volume 100(7), pages: 387-398.

Diaz Gómez MI, Fanelli SL, Delgado de Layño AM, Castro JA and Castro GD (2006)

Liver nuclear and microsomal CYP2E1-mediated metabolism of xenobiotics in rats chronically drinking an alcohol-containing liquid diet.

Toxicology and industrial health, volume 22(9), pages: 367-374.

Ding BS, Nolan DJ, Butler JM, James D, Babazadeh AO, Rosenwaks Z, Mittal V, Kobayashi H, Shido K, Lyden D, Sato TN, Rabbany SY and Rafii S (2010)

Inductive angiocrine signals from sinusoidal endothelium are required for liver regeneration.

Nature, volume 468 (7321), pages: 309-317.

Domenicali M, Caraceni P, Giannone F, Baldassarre M, Lucchetti G, Quarta C, Patti C, Catani L, Nanni C, Lemoli RM and Bernardi M (2009)

A novel model of CCl_4-induced cirrhosis with ascites in the mouse.

Journal of hepatology, volume 51(6), pages: 991-999.

Dorn C, Heilmann J and Hellerbrand C (2012)

Protective effect of xanthohumol on toxin-induced liver inflammation and fibrosis.

International journal of clinical and experimental pathology, volume 5(1), pages: 29-36.

Dufour JF and Clavien PA (2005)

Signaling pathways in liver diseases.

Springer-Verlag Berlin Heidelberg, printed in Germany.

Elias H (1949)

A re-examination of the structure of the mammalian liver: II. The hepatic lobule and its relation to the vascular and biliary systems.

American journal of anatomy, volume 85 (3), pages: 379-456.

Fausto N and Riehle KJ (2005)

Mechanisms of liver regeneration and their clinical implications.

Journal of hepato-biliary-pancreatic surgery, volume 12(3), pages: 181-189.

Fickert P, Zollner G, Fuchsbichler A, Stumptner C, Pojer C, Zenz R, Lammert F, Stieger B, Meier PJ, Zatloukal K, Denk H, and Trauner M (2001)

Effects of ursodeoxycholic and cholic acid feeding on hepatocellular transporter expression in mouse liver**.**

Gastroenterology, volume 121(1), pages: 170-183.

Friedman SL (2008)

Hepatic fibrosis-Overview.

Toxicology, volume 254(3), pages: 120-129.

Fujii T, Fuchs BC, Yamada S, Lauwers GY, Kulu Y, Goodwin JM, Lanuti M and Tanabe KK (2010)

Mouse model of carbon tetrachloride induced liver fibrosis: Histopathological changes and expression of CD133 and epidermal growth factor.

BMC Gastroenterology, volume 10, pages: 79-90.

Gebhardt R (1992)

Metabolic zonation of the liver: Regulation and implications for liver function.

Pharmacology & Therapeutics, volume 53(3), pages: 275-354.

Geerts A (2001)

History, heterogeneity, developmental biology and functions of quiescent hepatic stellate cells.

Seminars in liver disease, volume 21(3), pages: 311-335.

Godoy P, Lakkapamu S, Schug M, Bauer A, Stewart JD, Bedawi E, Hammad S, Amin J, Marchan R, Schormann W, Maccoux L, Recklinghausen I, Reif R and Hengstler JG (2010)

Dexamethasone-dependent versus -independent markers of epithelial to mesenchymal transition in primary hepatocytes.

Biological chemistry, volume 391(1), pages: 73-83.

Gunawan BK, Liu ZX, Han D, Hanawa N, Gaarde WA and Kaplowitz N (2006)

c-Jun N-terminal kinase plays a major role in murine acetaminophen hepatotoxicity.

Gastroenterology, volume 131(1), pages: 165-178.

Handler JS (1989)

Overview of epithelial polarity.

Annual review of physiology, volume 51, pages: 729-740.

Hansen JT and Koeppen (2002)

Netter's Atlas of Human physiology (Netter´s basic science).

Saunders, first edition, printed in USA.

Hoehme S, Hengstler JG, Brulport M, Schaefer M, Bauer A, Gebhardt R and Drasdo D (2007)

Mathematical modelling of liver regeneration after intoxication with CCl_4.

Chemico-biological interactions, volume 168(1), pages: 74-93.

Hoehme S, Brulport M, Bauer A, Bedawy E, Schormann W, Gebhardt R, Zellmer S, Schwarz M, Bockamp E, Timmel T, Hengstler JG and Drasdo D (2010)

Prediction and validation of cell alignment along microvessels as order principle to restore tissue architecture in liver regeneration.

Proceedings of the national academy of sciences, volume 107(23), pages: 10371-10376.

Hoehme S, Schwen LO, D'Alessandro LA, Friebel A, Neitsch J, Raue A, Rho SH, Gremse F, von Recklinghausen I, Hammad S, Ghallab A, Godoy P, Reif R, Kiessling F, Timmer J, Preusser T, Hengstler J, Klingmueller U and Drasdo D (2012)

Multiscale modeling of liver regeneration.

Manuscript in preparation.

Hong WJ, Petell JK, Swank D, Sanford J, Hixson DC and Doyle D (1989)

Expression of dipeptidyl peptidase IV in rat tissues is mainly regulated at the mRNA levels.

Experimental cell research, volume 182(1), pages: 256-266.

Jeong WI, Park O, Radaeva S and Gao B (2006)

STAT1 inhibits liver fibrosis in mice by inhibiting stellate cell proliferation and stimulating NK cell cytotoxicity.

Hepatology, volume 44(6), pages: 1441-1451.

Joseph B, Kumaran V, Berishvili E, Bhargava KK, Palestro CJ and Gupta S (2006)

Monocrotaline promotes transplanted cell engraftment and advances liver repopulation in rats via liver conditioning.

Hepatology, volume 44(6), pages: 1411-1420.

Junqueira LCU, Bignolas G, Brentani RR (1979)

Picrosirius staining plus polarization microscopy, a specific method for collagen detection in tissue sections.

The histochemical journal, volume 11(4), pages: 447-55

Katz NR (1992)

Metabolic heterogeneity of hepatocytes across the liver acinus.

Journal of nutrition, volume 122(3), pages: 843-849.

Koniaris LG, McKillop IH, Schwartz SI and Zimmers TA (2003)

Liver regeneration.

Journal of the American College of Surgeons, volume 197(4), pages: 634-659.

Krizhanovsky V, Yon M, Dickins RA, Hearn S, Simon J, Miething C, Yee H, Zender L and Lowe SW (2008)

Senescence of activated stellate cells limits liver fibrosis.

Cell, volume 134(4), pages: 657-667.

Kuntz E and Kuntz HD (2008)

Hepatology: Textbook and atlas.

Springer Medizin Verlag, Heidelburg, third edition, printed in Germany.

Kuo FC and Darnell JE (1991)

Evidence that interaction of hepatocytes with the collecting (hepatic) veins triggers position-specific transcription of the glutamine synthetase and ornithine aminotransferase genes in the mouse liver.

Molecular and cellular biology, volume 11(12), pages: 6050-6058.

Lecuit T and Lenne PF (2007)

Cell surface mechanics and the control of cell shape, tissue patterns and morphogenesis.

Nature reviews. Molecular cell biology, volume 8(8), pages: 633-644.

Lee PY, McCay PB and Hornbrook KR (1982)

Evidence for carbon tetrachloride-induced lipid peroxidation in mouse liver.

Biochemical pharmacology, volume 31(3), pages: 405-409.

Li FC, Huang GT, Lin CJ, Wang SS, Sun TL, Lo SY, Lo W, Chiou LL, Dong CY and Lee HS (2011)

Apical membrane rupture and backward bile flooding in acetaminophen-induced hepatocyte necrosis.

Cell death and disease volume 2, pages: e183-e191.

Link B, Duerk H, Thiel D and Frank H (1984)

Binding of trichloromethyl radicals to lipids of the hepatic endoplasmic reticulum during tetrachloromethane metabolism.

The biochemistry journal, volume 223(3), pages: 577-586.

Loeppen S, Schneider D, Gaunitz F, Gebhardt R, Kurek R, Buchmann A and Schwarz M (2002)

Overexpression of glutamine synthetase is associated with beta-catenin-mutations in mouse liver tumors during promotion of hepatocarcinogenesis by phenobarbital.

Cancer research, volume 62(20), pages: 5685-5688.

Ludwig J, Ritman EL, LaRusso NF, Sheedy PF and Zumpe G (1998)

Anatomy of the human biliary system studied by quantitative computer-aided three-dimensional imaging techniques.

Hepatology, volume 27(4), pages: 893-899.

Manibusan MK, Odin M and Eastmond DA (2007)

Postulated carbon tetrachloride mode of action: A review.

Journal of environmental science and health part C, volume 25(3), pages: 185-209.

Martin-Belmonte F and Mostov K (2008)

Regulation of cell polarity during epithelial morphogenesis.

Current opinion in cell biology, volume 20(2), pages: 227-234.

Martins PN, Theruvath TP and Neuhaus P (2008)

Rodent models of partial hepatectomies.

Liver international, volume 28(1), pages: 3-11.

Matsumoto T and Kawakami M (1982)

The unit-concept of hepatic parenchyma--a re-examination based on angioarchitectural studies.

Acta patholgica Japonica, volume 32(2), pages: 285-314.

McCaffrey LM and Macara IG (2009)

Widely conserved signaling pathways in the establishment of cell polarity.

Cold spring harbor perspectives in biology, volume 1(2), page: a001370.

McCuskey R (2008)

The hepatic microvascular system in health and its response to toxicants.

Anatomical record, volume 291(6), pages: 661-671.

Michalopoulos GK and DeFrances MC (1997)

Liver regeneration.

Science, volume 276(5309), pages: 60-66.

Michalopoulos GK and Khan Z (2005)

Liver regeneration, growth factors and amphiregulin.

Gastroenterology, volume 128(2), pages: 503-506.

Michalopoulos GK (2007)

Liver regeneration. Review.

Journal of cellular physiology, volume 213(2), pages: 286-300.

Mico BA and Pohl LR (1983)

Reductive oxygenation of carbon tetrachloride: Trichloromethylperoxyl radical as a possible intermediate in the conversion of carbon tetrachloride to electrophilic chlorine.

Archives of biochemistry and biophysics, volume 225(2), pages: 596-609.

Panbianco C and Gotta M (2011)

Coordinating cell polarity with cell division in space and time.

Trends in cell biology, volume 21(11), pages: 672-680.

Perez Tamayo R (1983)

Is cirrhosis of the liver experimentally produced by CCl_4 an adequate model of human cirrhosis?

Hepatology, volume 3(1), pages: 112-120.

Ponfick VA (1890)

Ueber Leberresection und Leberreaction.

Verhandl Deutsch Gesellsch Chir;19:28.

Poyer JL, McCay PB, Lai EK, Janzen EG and Davis ER (1980)

Confirmation of assignment of the trichloromethyl radical spin adduct detected by spin trapping during 13C-carbon tetrachloride metabolism in vitro and in vivo.

Biochemical and biophysical research communications, volume 94(4), pages: 1154-1160.

Radaeva S, Sun R, Jaruga B, Nguyen VT, Tian Z and Gao B (2006)

Natural killer cells ameliorate liver fibrosis by killing activated stellate cells in NKG2D-dependent and tumor necrosis factor-related apoptosis-inducing ligand-dependent manners.

Gastroenterology, volume 130(2), pages: 435-452.

Rappaport AM (1973)

The microcirculatory hepatic unit.

Microvascular research, volume 6(2), pages: 212-228.

Raucy JL and Carpenter SJ (1993)

The expression of xenobiotic-metabolizing cytochromes P450 in fetal tissues.

Journal of pharmacology and toxicological methods, volume 29(3), pages: 121-128.

Rodriguez-Boulan E and Powell SK (1992)

Polarity of epithelial and neuronal cells.

Annual review of cell biology, volume 8, pages: 395-427.

Sahu SC (2007)

Hepatotoxicity: From genomics to in vitro and in vivo models.

John Wiley & Sons Ltd, printed in England.

Saile B, Matthes N, Neubauer K, Eisenbach C, El-Armouche H, Dudas J and Ramadori G (2002)

Rat liver myofibroblasts and hepatic stellate cells differ in CD95-mediated apoptosis and response to TNF-α.

American journal of physiology. Gastrointestinal and liver physiology, volume 283(2), pages: G435-G444.

Schreiber S, Rignall B, Braeuning A, Marx-Stoelting P, Ott T, Buchmann A, Hammad S, Hengstler JG, Schwarz M and Koehle C (2011)

Phenotype of single hepatocytes expressing an activated version of β-catenin in liver of transgenic mice.

Journal of molecular histology, volume 42(5), pages: 393-400.

Shah H, Hartman SP and Weinhouse S (1979)

Formation of carbonyl chloride in carbon tetrachloride metabolism by rat liver in vitro.

Cancer research, volume 39(10), pages: 3942-3947.

Shi J, Aisaki K, Ikawa Y and Wake K (1998)

Evidence of hepatocyte apoptosis in rat liver after the administration of carbon tetrachloride.

American journal of pathology, volume 153, pages: 515-525.

Shivas JM, Morrison HA, Bilder D and Skop AR (2010)

Polarity and endocytosis: reciprocal regulation.

Trends in cell biology, volume 20(8), pages: 445-452.

Simons K and van Meer G (1988)

Lipid sorting in epithelial cells.

Biochemistry, volume 27(17), pages: 6197-6202.

Sakaida I, Terai S, Yamamoto N, Aoyama K, Ishikawa T, Nishina H and Okita K (2004)

Transplantation of bone marrow cells reduces CCl4-induced liver fibrosis in mice.

Hepatology, volume 40(6), pages: 1304-1311.

Slater TF and Sawyer BC (1970)

The hepatotoxic action of carbon tetrachloride stimulatory effect of carbon tetrachloride on lipid peroxidation in microsomal suspenions.

FEBS letters, volume 11(2), pages: 132-136.

Slater TF, Cheeseman KH and Ingold KU (1985)

Carbon tetrachloride toxicity as a model for studying free radical mediated liver injury.

Philosophical transactions of the royal society B: Biological sciences, volume 311(1152), pages: 633-645.

Stanciu A, Cotutiu C and Amalinei C (2002)

New data about ITO cells.

Rev Med Chir Soc Med Nat Iasi, volume 107(2), pages: 235-239.

Takasaki S and Hano H (2001)

Three dimensional observation of the human hepatic artery (arterial system in the liver).

Journal of hepatology, volume 34(3), pages: 455-466.

Teixeira-Clerc F, Julien B, Grenard P, Tran Van Nhieu J, Deveaux V, Li L, Serriere-Lanneau V, Ledent C, Mallat A and Lotersztajn S (2006)

CB1 cannabinoid receptor antagonism: a new strategy for the treatment of liver fibrosis.

Nature medicine, volume 12(6), pages: 671-676.

Tribble DL, Aw TY and Jones DP (1987)

The pathophysiological significance of lipid peroxidation in oxidative cell injury.

Hepatology, volume 7(2), pages: 377-387.

van Meer G and Simons K (1988)

Lipid polarity and sorting in epithelial cells.

Journal of cellular biochemistry, volume 36(1), pages: 51-58.

Villar D, Buck WB and Gonzalez JM (1998)

Ibuprofen, aspirin and acetaminophen toxicosis and treatment in dogs and cats.

Veterinary and human toxicology, volume 40(3), pages: 156-162.

Wang L and Boyer JL (2004)

The maintenance and generation of membrane polarity in hepatocytes.

Hepatology, volume 39(4), pages: 892-899.

Wang W, Soroka CJ, Mennone A, Rahner C, Harry K, Pypaert M and Boyer JL (2006)

Radixin is required to maintain apical canalicular membrane structure and function in rat hepatocytes.

Gastroenterology, volume 131(3), pages: 878-884.

Wang WB, Fan JM, Zhang XL, Xu J and Yao W (2009)

Serial expression analysis of liver regeneration-related genes in rat regenerating liver.

Molecular biotechnology, volume 43(3), pages: 221-231.

Wang EY, Yeh SH, Tsai TF, Huang HP, Jeng YM, Lin WH, Chen WC, Yeh KH, Chen PJ and Chen DS (2011)

Depletion of β-catenin from mature hepatocytes of mice promotes expansion of hepatic progenitor cells and tumor development.

Proceedings of the national academy of sciences, volume 108(45), pages: 18384-18389.

Weber LWD, Boll M and Stampfl A (2003)

Hepatotoxicity and mechanism of action of haloalkanes: Carbon tetrachloride as a toxicological model.

Critical reviews in toxicology, volume 33(2), pages: 105-136.

Wei H, Wei H, Wang H, Tian Z and Sun R (2010)

Activation of natural killer cells inhibits liver regeneration in toxin-induced liver injury model in mice via a tumor necrosis factor-α-dependent mechanism.

American journal of physiology. Gastrointestinal and liver physiology, volume 299(1), pages: G275-G282.

Wisse E (1970)

An electron microscopic study of the fenestrated endothelial lining of rat liver sinusoids.

Journal of ultrastructure research, volume 31(1-2), pages: 125-150.

Yamada Y and Fausto N (1998)

Deficient liver regeneration after carbon tetrachloride injury in mice lacking type 1 but not type 2 tumor necrosis factor receptor.

American journal of pathology, volume 152(6), pages: 1577-1589.

Zellmer S, Schmidt-Heck W, Godoy P, Weng H, Meyer C, Lehmann T, Sparna T, Schormann W, Hammad S, Kreutz C, Timmer J, von Weizsaecker F, Thürmann PA, Merfort I, Guthke R, Dooley S, Hengstler JG and Gebhardt R (2010):

Transcription factors ETF, E2F, and SP-1 are involved in cytokine-independent proliferation of murine hepatocytes.

Hepatology, volume 52(6), pages: 2127-2136.

Zhao DC, Lei JX, Chen R, Yu WH, Zhang XM, Li SN and Xiang P (2005)

Bone marrow-derived mesenchymal stem cells protect against experimental liver fibrosis in rats.

World journal of gastroenterology, volume 11(22), pages: 3431-3440.

9. Erklärung

Ich erkläre:

Ich habe die vorliegende Dissertation selbstständig, ohne unerlaubte fremde Hilfe und nur mit den Hilfen angefertigt, die ich in der Dissertation angegeben habe. Alle Textstellen, die wörtlich oder sinngemäß aus veröffentlichten oder nicht veröffentlichen Schriften entnommen sind, und alle Angeben die auf mündlichen Auskünften beruhen sind als solche kenntlich gemacht. Bei denen von mir durchgeführten und in der Dissertation beschriebenen Untersuchungen habe ich die Grundsätze guter wissenschaftlicher Praxis, wie sie in der „Satzung der Justus- Liebig-Universität Gießen zur Sicherung guter wissenschaftlicher Praxis“ niedergelegt sind, eingehalten.

Seddik Hammad

Acknowledgements

First of all I'm greatly indebted in my work to our merciful ''ALLAH''.

I want to thank Prof. Dr. Ernst Petzinger for his professional guidance and supervision throughout my work.

I would like to express my cardial gratitude and appreciation to Prof. Dr. Jan Hengstler for his guidance and helpful suggestions. Thanks for the critical observations and corrections. I learnt a lot from him during my study in Germany.

Tons of thanks to Prof. Dr. Abdel-Latif Shaker Seddik (Egyptian co-supervisor) for his professional supervision throughout my study.

Marks for very good assistance I received from my morphology team Dr. Iris vonRecklinghausen, Amnah Othman, Brigitte Begher-Tibbe and Martin Schmitz. I worked daily with this team. Many thanks for your help and encourage.

For motivating collaborations, helpful discussions and mathematical modeling I would like to acknowledge Dr. Dirk Drasdo, Dr. Stefan Hoehme, Adrian Friebel, Johannes Neitsch, William Weens, Nick Jagiella and Tim Johann.

Due acknowledgement also goes to Prof. Dr. Bruno Christ, Sandra Brueckner, Prof. Dr. Steven Dooley, Dr. Iryna Ilkavets and Dr. Bruno Stieger. They provided me the liver samples and uncommercial available antibodies.

Many thanks also to my colleagues Dr. Rosemarie Marchan and Dr. Joanna Stewart (for English correction), Dr. Raymond Reif (for helpful discussion and German translation), Prof. Dr. Klaus Golka and Dr. Marie-Louise Lehmann (for quite environment and advice), Dr. Silvia Seliniski (for statistical discussions), Dr. Cristina Cadenas, Dr. Patricio Godoy and Dr. Wolfram Foellman (for helpful discussion and critical suggestions).

Acknowledgements

==========

It was indeed a great opportunity and pleasure working in a system toxicology group at IfADo. Thanks Jakia Amin, Sonja Vossbeck, Dennis Frankenstein, Dr. Markus Schug, Dr. Wiebke Schormann and Regina Stoeber as well as the professional technical assistance received from Gerd Zimmermann.

I must acknowledge the official assistance and suggestions received from Silke Hankinson.

Many thanks to the Egyptian Government, the Ministry of High Education and Culture Affairs and the Mission Sector for funding me during my PhD study. I wish to express my thanks to my University (South valley university, Qena-Egypt) for allowing me to study and do research in Germany.

I would like to thank the virtual liver network (BMBF project) and Cancersys (EU-project) for allowing me to study and do my research within their frame.

I would like to thank my parents, brothers and sisters for their love and unending support over the course of my PhD and throughout my entire life.

Finally, I would like to thank my wife, vet. med. Amnah Othman, for her love and support. Thank you for encouraging me when the times were horrible. You mean the world to me and I could not have done this work without your encourage. Thanks to my daughters Hanen and Tasneem who sustained me a lot during this period.

This work is dedicated to my colleague 'Alexander Bauer', who passed away in 2009.

List of publications (peer-reviewed journals)

1. Schmidt M, Hellwig B, **Hammad S,** Othman A, Lohr M, Chen Z, Böhm D, Gebhard S, Petry IB, Lebrecht A, Cadenas C, Marchan R, Stewart J, Solbach C, Holmberg L, Edlund K, Kultima HG, Rody A, Berglund A, Lambe M, Isaksson A, Botling J, Karn T, Müller V, Gerhold-Ay A, Cotarelo C, Sebastian M, Kronenwett R, Bojar H, Lehr HA, Sahin U, Koelbl H, Gehrmann M, Micke P, Rahnenführer J and Hengstler JG: A Comprehensive Analysis of Human Gene Expression Profiles Identifies Stromal Immunoglobulin κ C as a Compatible Prognostic Marker in Human Solid Tumors.. Clinical Cancer Research. 2012 May 1;18(9):2695-2703.

2. Cadenas C, Vosbeck S, Hein EM, Hellwig B, Langer A, Hayen H, Franckenstein D, Büttner B, **Hammad S,** Marchan R, Hermes M, Selinski S, Rahnenführer J, Peksel B, Török Z, Vígh L and Hengstler JG: Glycerophospholipid profile in oncogene-induced senescence. Biochimica et Biophysica Acta BBA-Molecular and Cell Biology of Lipids. 2011 Dec 10. [Epub ahead of print].

3. Schreiber S, Rignall B, Braeuning A, Marx-Stoelting P, Ott T, Buchmann A, **Hammad S,** Hengstler JG, Schwarz M and Köhle C: Phenotype of single hepatocytes expressing an activated version of β-catenin in liver of transgenic mice. Journal of Molecular Histology, 2011 Oct., Volume 42, Issue 5, Pages: 393-400.

4. Zellmer S, Schmidt-Heck W, Godoy P, Weng H, Meyer C, Lehmann T, Sparna T, Schormann W, **Hammad S,** Kreutz C, Timmer J, von Weizsäcker F, Thürmann PA, Merfort I, Guthke R, Dooley S, Hengstler JG, Gebhardt R: Transcription factors ETF, E2F, and SP-1 are involved in cytokine-independent proliferation of murine hepatocytes. Hepatology, 2010 Dec., Volume 52, Issue 6, Pages: 2127-2136.

List of publications

==========

5. Braeuning A, Singh Y, Rignall B, Buchmann A, **Hammad S,** Othman A, von Recklinghausen I, Godoy P, Hoehme S, Drasdo D, Hengstler JG, Schwarz M: Phenotype and growth behavior of residual β-catenin-positive hepatocytes in livers of β-catenin-deficient mice. Histochemistry and Cell Biology, 2010 Nov., Volume 134, Number 5, Pages 469-481.

6. Godoy P, Lakkapamu S, Schug M, Bauer A, Stewart JD, Bedawi E, **Hammad S,** Amin J, Marchan R, Schormann W, Maccoux L, von Recklinghausen I, Reif R and Hengstler JG: Dexamethasone-dependent versus -independent markers of epithelial to mesenchymal transition in primary hepatocytes. Biological Chemistry, 2010 Jan, Volume 391, Issue 1, Pages: 73-83.

Manuscripts in preparation

7. Hoehme S, Schwen LO, D'Alessandro LA, Friebel A, Neitsch J, Raue A, Rho SH, Gremse F, von Recklinghausen I, **Hammad S**, Ghallab A, Godoy P, Reif R, Kiessling F, Timmer J, Preusser T, Hengstler J, Klingmueller U and Drasdo D (2012)
   Multiscale modeling of liver regeneration.

8. Hoehme S, **Hammad S**, Othman A, vonRecklinghausen I, Böttger J, Dirsch, Gebhardt R, Hengstler JG, Drasdo D (2012): Biomechanical vs. biochemical control of liver regeneration in mice and pigs.